

AD620525

AFOSR Scientific Report

AFOSR No. 68-0771

Final Report

# RESPONSE OF A BURNING PROPELLANT SURFACE TO EROSION TRANSIENTS

Prepared For

AIR FORCE OFFICE OF SCIENTIFIC RESEARCH  
WASHINGTON, D C

CONTRACT AF 49 638-1665

STANFORD RESEARCH INSTITUTE

MENLO PARK, CALIFORNIA



Reproduced by the  
**CLEARINGHOUSE**  
for Federal Scientific and Technical  
Information Springfield, MA 01101

STANFORD RESEARCH INSTITUTE

MENLO PARK CALIFORNIA



April 30, 1968

*AFOSR Scientific Report*

*AFOSR No. 68-0771*

*Final Report*

## RESPONSE OF A BURNING PROPELLANT SURFACE TO EROSION TRANSIENTS

*Prepared For:*

AIR FORCE OFFICE OF SCIENTIFIC RESEARCH  
WASHINGTON, D C

CONTRACT AF 49(638)-1665

*By* G A MARXMAN, C E WOOLDRIDGE, and E L CAPENER

*SRI Project PGU-5818*

*Approved:* MARJORIE W EVANS, DIRECTOR

FOR THE LABORATORY FOR HIGH SPEED RESEARCH

Copy No 98

## FOREWORD

The experimental and theoretical studies described in this report are the responsibilities of E. L. Capener and G. A. Marxman, respectively. Major contributors to this research include G. A. Marxman (Principal Investigator), E. L. Capener, C. E. Wooldridge, R. J. Kier. In early 1967, supervision of the program was transferred from L. A. Dickinson to G. A. Marxman.

## ACKNOWLEDGMENT

This research, under Contract AF 49(638)-1665, Project-Task No. 9711-01, and for the period 1 January 1966 through 31 December 1967, was sponsored by the Air Force Office of Scientific Research, Office of Aerospace Research, United States Air Force.

Technical Supervisor for this program was Dr. Bernard T. Wolfson, Project Scientist, Propulsion Division, Directorate of Engineering Sciences, Air Force Office of Scientific Research.

## Conditions of Reproduction

Reproduction, translation, publication, use, and disposal in whole or in part by or for the United States Government is permitted.

## SUMMARY

This report describes an investigation of high-amplitude axial-mode solid rocket combustion instability which arises in the form of an oscillating shock wave in the combustion chamber. Experimental studies have provided an evaluation of the influence of compositional factors, oxidizer type, and deflagration characteristics on the incidence of axial instability. The stability characteristics of a wide range of ammonium perchlorate and potassium perchlorate propellants were determined in motors ranging from 15 to 82 in. in length, using an explosive pulse to initiate a traveling shock wave. Differential thermal analysis of these propellants, and experiments incorporating fiber-optic devices with high-speed photography, indicated that surface-coupled heat release is a key factor underlying the different stability behavior observed with various propellants. This concept formed the basis for theoretical studies during the program.

A theoretical combustion model was proposed and a mathematical analysis was developed that predicts the response of a burning propellant to the pressure pulse imposed by a traveling shock wave as it passes over the propellant surface. Also considered theoretically was the interaction mechanism through which this burning rate response supports the shock wave. The resulting theory predicts the limits of the stable operating regime for individual propellants in terms of thermochemical parameters and the degree of surface-coupled heat release associated with the propellant type. The theory provides a consistent explanation of all stability characteristics observed experimentally during this program and established guidelines for avoiding axial instability.

# CONTENTS

FOREWORD	111
ACKNOWLEDGMENT	111
SUMMARY	v
LIST OF ILLUSTRATIONS	1x
LIST OF TABLES	xiii
NOMENCLATURE	xv
I INTRODUCTION	1
II THEORETICAL STUDIES	3
Formulation of the Combustion Model	5
Physical Interpretation of the Surface Reaction Kinetics	8
Linear Analysis of the Combustion Model	8
Consequences of Different Assumptions for the Treatment of Surface-Coupled Reaction Kinetics	18
Relationship of This Analysis to Other Recent Studies	20
Modified Combustion Model and Nonlinear Theory	23
Predicted Steady-State Behavior of the Flame Temperature	24
Theoretical Description of the Distribution of Heat Release in Solid Propellant Combustion	25
Modification of the Combustion Model	28
Mechanism of Interaction Between Propellant Response and Shock Wave	31
III EXPERIMENTAL STUDIES	41
Differential Thermal Analysis (DTA) of Propellants	41
Fiber-Optic Studies of the Solid Propellant Combustion Zone	61
Traveling Wave Phenomena	70

IV THEORETICAL INTERPRETATION OF EXPERIMENTAL RESULTS	83
The Frequency Criterion	83
The Response Amplitude Criterion	87
Theoretical Combustion Instability Limit	89
The Propellant Response to a Steep-Fronted Pressure Wave	93
V CONCLUSIONS AND RECOMMENDATIONS	97
APPENDIX A: LINEAR ANALYSIS OF THE COMBUSTION MODEL BASED ON A TRANSFORMATION	99
APPENDIX B: THE NUMERICAL ANALYSIS OF THE NONLINEAR THEORETICAL COMBUSTION MODEL	101
APPENDIX C: REINFORCEMENT OF A SHOCK WAVE BY A MASS SOURCE	107
APPENDIX D: DERIVATION OF THE CALCULATED STABILITY LIMIT	113
REFERENCES	117
DD FORM 1473	

## ILLUSTRATIONS

Fig. 1	Stability Limits for the Self-Excited Mode	11
Fig. 2	The Response Function in the Steady Oscillatory Mode	13
Fig. 3	Phase Relation Between Mass Flux and Pressure in the Steady Oscillatory Mode (a Positive Angle Corresponds to a Leading Mass Flux)	15
Fig. 4	Simplified Model of the Distribution of Heat Release in the Solid Propellant Combustion Process	26
Fig. 5	Wave Diagram of a Traveling Shock with No Combustion Support	32
Fig. 6	Wave Diagram of a Traveling Shock with Combustion Support Through Mass Addition	35
Fig. 7	Mass Addition Perturbation Required To Support a Traveling Shock	38
Fig. 8	High-Pressure DTA Cell	42
Fig. 9	Differential Thermal Analysis of AP	42
Fig. 10	Differential Thermal Analysis of AP Propellants	43
Fig. 11	DTA Thermograms for PBD Propellant with Technical-Grade AP	45
Fig. 12	DTA Thermograms for PBD Propellant with High-Purity AP	46
Fig. 13	DTA Thermograms for 80/20 AP/PPG Mixtures Showing Effect of AP Purity	47
Fig. 14	DTA Thermograms for Coated Technical-Grade AP	49
Fig. 15	DTA Thermograms for Coated Hi-Purity AP	50
Fig. 16	DTA Thermograms for Propellants Containing Coated Technical-Grade AP	51
Fig. 17	DTA Thermograms for Propellants Containing Coated High-Purity AP	52

Fig. 18	Burning Rate for Propellants Containing Coated and Noncoated Oxidizers	53
Fig. 19	Thermograms for Purified Propellants at Ambient and Elevated Pressures	55
Fig. 20	Thermogram for KP-Based Propellant	58
Fig. 21	Embedded Surface Thermocouple Response During Ignition of PU 128	59
Fig. 22	Embedded Surface Thermocouple Response During Ignition of PBAN 264	60
Fig. 23	Test Motor Used To Obtain Fiber-Optic Photographs	62
Fig. 24	Deflagration of Single AP Crystals (200 psig)	63
Fig. 25	Fiber-Optic Shadowgraph Showing the Deflagration of AP at the Surface of a Burning Solid Propellant	64
Fig. 26	Fiber-Optic View of the Ignition of Aluminum Particles at the Surface of a Burning Solid Propellant	66
Fig. 27	Fiber-Optic View of the Ignition of Aluminum Particles at the Surface of a Burning Solid Propellant	67
Fig. 28	Measurement of Aluminum Particle Diameter at Ignition	68
Fig. 29	Apparent Diameter of Aluminum Particles at Ignition	69
Fig. 30	Correlation of Threshold Pressure with Propellant Burning Rate in a 5 x 40-inch Rocket Motor	74
Fig. 31	Comparison of Stability Behavior of 5 x 40-Inch and 5 x 80-Inch Rocket Motors	75
Fig. 32	Influence of Burning Rate and Composition on Traveling Wave Instability in a 5 x 40-Inch Rocket Motor (Instability Denoted by Dashed Curves)	76
Fig. 33	Traveling Wave Instability in a Slab Burner	77
Fig. 34	Head-End Pressure Transients During Traveling Wave Instability in a Tubular Burner	79 & 80
Fig. 35	Burning Rate Behavior of the Five AP Propellants Selected for Detailed Analysis	90



Fig. 36	Stability Boundary Of AP Propellants Subjected to Finite-Wave, Axial-Mode Pressure Disturbances	92
Fig. 37	The Calculated Propellant Response to a Sharp-Fronted Pressure Wave	94
Fig. 38	Integrated Mass Addition Perturbation as a Function of Position	96
Fig. C-1	The Mass Addition Process Behind the Shock Wave	108
Fig. C-2	Behavior of the Mach Number Function $\phi$	111

## TABLES

I	COMPARISON OF TECHNICAL-GRADE AND HIGH-PURITY AP	43
II	PBD PROPELLANT FORMULATION	46
III	PROPELLANT COMPOSITIONS FOR COATED OXIDIZER STUDY	54
IV	MASS SPECTROGRAPHIC GAS ANALYSIS OF PRODUCTION GRADE	56
V	MASS SPECTROGRAPHIC GAS ANALYSIS OF 70/30 HIGH-PURITY AP/PBD PROPELLANT	58
VI	PROPELLANT COMPOSITIONS FOR THERMOCOUPLE STUDIES	59
VII	EXPERIMENTAL PROPELLANT FORMULATIONS	71
VIII	AXIAL INSTABILITY TEST DATA FOR AP-CONTAINING PROPELLANTS	73
IX	TUBULAR MOTOR INSTABILITY DATA	81
X	FREQUENCY OF PRESSURE PULSE (cps)	84
XI	APPROXIMATE RESONANT-FREQUENCY RANGE FOR A TYPICAL COMPOSITE PROPELLANT ACCORDING TO THEORETICAL COMBUSTION MODEL	85
D-1	PROPELLANT PARAMETERS REQUIRED FOR THEORETICAL ANALYSIS	114

## NOMENCLATURE

$a$	frequency factor in Arrhenius law
$A$	pyrolysis kinetics parameter
$A_t$	nozzle throat area
$C$	constant
$c_p$	specific heat capacity of gas at constant pressure
$c_s$	specific heat capacity of solid
$D_p$	port diameter
$E_D$	activation energy for pressure-insensitive surface-coupled reactions
$E_f$	activation energy for gas-phase reaction
$E_H$	activation energy for pressure-sensitive surface-coupled reactions
$E_w$	activation energy for pyrolysis at interface
$f$	frequency (cps)
$h$	enthalpy
$h_{g_w}$	energy carried into gas phase with vaporizing propellant per unit mass
$h_{s_w}$	energy carried by convection from unreacted solid phase per unit mass
$J$	port-to-throat area ratio
$k$	thermal conductivity of solid
$K_n$	ratio of propellant surface area to throat area
$L$	heat of vaporization per unit mass of propellant
$m$	order of heterogeneous reaction; mass flux from wall
$M$	Mach number
$n$	order of gas-phase reaction

$p$	chamber pressure
$q$	stability parameter
$Q_D$	heat of reaction per unit mass of reactant in pressure-insensitive surface-coupled reaction
$Q_D^*$	nondimensional heat of reaction per unit mass of reactant in pressure-insensitive surface-coupled reaction
$Q_H$	heat of reaction per unit mass of reactant in pressure-sensitive surface-coupled reaction
$Q_H^*$	nondimensional heat of reaction per unit mass of reactant in pressure-sensitive surface-coupled reaction
$Q_r$	heat of reaction per unit mass of reactant in gas-phase reaction
$Q_s$	heat of AP decomposition
$Q_T$	total heat of combustion
$R$	gas constant
$r$	burning rate
$T$	temperature
$t$	time
$u$	velocity
$x$	distance into propellant from surface
$y$	transformed distance

#### Greek letters

$\alpha$	kinetics parameter
$\alpha_o$	kinetics parameter
$\gamma$	specific heat ratio, $c_p/c_v$
$\kappa$	thermal diffusivity of solid ( $= k/\rho_s c_s$ )
$\epsilon_r$	mass fraction of reactant at propellant surface (nearly unity)
$\theta_s$	surface-coupled heat release parameter
$\nu$	pressure exponent in empirical burning rate law

- $\zeta_D$  fraction of steady-state total heat of combustion,  $Q_T$ , associated with pressure-insensitive surface-coupled reactions
- $\zeta_H$  fraction of steady-state total heat of combustion,  $Q_T$ , associated with pressure-sensitive surface-coupled reactions
- $\rho_s$  density of solid propellant
- $\varphi$  phase angle between mass flux and pressure; Mach number function
- $\chi$  number of sites that undergo surface-coupled reactions per unit mass of solid propellant
- $\omega$  frequency (rad/sec)

#### Subscripts

- c chamber
- f gas-phase flame
- g gas phase
- i initial value at  $t = 0$
- o conditions at  $x \rightarrow \infty$
- s solid phase
- w conditions at wall (gas-solid interface)

#### Superscripts

- \* nondimensional quantity normalized to steady-state value;  
e.g.,  $r^* = r/r_i$ ,  $T_f^* = T_f/T_{f_i}$ . Note one exception:  $T_o^* = T_o/T_{w_i}$ .  
Also,  $t^* = r_i^2 t/K$  and  $x^* = r_i x/K$ .
- denotes value of quantity prior to pressure disturbance
- $\sim$  denotes difference between perturbed and unperturbed value, divided by unperturbed value;  $\tilde{r} = (r(t) - \bar{r})/\bar{r}$ .

## I. INTRODUCTION

The reliable performance of present and future solid propellant rockets is seriously handicapped by combustion instability phenomena. The associated problems have been the subjects of intense research for many years, but most of this effort has been devoted to acoustic instability, or periodic small-amplitude disturbances in the acoustic modes of the chamber. In contrast, the present study has been concerned with finite-amplitude, traveling-wave instability in the axial mode. Relatively little previous research on this topic has been performed.

To make this final report on the project a potentially useful document, the most important experimental and theoretical developments of the entire contract period are discussed and summarized herein. Included in the following sections are the propellant response theory, the analysis of the driving mechanism, the experimental measurements of propellant characteristics and stability behavior, and a comparison of theory and experimental observations. The report culminates in a description of a quantitative theoretical method for determining a stability map for solid propellants, and this method is shown to predict observed stability limits of some 20 different propellants.

The ultimate goal of the investigation was to develop theoretical guidelines for avoiding axial combustion instability, and it is felt that this objective has been fully achieved. The guidelines appear in the conclusion of the report. The success achieved in interpreting the experimental observations indicates that the application of these principles should substantially reduce the probability of encountering finite-amplitude, axial-mode combustion instability in future solid propellant rocket motors.

## II. THEORETICAL STUDIES

The importance of the combustion response in all unstable combustion situations has been widely recognized, although this investigation, more than others, has emphasized the combustion interaction with traveling waves in the axial mode of the motor chamber. During this investigation a major part of the theoretical effort was focused on the formulation of a combustion model that would adequately describe the response of the combustion mechanism to pressure disturbances induced by traveling shock waves passing over the propellant surface. This theoretical approach was motivated by two general observations relevant to axial-mode instability in solid-propellant motors: (1) different propellants have widely differing stability characteristics in a given combustion chamber,<sup>1</sup> suggesting that the combustion response, rather than gas-dynamical interactions with the chamber and nozzle, is the controlling factor; and (2) those propellants with a relatively high amount of surface-coupled heat release, such as the ammonium perchlorate (AP)-based propellants with their significant solid-phase exotherms, are particularly susceptible to unstable combustion.<sup>2,3</sup>

Acoustic instability problems have stimulated a number of theoretical studies of the combustion response, which is characterized in terms of an "acoustic admittance," or more generally, in terms of the "response function." Most of these studies, which are comprehensively summarized elsewhere,<sup>4</sup> have been basically similar and have neglected surface-coupled reactions entirely. Notable exceptions are the recent analyses by Friedly and Petersen<sup>5</sup> and by Culick,<sup>6</sup> in which energetic surface reactions are considered. There have also been several treatments of the effect of surface reactions by Zel'dovich and his colleagues and students in the Soviet Union, recently summarized by Vantoch.<sup>7</sup> All of these theoretical analyses lead to the conclusion that surface reactions tend to have a stabilizing influence on the propellant. As was noted above, this conclusion appears to be in direct conflict with our experimental observations on composite propellants. Thus, it seems

quite clear that the combustion models underlying these analyses, which differ mainly in mathematical details, do not adequately represent the true combustion mechanism of this class of propellants. Interestingly enough, the analyses appear to describe double-base propellants much better than composites, for the former are observed to have instability regimes that are essentially the opposite of those associated with composites.<sup>1</sup>

In an effort to explain this situation, a new combustion model was formulated during this investigation.<sup>1, 2, 8, 9</sup> This model differs from earlier ones primarily in the kinetics description of the surface reactions. Through the surface kinetics treatment the SRI model distinguishes between composite and double-base propellants, unlike other theories. Detailed calculations and comparisons with instability data show that this model is consistent with observations of both classes of propellants. Specifically, surface-coupled exotherms are shown to have a destabilizing effect on composite propellants, whereas pressure-sensitive surface exotherms tend to stabilize double-base propellants.

The theoretical analysis developed during this study was the first to yield conclusions that are consistent with the experimental data. Subsequently two other treatments of surface reaction effects have been proposed that provide somewhat similar but not identical conclusions.<sup>10, 11</sup> The assumptions underlying these analyses differ substantially from those of the present investigation. A comparison of these theories appears later in this section of the report.

To complete the treatment of transient combustion response, a modified version of the model, used in a nonlinear analysis, is presented in this section. The remainder of the theoretical discussion deals with the interaction mechanism through which the burning rate response to pressure disturbances, as described by the combustion model, acts to support the traveling shock wave, thereby causing axial-mode combustion instability.



### Formulation of the Combustion Model

The chief assumptions made in formulating the model were the following:

(a) the gas-phase reactions can be represented in terms of a single reaction of arbitrary order that obeys Arrhenius kinetics and responds instantaneously to pressure and temperature disturbances (i.e., time-dependent terms are omitted in the gas-phase equations); (b) the Lewis number is unity in the gas phase; (c) surface pyrolysis and surface-coupled exothermic or endothermic reactions follow Arrhenius laws; and (d) the solid phase is essentially homogeneous with temperature-independent transport properties. For typical propellants, assumption (a) is valid for chamber oscillations at frequencies of a few thousand cycles per second or less. Most of the acoustic instability problems of greatest interest fall within this regime.

As assumption (b) implies, the pyrolysis and surface-coupled reactions are assumed to occur in a surface layer of negligible thickness relative to the penetration depth of the temperature profile. It is difficult to evaluate the quantitative effect of assumptions (b), (c), and (d). However, it is important to remember that all analyses of this kind unavoidably rely on a highly simplified picture of the complex combustion process. Within this context these assumptions seem fully justified, even necessary, because they permit a simplified mathematical formulation that is consistent with the underlying concepts.

The formulation begins with the equation governing heat conduction in the solid phase beyond the surface reaction zone. In nondimensional form:

$$\frac{\partial T^*}{\partial t^*} = r^* \frac{\partial T^*}{\partial x^*} + \frac{\partial^2 T^*}{\partial x^{*2}} \quad (1)$$

The propellant pyrolysis at the wall is assumed to follow an Arrhenius law, so that the burning rate is related to wall temperature as follows:

$$r^* = \exp \left[ (E_w / RT_{w_i}^*) (T_w^* - 1) / T_w^* \right] \quad (2)$$

The following boundary condition is imposed upon temperature:

$$x^* \rightarrow \infty; T^* \rightarrow T_o^* \quad (3)$$

The remaining boundary condition is obtained through an energy-flux balance at the solid-gas interface. The net heat conducted into the unreacted solid propellant from the interface at the plane  $x = 0$  is:

$$-\left(\frac{\partial T^*}{\partial x^*}\right)_w = -\left(\frac{\partial T^*}{\partial x^*}\right)_{g_w} - r^* (h_{g_w} + h_{s_w} - Q_H - Q_D) / c_s \bar{T}_w \quad (4)$$

The first term on the right-hand side of the equality sign represents the energy coming from the gas phase; the second, the energy carried into the gas with the vaporizing propellant; the third, the energy carried by convection from the unreacted solid phase into the interface; the fourth, the energy released (positive) in heterogeneous decomposition reactions at the surface whose reaction rates depend upon the local gas-phase density; and the last, the energy released in solid-phase surface reactions with rates that are independent of gas-phase conditions. It is convenient to rewrite this expression as follows:<sup>12</sup>

$$\left(\frac{\partial T^*}{\partial x^*}\right)_w = -\left(\frac{\partial T^*}{\partial x^*}\right)_{g_w} + r^* \left[ (c_s - c_p)(T_w - T_o) - L + Q_H + Q_D \right] / c_s \bar{T}_w \quad (5)$$

Denison and Baum<sup>12</sup> have obtained a solution to the gas-phase conservation equations by assuming that the complex gaseous reaction process can be represented by a single-step reaction of order  $n$ , where in some cases  $n$  may not be an integer. We retain their gas-phase solution, which yields the following expression for the heat flux from the gas phase to the wall:

$$-\left(\frac{\partial T^*}{\partial x^*}\right)_{g_w} = r^* \left[ \epsilon_r Q_r - c_p (T_f - T_w) \right] / c_s \bar{T}_w \quad (6)$$

This solution also relates the instantaneous flow of reactant into the gaseous reaction zone  $\rho_s r$  to the instantaneous gas-phase reaction rate, so that:

$$r^* = p^{*n/2} T_f^{*1+n/2} \exp \left[ (E_f / 2RT_f) (T_f^* - 1) / T_f^* \right] \quad (7)$$

It is assumed that the surface-coupled reactions occur in a thin zone so that the surface heat release acts as a boundary condition on the solid phase. The heterogeneous heat release per unit mass flux through the reaction zone can be expressed in terms of an Arrhenius law as

$$Q_H^* = (p^* / T_w^*)^m \exp \left[ (E_H / RT_w) (T_w^* - 1) / T_w^* \right] \quad (8)$$

for a pressure-sensitive reaction.

In reality  $Q_H$  probably depends on the thickness of the surface reaction zone (which is related to  $\rho_s r$ ) and on the specific nature of the pyrolysis process (which is also related to  $\rho_s r$  ultimately). Thus, one might choose to write the above kinetics expression including  $(\rho_s r)^y$  as a factor, for example. Then the exponent  $y$  would become an unknown, and somewhat indirect, measure of the extent of surface reactions relative to gas-phase reactions. However, such a modification would not significantly alter the conclusions, and it has essentially no effect on the perturbation analysis given below. Therefore until there emerges a more detailed understanding of the mechanism, any further complication of this type probably is unwarranted and will not be considered here.

Except that they are independent of the pressure, the other surface reactions follow a similar law:

$$Q_D^* = \exp \left[ (E_D / RT_w) (T_w^* - 1) / T_w^* \right] \quad (9)$$

Equations (5), (6), (8), and (9) can be combined to obtain:

$$-\left(\frac{\partial T^*}{\partial x}\right)_w = r^* \left\{ (\epsilon_r Q_r - L)/c_s \bar{T}_w - (c_p/c_s) \left[ (\bar{T}_f/\bar{T}_w) T_f^* - T_o^* \right] + (T_w^* - T_o^*) + (1 - T_o^*)(\zeta_H Q_H^* + \zeta_D Q_D^*) \right\} \quad (10)$$

Equations (1), (2), and (7), with the boundary conditions of Eqs. (3) and (10), complete the mathematical representation of the combustion model in terms of the dependent variables  $T_f^*$ ,  $T_w^*$ , and  $r^*$ .

#### Physical Interpretation of the Surface Reaction Kinetics

For composite propellants we may envision the surface reaction zone as encompassing, first, pyrolysis of the propellant (described by Eq. 2) and subsequently, surface-coupled reactions among the pyrolysis products (described by Eqs (8) and (9)). Thus, the activation energies  $E_H$  and  $E_D$  associated with Eqs. (8) and (9) represent an overall description of a complicated sequence of events, which may include mixing between the various macroscopic constituents of the composite propellant, as well as reaction steps. In contrast, with a double-base propellant there is no reason to distinguish surface-coupled energetic reactions from pyrolysis reactions, because the constituents are intermixed on a molecular scale. Thus, the pyrolysis and other reactions may be considered as a single sequence, with a single activation energy  $E_w$  characterizing the rate-controlling step, and with  $E_H = E_D = 0$ . A possible exception might occur with heterogeneous reactions, which could call for a very small value of  $E_H$  associated with molecular mixing between gas-phase constituents and pyrolysis products.

#### Linear Analysis of the Combustion Model

Owing to the nonlinear character of the equations describing the combustion model, a general closed-form solution cannot be obtained. However, an analytical solution appropriate to small pressure disturbances can be derived in a straightforward manner by using the customary

small-perturbation approach. The resulting linear analysis affords a physically clear interpretation of the main implications of the combustion model. Of course, nonlinear effects may be important in dealing with pressure disturbances associated with traveling shock waves, unless these waves are weak. (As will become apparent in later discussion, the shock waves encountered in axial instability do in fact tend to be quite weak, having a Mach number near unity.) Nonlinear effects may be accounted for by programming the appropriate equations for a digital computer, but the numerical approach does not readily provide physical insight. Therefore, to display the important features of the model it is convenient here to consider a linear treatment first, deferring the discussion of the nonlinear numerical solution to a later section of the report.

The linear analysis is accomplished by performing a mathematical transformation of an earlier treatment by Denison and Baum,<sup>12</sup> whose model excluded the possibility of surface-coupled reactions. The transformation makes their mathematical analysis applicable to the model presented above, which specifically includes surface-coupled exothermic or endothermic reactions. Thus, from a mathematical viewpoint the present linear analysis is formally identical to that of Denison and Baum, but describes the behavior of a more realistic combustion model. The transformation appears in Appendix A, and the results of the analysis will be summarized in the following discussion.

According to the linear theory, a given propellant can be characterized in terms of three parameters:<sup>12</sup>  $A$ , which relates to the surface decomposition kinetics;  $\alpha_0$ , which relates to the gas-phase kinetics; and  $\nu$ , the steady-state pressure exponent. The stable zone is described by the relation

$$q^2 - q - 2A < 0 \quad (11)$$

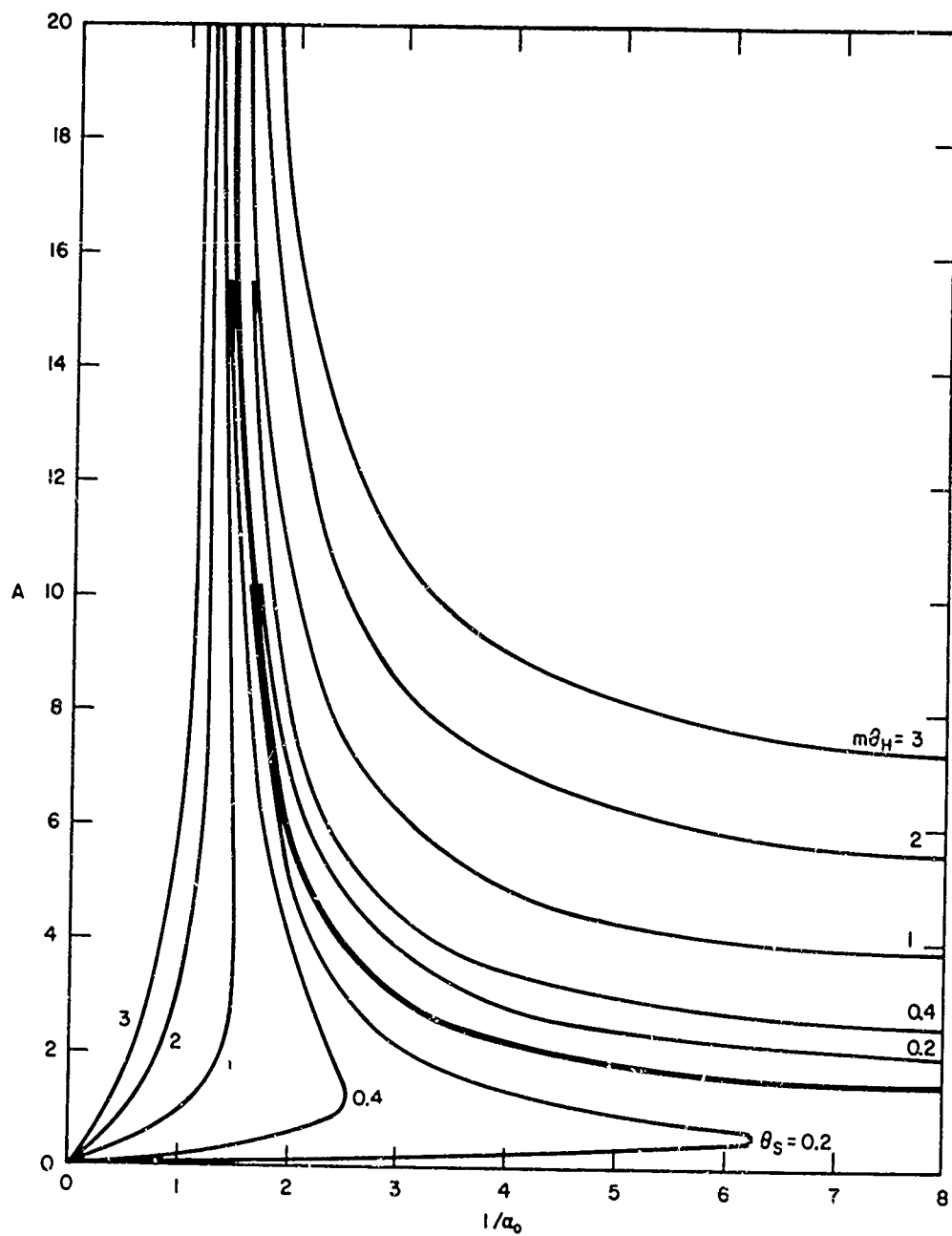
where

$$q = 1 + \theta_s + A(1 - \alpha_0) - 1 + A(1 - \alpha)$$

Since no propellant that is incipiently unstable can exist in nature, Eq. 11 describes the limiting behavior of all real propellants. However, even though no propellant can be unstable in the mathematical sense, very large numerical values can be obtained for the response function in the immediate vicinity of the limit line. The maximum in the response function will occur at a preferred frequency which is near the unbounded oscillatory frequency associated with the limit line, and the large response at this frequency is interpreted experimentally as "combustion instability." Thus, the location of the limit line is important because it defines the region in which the steady oscillatory response will have a large amplitude.

Figure 1 shows a series of limit lines in the  $A$  versus  $1/\alpha_0$  coordinate system corresponding to different values of surface-coupled heat release. In each case the stable region lies to the left of the line, and a large steady oscillatory response is obtained for values of  $A$  and  $\alpha_0$  which lie close to, but to the left of, any given limit line. The original Denison-Baum limit line,<sup>12</sup> which was derived for zero surface heat release, is shown as the heavy unlabeled line. When surface heat release is present, the additional parameter  $\theta_s$ , which is related to the proportion of surface-coupled heat release, enters the solution. The mathematical transformation discussed previously allows the immediate prediction of the shift in the limit line induced by surface reactions. It is important to understand, however, that the transformation collapses all of the limit lines into the "universal" Denison-Baum line in the  $A$ - $1/\alpha$  coordinate system; i.e., the heavy line of Fig. 1 becomes a universal curve when the abscissa is identified as  $1/\alpha$  rather than  $1/\alpha_0$ .

The curves that lie below the Denison-Baum line in Fig. 1 correspond to the composite propellant heat release description of the preceding subsection. It can be seen that a relatively small proportion of surface-coupled heat release can profoundly decrease the extent of the stable region: the effect becomes more pronounced as  $A$  decreases. The curves that lie above the Denison-Baum line correspond to the double-base propellant model for which  $\theta_s = -m\zeta_H(1 - T_o^*)$ . In this case the effect of



TA-6577-38

FIG. 1 STABILITY LIMITS FOR THE SELF-EXCITED MODE

surface-coupled heat release is found to be stabilizing, in agreement with the work of Soviet investigators.<sup>13 14</sup>

According to the transformation of Eq. (A2), Appendix A, the response of the surface mass addition rate to a sinusoidal forcing pressure fluctuation can be expressed as<sup>12</sup>

$$\frac{1}{v} \frac{\tilde{m}}{\tilde{p}} = \frac{A_\alpha}{\sqrt{a^2 + b^2}} \frac{\omega \kappa}{r^2} \sin(\omega t + \varphi) \quad (12)$$

where the phase angle  $\varphi$  is given by

$$\varphi = \tan^{-1} (b/a) + \pi/2 \quad (13)$$

and where

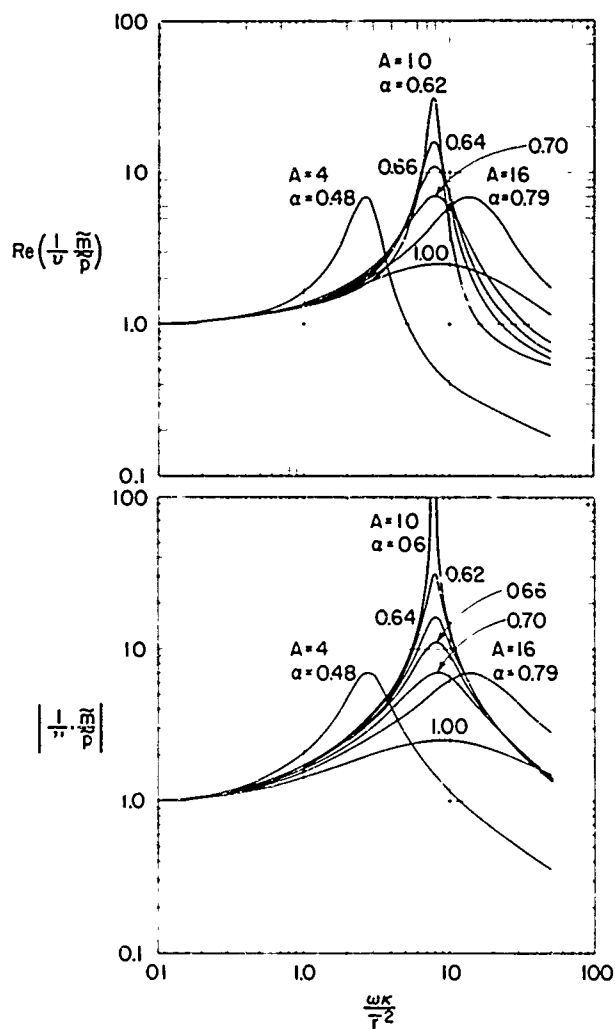
$$a = A (1 + \lambda_r) - \frac{\omega \kappa}{r^2} \lambda_i; \quad b = \frac{\omega \kappa}{r^2} (\lambda_r + q) + A \lambda_i$$

$$\lambda_i = -\frac{1}{2} \left[ \frac{-1 + (1 + 16\omega^2 \kappa^2 / r^4)^{1/2}}{2} \right]^{1/2}$$

$$\lambda_r = -\frac{1}{2} \left\{ 1 + \left[ \frac{1 + (1 + 16\omega^2 \kappa^2 / r^4)^{1/2}}{2} \right]^{1/2} \right\}$$

Frequency response curves for selected values of  $A$  and  $\alpha$  are shown in Fig. 2. These curves correspond to the universal representation of the limit line which is obtained from the transformation. The lower section of Fig. 2 shows the absolute value of the ratio of the mass flow perturbation from the surface to the pressure perturbation, normalized by the steady-state pressure exponent  $v$ . Such a normalization is required to obtain a universal representation of the response function. The upper section of Fig. 2 shows the real part of the mass flux/pressure perturbation ratio, i.e., the component of the response function which is in phase with the pressure perturbation. It is this quantity that governs the outcome of the stability analysis.





TB-5577-36

FIG. 2 THE RESPONSE FUNCTION IN THE STEADY OSCILLATORY MODE

A family of curves is shown for  $A = 10$ . A decreasing value of  $\alpha$  corresponds to horizontal movement to the left away from the universal limit line of Fig. 1. Near the limit line very small changes in  $\alpha$  cause large changes in the amplitude of the response function. This demonstrates the importance of the location of the limit line for any given propellant. At values of  $\alpha$  near the limit line the real part of the response shown in Fig. 2 has a narrower peak than the absolute

response, but the peak amplitudes are nearly the same, reflecting the nearly zero phase shift which occurs near the peak. (The real part of the response is not shown for the limiting value of  $\alpha$ , since only in this case does the phase angle exceed  $90^\circ$ , giving rise to a spurious negative real part. In practice, operation on the limit line itself can never be attained.) As the amplitude of the response decreases with increasing  $\alpha$ , the response curves broaden and the real part becomes more nearly like the absolute response. Also, the value of the frequency at which resonance occurs shifts only slightly with  $\alpha$  at a fixed value of  $A$ .

Also shown in Fig. 2 are response curves for  $A = 4$  and  $16$  whose amplitudes are equal to that of the  $A = 10$ ,  $\alpha = 0.70$  case. As the value of  $A$  increases, the response broadens markedly (note the logarithmic scale). This implies that propellants having a high activation energy of decomposition will be susceptible to random forcing functions over a much wider frequency band than those having lower activation energies. Since the limit lines on Fig. 1 become more nearly vertical as  $A$  increases, the value of  $\alpha$  corresponding to a constant amplitude response changes more and more slowly with increasing  $A$ . Finally, in connection with Fig. 2 it is important to note that the solution approaches the correct limits at large and small values of the frequency; i.e., as  $\omega \rightarrow \infty$ ,  $|\tilde{r}/\tilde{v}_p| \rightarrow 0$  and as  $\omega \rightarrow 0$ ,  $|\tilde{r}/\tilde{v}_p| \rightarrow 1$ .

Figure 3 shows the phase angle behavior for the  $A = 10$  family of frequency response curves. For all values of  $\alpha$  the rate of change of phase angle at  $\omega = 0$  is the same and the return to zero phase angle occurs at the same value of  $\omega K/\bar{r}^2$ . The peak in the response (see Fig. 2) shifts across this value of nondimensional frequency in the direction of increasing  $\omega$  as  $\alpha$  increases, and always occurs near it. The total swing in the phase angle decreases as  $\alpha$  increases, as implied previously in connection with the fact that the real response approaches the absolute response as  $\alpha$  becomes larger.

It should be noted that the present analysis groups all of the governing variables of the problem into two nondimensional parameters,

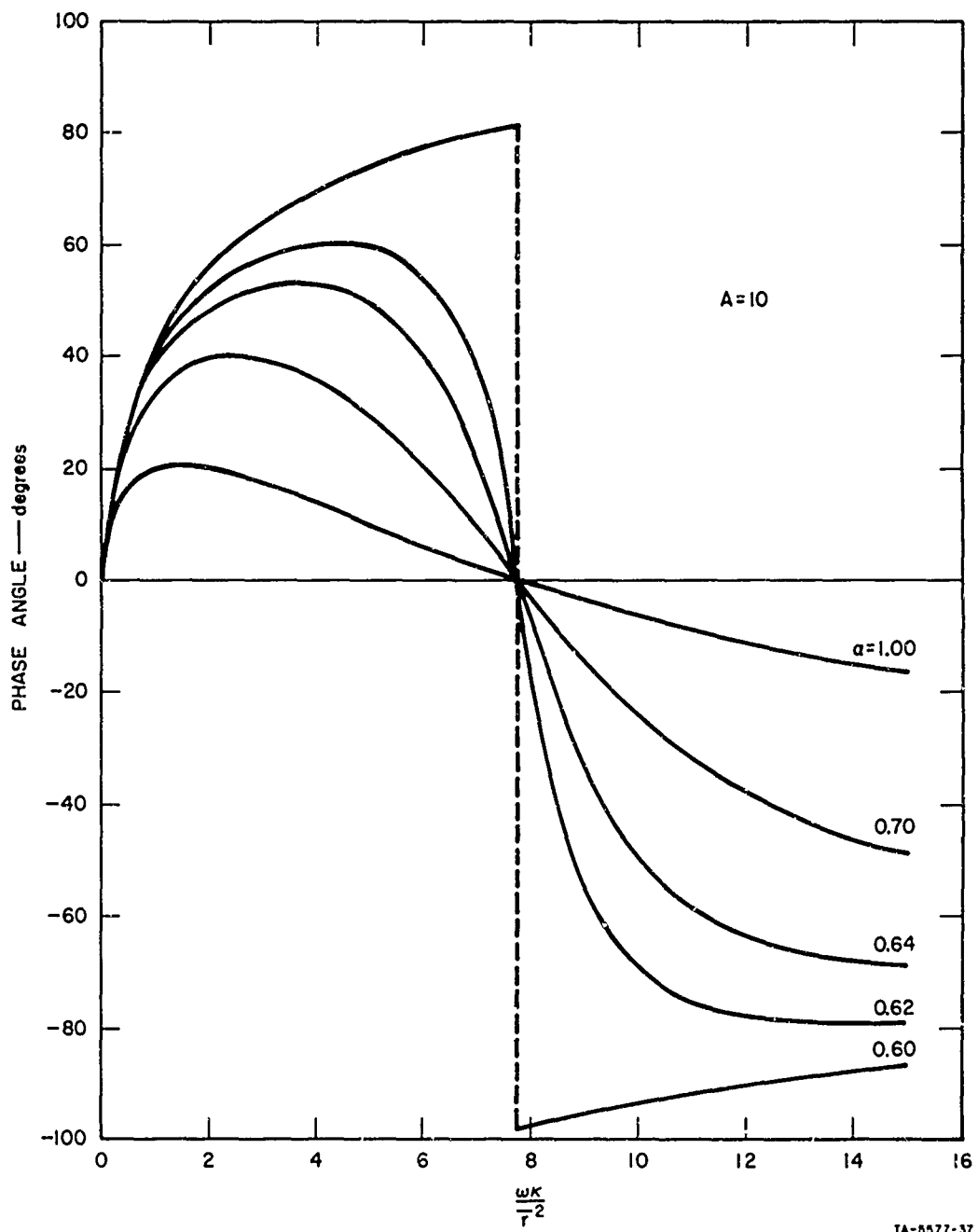


FIG. 3 PHASE RELATION BETWEEN MASS FLUX AND PRESSURE IN THE STEADY OSCILLATORY MODE (Positive Angle Corresponds to a Leading Mass Flux)

A and  $\alpha$ . This means that one family of response curves (such as those shown in Fig. 2) replaces the six families presented by Friedly and Petersen<sup>5</sup> who examined each variable individually.

In order to clarify the importance of surface-coupled heat release, we will consider here the response of both a typical composite and a typical double-base propellant. First, consider a composite propellant, which as noted above is characterized by nonzero values of  $E_H$  and  $E_D$ . Assume:

$$E_H/\bar{R}\bar{T}_w = E_D/\bar{R}\bar{T}_w = E_w/\bar{R}\bar{T}_w = 15$$

$$E_f/\bar{R}\bar{T}_f = 5$$

$$m = 1, n = 1.5, c_p/c_s = 1$$

$$\bar{T}_f = 2250^\circ\text{K}, \bar{T}_w = 1000^\circ\text{K}, T_o = 300^\circ\text{K}$$

$$Q_H/Q_T = Q_D/Q_T = 0.05$$

Then from Eqs. (A2) and (A3), Appendix A

$$\zeta_H = \zeta_D = 0.05, \theta_s = 1$$

$$\alpha_o = 0.75, \alpha = 0.65, A = 10.5$$

With these values for  $\alpha_o$  and  $\alpha$ , Fig. 2 shows that the peak response is doubled when there is 10% of the total heat release at the surface (i.e.,  $\zeta_H + \zeta_D = 0.10$ ). This demonstrates the strong influence that can be exerted by a relatively small surface heat release and helps to explain the sharp experimental demarcation between stable and unstable operation which has been obtained previously in our laboratory by Capener, et al.<sup>1-3</sup>

Using the numerical values given above, the effective pressure exponent changes from  $\nu_0 = n/2 = 0.75$  to  $\nu = 0.94$  (see Eq. (A3)) with addition of the surface-coupled heat release. This means that for the hypothetical propellant described here, 10% of the total heat release is near the upper limit that can be associated with the surface reactions if a stationary steady-state is to be attained. This is an important consideration in the formulation of new propellants.

Consider now a typical double-base propellant for which

$$E_H = E_D = 0, E_w/RT_w = 15$$

$$E_f/RT_f = 5$$

$$m = 0.3, n = 1.5, c_p/c_s = 1$$

$$\bar{T}_f = 2500^\circ \text{K}, \bar{T}_w = 1000^\circ \text{K}, T_o = 300^\circ \text{K}$$

$$\zeta_D = 0, \zeta_H = 0.7$$

Here it has been assumed that the heat release process in the surface zone is governed entirely by pressure-sensitive reactions having an order of 0.3. If there is no pressure sensitivity,  $\theta_s$  will be zero and there will be no effect of surface heat release. This was the case in the investigation of Friedly and Petersen,<sup>5</sup> who did not allow any pressure sensitivity in the surface process and whose results therefore show no effects of surface heat release. The typical double-base propellant has a much larger proportion of surface heat release than the typical composite propellant; for example, Soviet researchers have reported that as much as 80 percent of the total heat release may be generated in the surface zone.<sup>15</sup> Notice, however, that Eq. (A3), Appendix A, predicts a much smaller effect of heat release on the value of  $\theta_s$  in the double-base case, as compared to the composite case, because the large multiplying factor  $E_H/RT_w$  is gone and  $m$  is usually less than unity.

The numerical choices above give

$$\theta_s = 0.145, A = 10.5$$

$$\alpha_o = 0.83, \alpha = 0.85$$

In this case the effect of increasing the heat release is to increase  $\alpha$ , leading to a smaller peak response to forced pressure oscillations. The relative gain in stability, however, is smaller than the loss in stability caused by surface-coupled heat release in the composite case.

It is important to remember that the above analysis is limited to an upper frequency of a few thousand cycles per second because the relaxation processes in the gas phase have been completely neglected. For the  $A = 10$  case where resonance occurred near  $\omega K/\bar{r}^2 = 8$ , the corresponding frequency would be 51 cps if  $\bar{r} = 0.1$  in./sec and 1270 cps if  $\bar{r} = 0.5$  in./sec, using  $K = 2.5 \times 10^{-4}$  in.<sup>2</sup>/sec. These values are within the regime of validity for the analysis, but with substantially higher values of  $A$ ; for example, the results might be restricted to burning rates somewhat lower than 0.5 in./sec.

#### Consequences of Different Assumptions for the Treatment of Surface-Coupled Reaction Kinetics.

It is intuitively clear that surface-coupled reactions may be especially important in transient combustion phenomena, because an exotherm or endotherm coupled to the solid-phase temperature profile must either amplify or attenuate the resonance mechanism associated with different relaxation times of the gas and solid phases. The main conclusion of the present analysis is that surface-coupled reactions are not only important in oscillatory combustion, but that their effect also may depend critically on the detailed structure of the surface-zone kinetics. The potential significance of this conclusion becomes clear by relating it to the two general classes of solid propellants in terms of the combustion model.

According to the discussion following Eq. (10), a composite propellant generally corresponds to  $E_H > 0$  and/or  $E_D > 0$ , whereas for a typical double-base propellant  $E_H = E_D = 0$ . When there are exothermic surface-coupled reactions ( $\theta_H > 0$ ,  $\theta_D > 0$ ) for example, Eq. (A3) indicates that  $\theta_s > 0$  for composite propellants, whereas  $\theta_s < 0$  (unless  $E_H/RT_w > m$  owing to molecular mixing) for double-base propellants. It follows that exothermic surface-coupled reactions tend to destabilize composite propellants (by increasing the response amplitude), while they tend to stabilize double-base propellants. This rather remarkable theoretical conclusion may explain the previous experimental observation that the stable burning regimes of composite and double-base propellants are reversed.<sup>1-3</sup> It is important to recognize that the possibility of a destabilizing effect associated with surface-coupled exotherms does not arise unless there is a departure from the single-step description or the surface kinetics (i.e.,  $E_H = E_D = 0$ ). Because earlier treatments<sup>5,6</sup> have employed only the single-step description, they have not predicted this effect.

The method of describing surface kinetics in a combustion model is related to the assumed steady-state behavior of the overall heat of combustion, or the flame temperature. It is illuminating to consider the surface kinetics question within this context. In steady-state combustion,  $-k(\partial T/\partial x)_w = \rho_s r c_s (T_w - T_o)$ , in which case Eq. (10) becomes a simple expression for the gas-phase flame temperature in terms of the total heat release in the combustion process. In the present formulation, employing a two-step surface kinetics treatment, the total heat release per unit mass of propellant and the flame temperature tend to rise with increasing pressure because both surface terms increase. (A pressure increase raises  $r$  and therefore  $T_w$ .) For a realistic choice of parameters the increase in  $T_f$  is small, as it is with real propellants; in fact it can be made equal to that predicted by a thermochemical calculation for any given propellant, if desirable. This approach, which we have associated with composite propellants, leads to the general conclusion discussed above, i.e., that surface exotherms tend to make the propellant response less stable.

An alternative approach is to retain the two-step kinetics description but require that the total heat of combustion and  $T_f$  remain constant. This can be accomplished by imposing the restriction  $\theta_s \approx - (2m/n)(E/RT_w)\zeta_H(1-T_o^*)$ , from which it follows that the overall pressure exponent  $\nu = n/2$ . With this restriction the analysis leads a completely different conclusion; surface exotherms tend to stabilize the propellant. This is the result obtained by others.<sup>5,6</sup> However, the indicated restriction seems unrealistic. It implies that every exothermic surface reaction will be compensated for exactly by an endothermic reaction, such that the total surface heat release, as well as the overall total (including the gas-phase) heat release will remain constant.

Next we consider the single-step kinetics treatment, in which  $E_H = E_D = 0$ , so that all surface reactions are characterized by the pyrolysis activation energy. This form of kinetics description is used in all earlier analyses, and it always leads to the conclusion that surface-coupled exotherms stabilize the propellant. In the present treatment, where this case is identified with double-base propellants, it is found that the steady-state flame temperature again tends to rise with pressure (unless  $m = 0$ ), as with real propellants. However, if one requires that the flame temperature remain constant ( $\nu = n/2$ ), the present treatment shows that surface reactions have no first-order effect on propellant stability.

It is evident from the foregoing discussion that the method of incorporating surface reactions in the combustion model is a crucial factor. The experimental results obtained in our laboratory, which are summarized later in this report, associate surface exotherms with instability in composite propellants. Earlier analyses based on simpler kinetic descriptions predict the opposite behavior, whereas the present treatment is consistent with the observations.

#### Relationship of This Analysis to Other Recent Studies

After the model discussed above had been formulated, two other approaches to the analysis of combustion response with surface reactions



were proposed by other workers.<sup>10,11</sup> These analyses are more closely related to the present treatment than were earlier ones, because they also represent endeavors to characterize transient combustion behavior in terms of two or three parameters (e.g.,  $A$ ,  $\alpha$ ,  $\theta_s$  in the present case). Consequently, a brief comparison of these studies with the present work is in order.

The model advanced by Brown, Muzzy, and Steinle<sup>10</sup> describes the heat transfer from the gas phase as being proportional to  $(p^*)^{n'}$ . This assumption is essentially equivalent to replacing Eq. (7) of the present analysis with the empirical expression,  $r^* = (p^*)^{n'}$ , which is the usual empirical steady-state burning rate law. The difficulty with this approach is that the empirical description of steady-state behavior does not correctly relate the burning rate and pressure during transient behavior. It is easy to see that if the combustion mechanism includes pressure-sensitive surface-coupled reactions, as is usually assumed, then the overall pressure index of the propellant reflects the effect of surface reactions as well as the gas-phase reactions. However, it is fundamental to all analyses that the response time of surface reactions is substantially greater than that of gas-phase reactions; this means that the steady-state pressure index cannot apply to transient behavior, owing to a time-dependent shift in the relative contributions of surface and gas-phase reactions. In other words, during transient behavior the overall pressure index of the propellant is a function of time.

Equation (7) illustrates the importance of this effect. During steady-state burning the flame temperature changes little with pressure, so that  $v$  is the steady-state pressure index. However, during transient behavior the flame temperature changes markedly and is responsible for most of the change in burning rate registered by Eq. (7). Thus, if one were to replace Eq. (7) by a simple empirical power law,  $r^* = (p^*)^{n'}$ , the effective pressure index  $n'$  would have to be a function of time to correctly account for the behavior. One of the chief advantages of the Denison-Baum<sup>12</sup> gas-phase treatment leading to Eq. (7) is that it avoids all use of empirical burning rate laws; therefore, the kind of fundamental difficulty just mentioned does not arise.

Brown et al.<sup>10</sup> also use a single-step surface kinetics description to describe all propellants, so that composite and double-base types are not distinguished. The importance of the surface kinetics description has already been discussed; as was explained, the single-step treatment seems inadequate.

Still another approach has been proposed by Krier, T'ien, Sirignano, and Summerfield.<sup>11</sup> These authors have raised objections to the premixed flame treatment used by Denison and Baum<sup>12</sup> to describe the gas-phase reaction process, and they have developed an alternative approach based on the postulate that gas-phase reactions are independent of the local temperature. They assume that the gas-phase reaction rate is uniform (independent of  $x, t$ ) and then show that the heat transfer from the gas phase to the propellant surface is

$$-k \left( \frac{\partial T}{\partial x} \right)_{gw} \approx \frac{1}{r} \left( \frac{k \epsilon_r Q_r \rho_g / \rho_s}{c_g \tau_c} \right)$$

where  $\tau_c$  is a characteristic reaction time. The next step is to assume that the foregoing expression can be written:

$$-k \left( \frac{\partial T}{\partial x} \right)_{gw} = \frac{\varphi(p)}{r}$$

and  $\varphi(p)$  is evaluated from the steady state by noting that:

$$\varphi(p) = \bar{r} \left[ -k \left( \frac{\partial T}{\partial x} \right)_w \right]$$

and that  $\bar{r} = \bar{a} \bar{p}^n$ ;  $-k \left( \frac{\partial T}{\partial x} \right)_w$  can be evaluated from a simple heat balance at the propellant surface.<sup>w</sup>

This analysis appears to have several fundamental weaknesses, foremost of which is the fact that it again relies on the empirical steady-state burning rate law to evaluate the transient behavior of the gas-phase reactions. In fact, if one assumes that the gas-phase reactions are independent of  $x$  but not  $t$ , then the development outlined above leads to:

$$-k \left( \frac{\partial T}{\partial x} \right)_{gw} = \frac{\varphi(p, t)}{r}$$

and it is impossible to evaluate  $\varphi(p, t)$  from a steady-state empirical expression. In addition, the assumption that gas-phase reaction rates are independent of the local temperature is difficult to accept.

Krier et al.<sup>11</sup> also use a single-step surface kinetics treatment, similar to that of Brown et al.<sup>10</sup> Therefore, previous comments concerning the surface kinetics apply here as well. Because of the modifications in the gas-phase treatment, both of these analyses yield results that are qualitatively the same as those given by the present analysis, with a different kinetics treatment, for composite propellants; i.e., it is predicted that surface-coupled exotherms will tend to destabilize the propellant combustion process. Also, despite substantial differences in the combustion models, all of these analyses characterize the response in terms of two or three parameters, as mentioned before.

Experimental studies on nonacoustic instability recently initiated by Beckstead and Culick<sup>16</sup> promise to be very illuminating concerning the capabilities of various theoretical approaches. They have found that the present analysis, for example, is able to correlate their data from propellants with polyurethane binders reasonably well. On the other hand, none of the available theories was successful with other binders, suggesting that some significant mechanism may yet be missing from all existing theories.

#### Modified Combustion Model and Nonlinear Theory

As has been noted, the linear theory discussed above is useful primarily as a means of conveying the general features of the combustion model. However, to obtain a quantitative comparison with finite-amplitude combustion oscillations such as those observed in the present axial-mode instability studies, it is necessary to account for nonlinear effects in the analysis. For this purpose, a computer program based on the nonlinear equations of the model has been developed. This computer program

incorporates a slightly modified and somewhat more sophisticated version of the combustion model. The modified model is discussed below, and the equations describing this model, from which the computer program was developed, are summarized in Appendix B.

#### Predicted Steady-State Behavior of the Flame Temperature

Unlike many other combustion models, the model summarized in the previous sections of this report predicts that the gas-phase flame temperature will increase as the burning rate rises, even in steady-state combustion. This behavior is a consequence of the surface-coupled reaction kinetics employed in the model, as will become evident from a careful examination of Eq. 10.

In steady-state combustion, the net heat flux into the unreacted solid propellant is equal to the energy required to condition the propellant for surface pyrolysis; i.e.,  $-k(\partial T/\partial x)_w = \rho_s r c_s (T_w - T_o)$ . Thus, in the steady-state limit, Eq. 10 becomes a simple expression for the gas-phase flame temperature in terms of the total heat release in the combustion process:

$$c_p (T_f - T_o) = \rho_s r [\epsilon_r Q_r + H_H \left( \frac{p}{T_w} \right)^m e^{-E_H/RT_w} + H_D e^{-E_D/RT_w} - L] \quad (14)$$

The first term within the brackets of this equation represents the heat release associated with combustion in the gas-phase flame; the next two terms describe, respectively, pressure-sensitive (heterogeneous) and pressure-insensitive energetic surface-coupled reactions; the last term represents the latent heat of phase change or decomposition near the burning surface. As the burning rate increases, so does  $T_w$  (See Eq. 2). Thus, the magnitude of the surface-coupled heat release increases with burning rate, and it follows from Eq. 14 that  $T_f$  rises as well. For a reasonable choice of parameters such as  $E_H$  and  $E_D$ , a large change in pressure (and therefore burning rate) may lead to a greater increase in  $T_f$  than is normally encountered with actual propellants. (Composite propellants typically exhibit a modest increase in flame temperature with pressure up to about 200 psi, after which  $T_f$  is almost constant.

Double-base propellants often have a somewhat greater dependence of flame temperature on pressure in steady-state combustion.)

The characteristic just described suggested that a modification of the model was in order, because the accuracy with which the model predicts the steady-state behavior of all dependent variables may be regarded as a legitimate test of its applicability to nonsteady phenomena. In general, the model in the form presented above will not yield the exact steady-state behavior of flame temperature versus pressure for a given propellant unless certain restrictions are imposed on the numerical values assigned to kinetic parameters such as  $E_H$  and  $E_D$ . This situation is not entirely satisfactory, because the flame temperature is actually a purely thermodynamic quantity, determined primarily by the heat of reaction of the propellant; it is quite independent of the reaction kinetics. (Note that  $T_f$  is normally obtained from an "adiabatic flame temperature" calculation, in which the propellant composition and heats of reaction appear but not the kinetics parameters.<sup>17</sup>)

To identify the source of this apparent anomaly in the combustion model, it will be helpful to re-examine the theoretical description of gas-phase and surface-coupled heat release in the combustion process. A brief study of the steady-state combustion mechanism will reveal a minor but potentially important correction that should be introduced into the model to overcome the difficulty described above, and it will also clarify the physical basis for the surface kinetics treatment that in earlier discussion was shown to be the most important feature of the model.

#### Theoretical Description of the Distribution of Heat Release in Solid Propellant Combustion

The solid propellant combustion mechanism is illustrated in Fig. 4. It is convenient to envision the propellant as moving at a negative velocity, equal to the burning rate, toward the surface zone ( $x = 0$ ) where pyrolysis occurs; the pyrolysis products then proceed into the gas phase where further reactions complete the combustion and the final flame temperature  $T_f$  is achieved. During this process the total heat

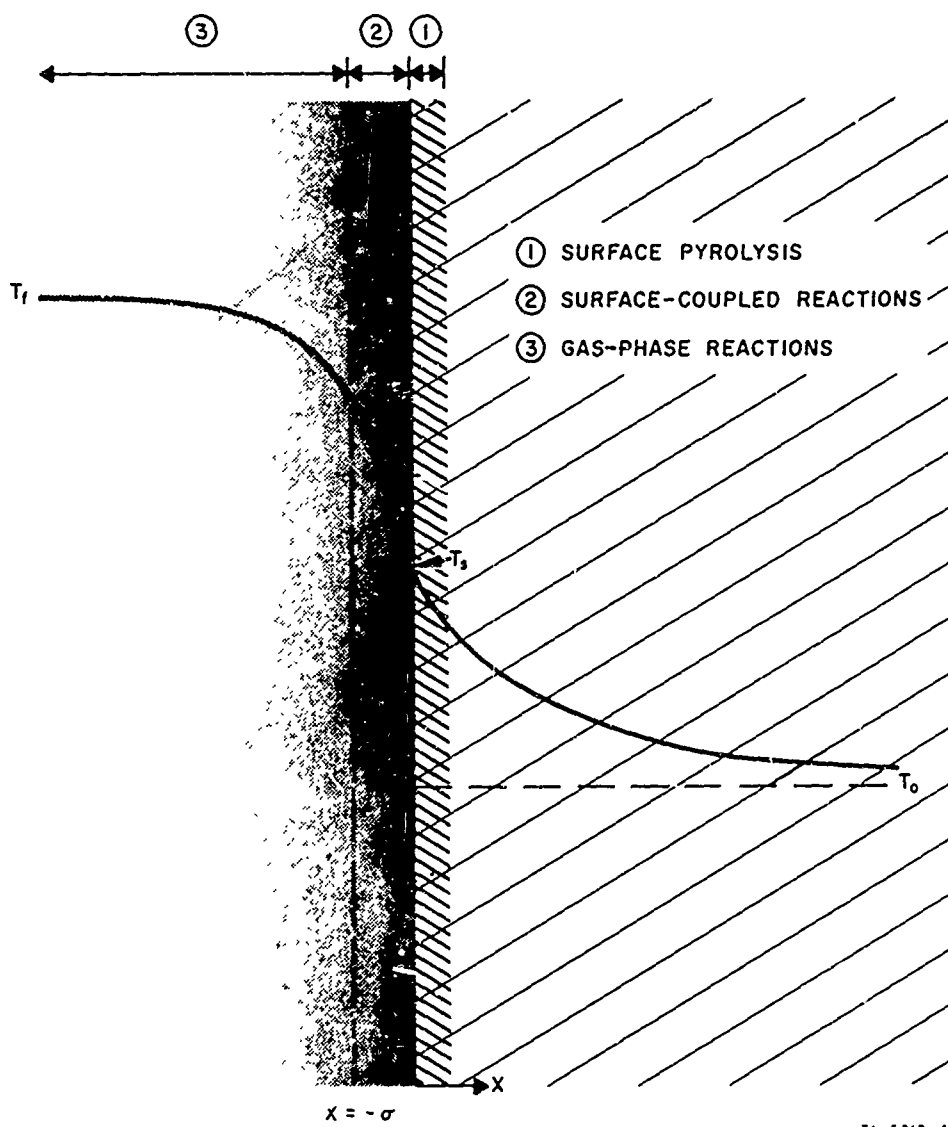


FIG. 4 SIMPLIFIED MODEL OF THE DISTRIBUTION OF HEAT RELEASE IN THE SOLID PROPELLANT COMBUSTION PROCESS

release per unit area of propellant surface, and per time, is  $\rho_s r Q$ , where  $Q$  is the total heat of combustion of the propellant. Of this total, a portion,  $\rho_s r Q_s$ , is released within a relatively narrow pyrolysis region near the surface of the solid; i.e.,  $Q_s$  is the heat of decomposition of the propellant. In a typical AP-type composite propellant,

for example,  $Q_s$  would be essentially the heat of decomposition of AP. The pyrolysis products then initiate a very complex sequence of reactions, which occurs in a zone extending from the propellant surface into the gas phase for whatever distance is required to complete combustion. The thickness of the gas-phase flame zone depends on both the total mass flux  $\rho_s r$  and the kinetics of the reactions within this zone. For example, as the pressure increases the local reactant concentration rises, causing an increase in the local reaction rates. Thus, at higher pressures the reactions are accomplished more rapidly and the flame zone is thinner, as is well known.

To express the total heat release in the combustion process in terms of that associated with each of the constituent reactions, it is convenient to define a parameter  $\epsilon$ , which is essentially a measure of the "completeness" of combustion. Specifically, the concentration of reactants entering any given reaction plane in the flame zone, such as  $x = -x_1$ , is  $\rho_s r [1 - \epsilon(x_1)]$ . At the gas-solid interface  $\epsilon \ll 1$ , because the flow at that point consists almost entirely of pyrolysis products that are available for further reactions. As the distance from the propellant surface grows greater,  $\epsilon$  increases, since more and more combustion products are present and the concentration of potential reactants is less. The position at which  $\epsilon = 1$  marks the edge of the flame zone; i.e., when  $\epsilon = 1$  there are no more reactants, combustion is complete, and the flame temperature has been achieved.

This visualization of the combustion process leads to the following relatively simple expression for the total heat release per unit time and surface area:

$$\rho_s r Q = \rho_s r Q_s + \rho_s r \int_0^{-\infty} H(x) [1 - \epsilon(x)] e^{-E(x)/RT(x)} dx \quad (15)$$

As was noted above, the concentration factor  $\epsilon$  is a function of  $x$ , changing from nearly zero at the propellant surface to unity at the edge of the flame zone. In addition, the local heat of reaction  $H$ , the local activation energy  $E$ , and the temperature  $T$  vary with  $x$ . All of these variables depend on the specific sequence of reactions involved

in the process; at any given position  $x_1$ , the quantities  $H$  and  $E$  characterize the particular reaction occurring at that point, whereas  $\epsilon$  and  $T$  reflect the history of reactions closer to the surface. To perform the integration of Eq. 15 it would be necessary to assume a specific reaction sequence and solve the conservation equations to determine the concentration and temperature profiles. This would be a formidable task, hardly justifiable or even possible in view of the general lack of information about reactions in the flame zone. Nevertheless, Eq. 15 suggests some interesting and useful concepts for the combustion model.

First, note that Eq. 15 expresses the total heat release in terms of the constituent reactions in either steady or nonsteady combustion. Second, note that as the general temperature level rises, as when the burning rate or pressure increases, the integral is completed over a shorter distance; i.e., the flame zone is thinner. Alternatively, as the temperature increases, a greater fraction of the total heat release occurs within an arbitrarily narrow zone of thickness  $\sigma$  (Fig. 4) near the surface. This observation is important in nonsteady combustion, because those reactions near the surface will be "surface-coupled," or governed primarily by the relatively slow thermal response of the solid, whereas those farther out in the flame zone will follow the much faster thermal response of the gas. It is this aspect that led to the unique kinetics description of surface-coupled reactions employed in the SRI theory, as will be demonstrated below.

#### Modification of the Combustion Model

In principle the combustion model should contain the right-hand side of Eq. 15 in place of the first and the last two terms of Eq. 10, which represent the gas-phase and the surface-coupled heat release, respectively. However, in this form the combustion model would almost exclude the possibility of reasonable mathematical analysis, as was explained in connection with Eq. 15. Therefore, it is necessary to introduce a major simplification while retaining those features of Eq. 15 that are of primary importance in both steady and nonsteady combustion.



This simplification is accomplished by dividing the flame zone into two regions: one relatively thin zone adjacent to the propellant surface (e.g., the zone of thickness  $\sigma$  in Fig. 4) and the other occupying the remainder of the flame zone. Reactions in the first zone occur practically at the surface temperature  $T_w$ , and in nonsteady combustion the temperature profile in this region tends to be in phase with  $T_w$ ; i.e., it is dominated by the thermal response of the solid phase. This is the zone of surface-coupled reactions and it is characterized by the fact that  $\epsilon \ll 1$ . The other zone encompasses the "true" gas-phase reactions, or those that follow the faster thermal response of the gas phase. With this approach Eq. 15 takes the following much simpler form:

$$\rho_s r Q = \rho_s r \left\{ Q_s + \int_{x=-\sigma}^{-\infty} H(x) [1 - \epsilon(x)] e^{-E(x)/RT(x)} dx \right\} + \rho_s r H e^{-E/RT_w} \quad (16)$$

A comparison of Eq. 16 with Eq. 10 shows that the last term of Eq. 16 represents the surface-coupled heat release; this term has been separated into two parts in the combustion model: one describing pressure-sensitive or heterogeneous reactions, and the other those that are pressure insensitive. The bracketed quantity in Eq. 16 is clearly identified with  $Q_r$  in Eq. 10.

This comparison reveals at once the modification that should be introduced into the model for application to nonlinear behavior. In the model,  $Q_r$  has heretofore been treated as a constant, whereas Eq. 16 shows that it may vary. The way it varies for a given propellant is determined by the behavior of the total heat of reaction  $Q$  which can be determined from thermochemical calculations. (In fact, knowing the dependence of  $Q$  on pressure in steady combustion is equivalent to knowing the behavior of the flame temperature  $T_f$ .) If  $Q$  is known, then for any value of the last term in Eq. 16,  $Q_r$ , which corresponds to the quantity in brackets, is also known. Thus, for large excursions in the pressure or burning rate,  $Q_r$  should be treated as a variable such that in the

steady-state limit the dependence of the flame temperature on the pressure is as predicted by thermochemical calculations. Note that this method of ensuring a correct flame temperature behavior in the model involves only the heats of reaction and is completely independent of the kinetics parameters, such as  $E_H$  and  $E_D$ . In this way the objection raised earlier in this report, relevant to the original form of the model, is completely overcome.

For the nonlinear analysis, obtained from the computer program outlined in Appendix B, the modified combustion model with variable  $Q_r$  is used. Inasmuch as the foregoing discussion has centered on steady-state combustion, a brief commentary on the methods of modifying the model for a nonsteady analysis follows.

In general, the behavior exhibited by Eq. 16 or Eq. 10 with a variable  $Q_r$  is as follows: As the burning rate and surface temperature rise, the amount of surface-coupled heat release increases. Normally, the total heat release increases too, but only slightly. Therefore,  $Q_r$  must decrease as the surface terms increase to preserve the correct total heat release  $Q$ . The dependence of the surface terms on  $T_w$  or on the burning rate (see Eq. 2) is known. The dependence of the adiabatic flame temperature, and therefore of  $Q$ , on the pressure (or the burning rate or  $T_w$ ) is known from thermochemical calculations. The difference between  $Q$  and the surface terms is  $Q_r$ , and the thermochemical calculation establishes a unique value of  $Q_r$  for every value of  $T_w$  and the surface terms.

It appears reasonable to assume that in nonsteady combustion the heat release in the gas phase  $Q_r$  will be the same as the steady-state value for the same total heat release in the surface-coupled terms. Note that this assumption does not relate  $Q_r$  to the instantaneous value of  $T_w$  or  $p$ , but to the instantaneous heat release, thereby preserving the thermochemical characteristics of the propellant. In the steady-state limit this assumption reduces to the correct behavior, as described above.

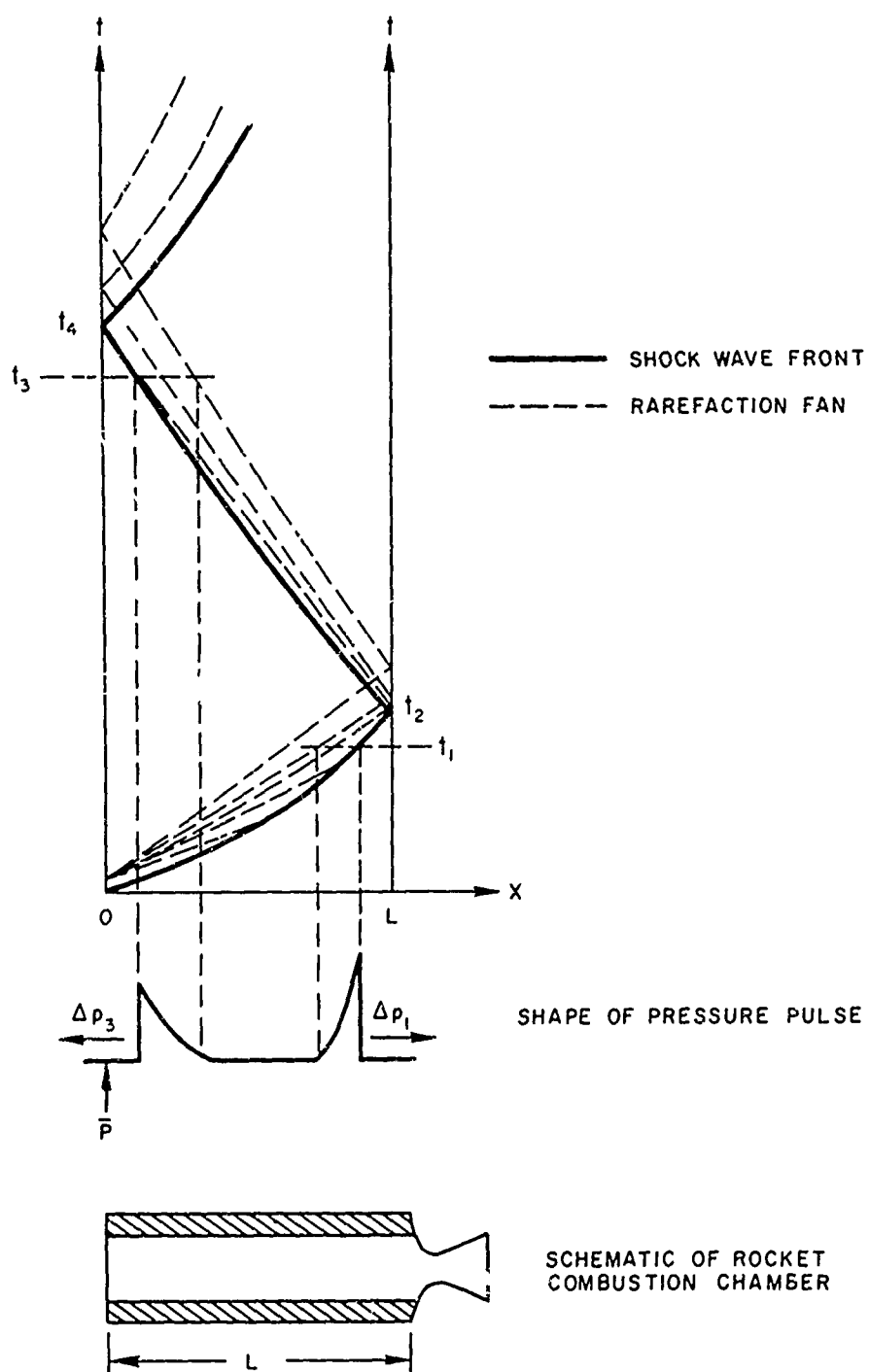
### Mechanism of Interaction Between Propellant Response and Shock Wave

The theoretical discussion up to this point has been concerned primarily with the response of the propellant combustion mechanism to pressure pulses which are induced at any given point on the burning surface by a traveling shock wave as it passes over that point. The combustion model that evolved from this study has led to an interpretation of traveling wave combustion instability data, in terms of the theoretically predicted response characteristics of various propellant types; i.e., it has been shown that propellants with a predicted high-amplitude response will support axial-mode, traveling-wave instability, whereas those having a low-amplitude response will result in the rapid decay of any shock wave imposed on the combustion chamber.<sup>2</sup> This theory correctly interprets instability observations with both composite and double-base propellants, which behave quite differently.

Despite the success of the correlation between theory and experiments, the theoretical explanation of axial-mode, traveling-wave instability is not yet complete. Still needed is a clarification of the interaction mechanism by which the burning rate response of the combustion process can support the traveling shock wave, causing combustion instability. A qualitative understanding of this interaction process can be obtained with the aid of a simplified x-t wave diagram for the rocket motor situation.

To clarify the mechanism of finite-amplitude axial-mode instability, assume that a shock wave is introduced into the combustion chamber by some unspecified disturbance. For example, a mechanical failure of a small section of the propellant or restrictor might temporarily block the nozzle. Whatever the initiation mechanism, it can be assumed to have essentially the same effect as would the impulsive forward movement of a piston at the same position, followed by a sudden termination of movement. The result would be to send a shock wave traveling down the combustion chamber, closely followed by a rarefaction wave.

Figure 5 depicts the situation when there is no interaction between the wave and the response of the burning rate to the pressure jump



TA-5818-59

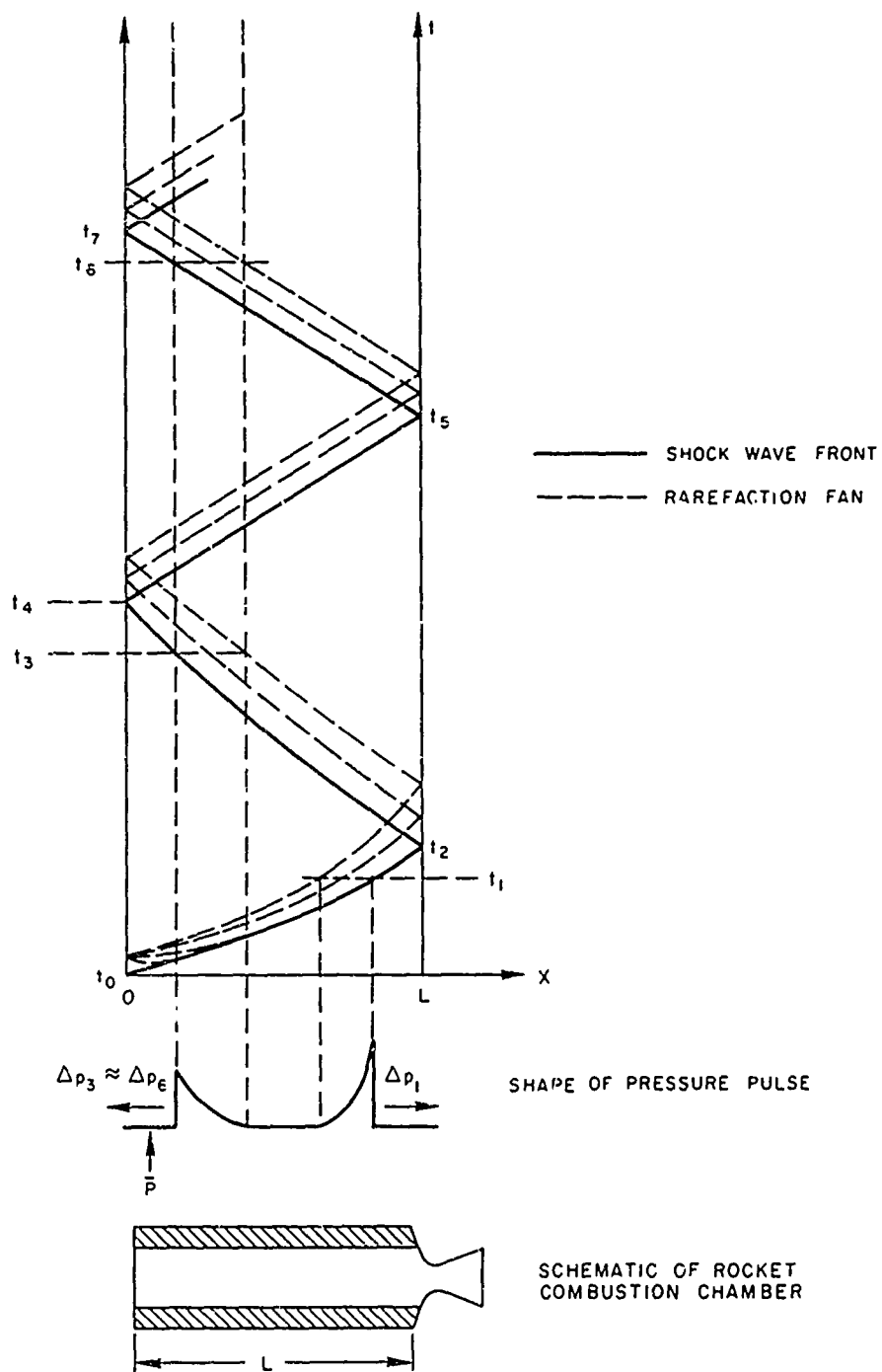
FIG. 5 WAVE DIAGRAM OF A TRAVELING SHOCK WITH NO COMBUSTION SUPPORT

associated with the wave front. Thus, the wave diagram of Fig. 5 corresponds to the case of a very weak propellant response (low response function), or to a maximum response frequency that is far different from the frequency of passage of the wave over any given point on the surface. In this illustration the shock wave is initiated at the head end of the motor, as it was in the experimental studies during this program. (In those experiments an explosive pulse at this position created the traveling shock wave.) A rarefaction wave forms just behind the shock. Assuming that the initial particle velocity toward the nozzle is small, the particle velocity behind the shock is always in the direction of shock movement. Therefore, the rarefaction front, which moves relative to the motor with sonic velocity plus the local particle velocity, will overtake the shock front. The effect of the rarefaction fan is to attenuate the shock wave and broaden the pressure pulse as it travels toward the nozzle. Thus, one might imagine a shock wave initially moving at a Mach number  $M = 3$  near the head end and approaching the nozzle at  $M = 2$ .

The shock attenuation process decreases the shock velocity and appears on the  $x-t$  wave diagram as a curvature of the shock path. The pressure pulse waveform, as a function of time of travel, is illustrated below the wave diagram. At time  $t_1$ , just before the shock reaches the nozzle, the pressure pulse comprises a sharp rise  $\Delta p$  at the shock front followed by a pressure decay through the rarefaction fan. At time  $t_2$  the shock wave and the rarefaction are reflected from the nozzle entrance, with a further loss of strength. As the wave travels back toward the head end, the rarefaction continues to diminish the shock strength and also tends to extend over an ever-increasing region behind the shock. Thus,  $\Delta p_3 < \Delta p_1$  and at time  $t_3$  the rarefaction zone is broader. Owing to the continual decay of shock strength, each successive passage through the chamber takes longer (e.g.,  $t_4 - t_2 > t_2$ ), until finally the shock disappears altogether. In a rocket motor of typical dimensions with a propellant that responds only weakly to pressure disturbances, this attenuation ordinarily will require only a few passes of the shock system over the length of the grain.

Consider next the same process, but with one important modification: it is now assumed that the combustion mechanism responds to pressure pulses with a sharp increase in burning rate, as indicated by the theory discussed previously. This situation can arise in an actual motor if two considerations are fulfilled: (1) the propellant response function must have an appreciable amplitude at the resonant frequency (or frequency of maximum response), and this depends on the thermochemical characteristics of the propellant (see Fig. 2); (2) the frequency at which the shock front passes a point on the propellant surface must be reasonably close to the resonant frequency, so that the burning rate response will be large enough to interact significantly with the shock wave. Realization of this condition depends mainly on the geometry, or more specifically on the characteristic length dimension of the combustion chamber. In all cases the wave velocity is about the same, since the Mach number of the traveling shock wave tends toward a value in a relatively narrow range ( $1 < M < 1.4$ ). Therefore, the frequency of passage over a given point is, to first order, inversely proportional to the chamber length.

Figure 6 illustrates the traveling wave process when there is a significant propellant combustion response to the passage of a pressure jump. It is convenient to assume that at time  $t = 0$  on this diagram the wave has already completed several passes through the chamber and has undergone a certain degree of attenuation, as discussed in connection with Fig. 5. During this period the wave passes back and forth over the grain at a frequency near the resonant (or peak response) frequency of the propellant. Thus, each point on the grain is subjected to a periodic pressure jump, followed by a decay; the actual frequency will vary with axial position, but will be near the resonant frequency over most of the surface if the chamber length  $L$  is within a certain critical range. Note too, from Fig. 3, that the phase angle is very small near the resonant frequency. Thus, the first few passes of the shock wave will establish a periodic perturbation in the burning rate or a traveling mass source that tends to move along with the shock; also, because the phase angle is small the peak burning rate response will be very close to the shock front.



TA-5816 58

FIG. 6 WAVE DIAGRAM OF A TRAVELING SHOCK WITH COMBUSTION SUPPORT THROUGH MASS ADDITION

The effect of a sudden jump in the mass addition at the surface just behind the shock is to create compression waves which travel along the local characteristic lines. The compression waves tend to counteract the rarefaction wave, and reinforce the shock wave. A physical interpretation of this shock interaction mechanism may be deduced by noting that the sharp increase in mass flux over an annular surface zone behind the shock front, corresponding to a traveling annular mass source, has the effect of constricting the axial flow behind the shock front or of diverting this flow toward the center of the chamber. Essentially the same effect would be achieved by driving an annular ring or a piston with a hole in the center along behind the shock front. Compression waves emanating from the motion of this annular piston would tend to support the shock wave and alter the particle velocity distribution behind it so that the rarefaction wave would overtake the shock more slowly.

On the wave diagram of Fig. 6 the effect of the traveling mass source is to bend the rarefaction fan and the shock path away from each other. Finally, if the mass source is strong enough (i.e., if the propellant response is great enough) an equilibrium condition is achieved; the mass source causes the flow a very short distance behind the shock wave to become sonic relative to the shock front. When this happens the rarefaction wave is moving at the same velocity as the shock front and cannot attenuate it further. This situation arises when the shock path and the rarefaction front are parallel on the wave diagram.

In Fig. 6 the shock wave, which was initiated some time prior to  $t_0$ , is still decaying as it travels toward the nozzle ( $t_0 < t < t_2$ ). The pressure waveform at time  $t_1$  is illustrated. Throughout this period the traveling mass source, corresponding to the propellant response, follows essentially the same path as the shock front and reinforces the shock wave. Some time just after  $t_2$  in the wave diagram, the rarefaction wave is completely compensated for by the compression waves from the traveling mass source, so that the shock front and the rarefaction follow parallel paths. From then on the shock system continues unabated, with essentially a constant waveform. (Note that the waveforms at  $t_3$  and  $t_4$  are identical.) This situation corresponds to finite-amplitude, axial-mode combustion instability.



To translate the foregoing qualitative description of the shock interaction mechanism into precise quantitative terms requires a rather complex and tedious, though straightforward, numerical calculation using the method of characteristics in three dimensions, or in two dimensions if the chamber is cylindrically symmetric. A one-dimensional treatment based on the method of characteristics similar to that described by Mirels<sup>18</sup> would provide an approximate description of the flow field behind the shock front, indicating how the wall mass perturbation leads to compression waves which, in turn, reinforce the shock wave. From such an analysis, for example one could construct quantitative, though not very accurate wave diagrams such as those illustrated in Figs. 5 and 6. For the present application, wherein the propellant response can be predicted only in a very approximate way, the method of characteristics seems an inappropriate way to analyze the interaction mechanism. A less complicated approach, even if less precise, would be more suitable.

A simple and adequately precise description of the interaction process may be obtained by observing that the effect of the traveling mass source, or annular piston, behind the shock wave is similar to the role of exothermic chemical reactions in supporting a detonation wave. Of course, in the latter the energy release may be assumed to be uniformly distributed over a cross-section behind the shock front, which permits the use of a simple one-dimensional treatment. In the situation of present interest, the pressure signal is transmitted through a complicated, cylindrically symmetric (two-dimensional) flow field from the annular mass perturbation to the shock front. However, if the transmission time for this signal is small relative to the characteristic time for the expansion process behind the shock wave, a one-dimensional analysis is appropriate as a first approximation. In the experimental studies performed during this investigation (summarized in later sections of this report), the rarefaction wave had a characteristic time of about 2 msec. The time for a pressure signal emanating from the propellant surface to reach the centerline of the 4-in. chamber, assuming a sonic velocity of 3000 ft/sec in the hot combustion gas, is approximately

0.05 msec, or more than an order of magnitude less than the rarefaction time. Accordingly, an analysis similar to the usual treatment of detonation wave propagation will provide a valid first-order description of the interaction mechanism that drives the shock wave in axial-mode instability. Such an analysis is presented in Appendix C, where the analogy between the mechanisms driving a shock wave and a detonation wave is explained in greater detail.

Equation C11, Appendix C, determines the perturbation  $m'$  in the total mass flux that must occur behind a shock wave moving at Mach number  $M$  to make the flow behind the shock sonic relative to the shock front, as in a detonation wave. The result is expressed in terms of the ratio  $m'/\bar{m}$ , where  $\bar{m}$  is the mass flux through the shock plane in a coordinate system moving with the shock;  $m'/\bar{m}$  vs.  $M$  is shown in Fig. 7.

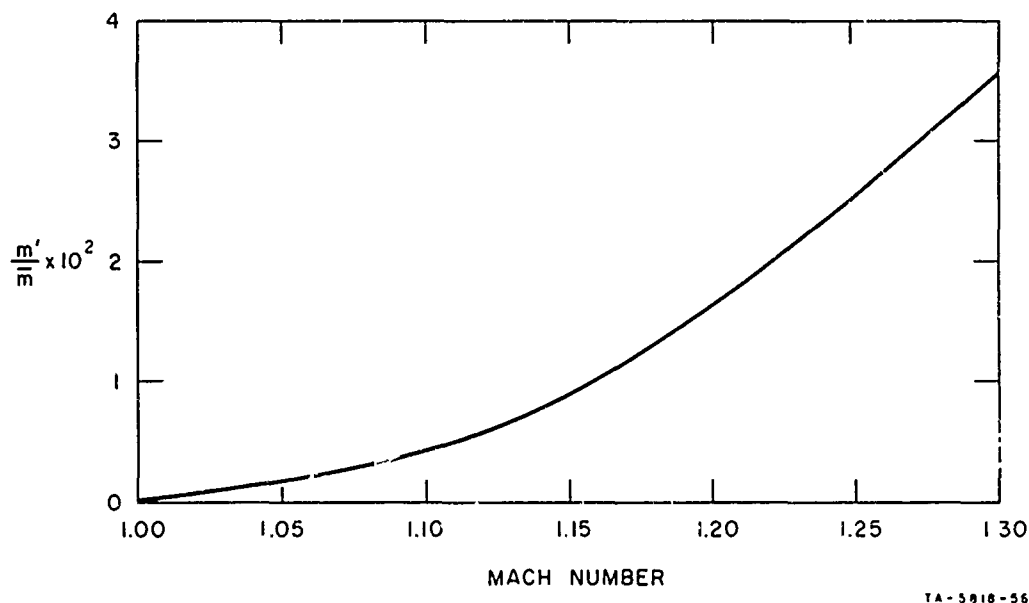


FIG. 7 MASS ADDITION PERTURBATION REQUIRED TO SUPPORT A TRAVELING SHOCK

To illustrate the implications of Fig. 7, it will be useful to make an order-of-magnitude estimate of the kind of propellant response that could cause axial-mode, traveling-wave combustion instability in a typical solid rocket motor. Consider a shock wave traveling at  $M = 1.2$ , which is typical of such instability. According to Fig. 7, the corresponding value of  $m'/\bar{m}$  is about 0.016, where  $m'$  is the mass added behind the shock by a burning rate pulse that extends over an annular surface of length  $\ell$  and  $\bar{m}$  represents the mean flow through the motor provided by the average burning rate acting over the full motor length  $L$ . Pressure measurements discussed in a later section of this report show that in a motor of typical dimensions (e.g.  $L \sim 40$  to  $80$  in.) the length of the rarefaction zone is of the same order as  $L$ . The shape of the wave profile shows a rarefaction following very closely behind the shock, indicating that the influence of the effective mass source  $m'$  is felt over a length  $\ell$  that is small in comparison with the rarefaction length. Thus, as an order-of-magnitude estimate,  $L/\ell \sim 10$ . Since

$$\frac{m'}{\bar{m}} = \frac{r - \bar{r}}{\bar{r}} \frac{\ell}{L} = \tilde{r} \frac{\ell}{L}$$

it follows that  $\tilde{r} \sim 10 \cdot 0.016 = 0.16$ . For typical propellants  $\tilde{v} \sim 0.3$ , and for  $M = 1.2$ ,  $\tilde{p} \sim 0.15$ . Thus the minimum response function of the propellant that will cause traveling wave instability is  $1/\sqrt{\tilde{m}/\tilde{p}} \equiv 1/\sqrt{\tilde{r}/\tilde{p}} \sim 3.6$ .

This estimate is approximate, of course, and tends to be conservative. For example, the ratio  $L/\ell$  should be essentially equivalent to the ratio of the rarefaction time to pressure-wave transmission time from the propellant to the center of the shock plane. According to the earlier estimate of this ratio, it would follow that  $L/\ell \sim 40$ , in which case the minimum response function for combustion instability would be about 14. In general, one can conclude that any propellant with a response function less than 3 to 4 is very unlikely to exhibit traveling wave instability, whereas with a response function on the order of 10 or more the probability of this kind of instability is relatively high. Both the response function

theory summarized in previous sections of this report and experimental measurements in the T-burner<sup>10</sup> indicate that this range is representative of real propellants.

### III. EXPERIMENTAL STUDIES

The experimental studies carried out under this program consisted of differential thermal analysis (DTA) measurements, fiber-optic studies of the solid propellant combustion zone, and studies of the growth and decay of finite traveling pressure waves that were induced in cylindrical and slab motors by the firing of a black powder pulse at the head end.

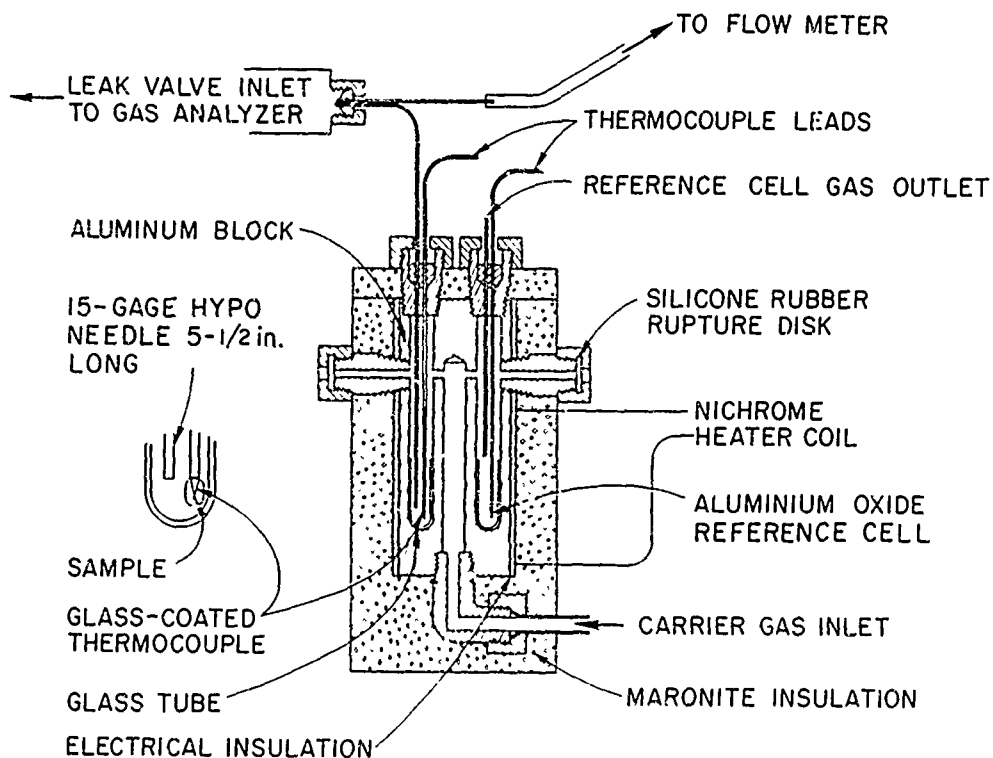
#### Differential Thermal Analysis (DTA) of Propellants

The theoretical combustion model that has been developed at SRI predicts a sizeable influence of surface-coupled heat release on the transient burning behavior. The present DTA studies, combined with mass spectrographic analysis of gaseous decomposition products, were used to differentiate between gas-phase and solid-phase reactions that might occur during the decomposition of AP and potassium perchlorate (KP) based propellants. These studies were performed at a series of pressures ranging from 1 to 70 atm.

A DTA cell designed to operate at elevated pressures was fabricated; its detailed construction is shown in Fig. 8. The cell is fitted with safety rupture diaphragms. The gaseous decomposition products can, when desired, be ducted to an analytical mass spectrometer. In the studies performed, a quadrupole residual gas analyzer (Electrical Associates Incorporated, Quad 210) was used.

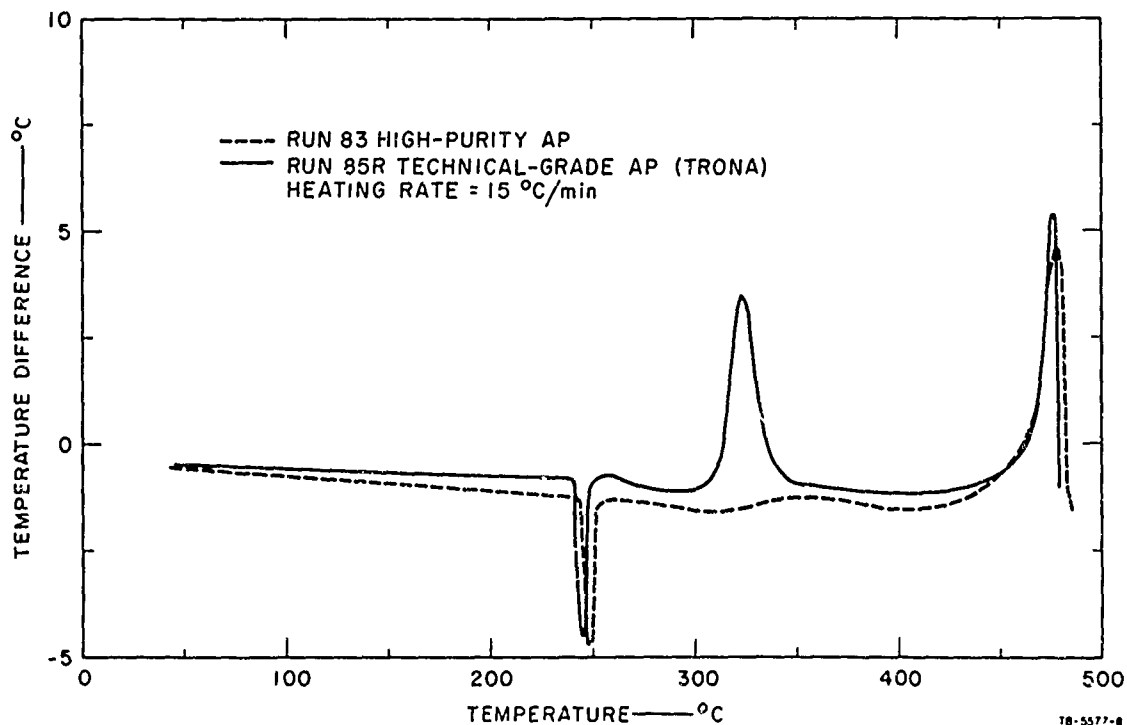
Initial experiments were carried out at atmospheric pressure. The first point to be investigated was the effect of AP purity on the DTA of AP. Figure 9 shows the DTA results on technical-grade and high-purity AP analyzed, as indicated in Table I. It is seen that technical-grade AP gives an initial decomposition exotherm at 325°C which does not appear on the DTA curve for high-purity AP.

In Fig. 10 the DTA results comparing the behavior of high-purity and technical-grade AP in a polyurethane propellant containing 75% AP are given. The DTA responses are almost identical. It appears that



1B-5818-27

FIG. 8 HIGH-PRESSURE DTA CELL



1B-5577-8

FIG. 9 DIFFERENTIAL THERMAL ANALYSIS OF AP

Table I

## COMPARISON OF TECHNICAL-GRADE AND HIGH-PURITY AP

Constituent	High-Purity (%)	Technical-Grade (%)
$\text{NH}_4\text{ClO}_4$	99.8	99.3
$\text{NH}_4\text{Cl}$	0.02	0.10
$\text{NaClO}_3$	Trace	.007
Sulphated Ash	Trace	0.33
Insoluble	.002	0.109
Total Moisture	0.079	0.048
Metal Oxide (Nonalkali)	0.001	--
pH	5	6
Iron as Fe	--	.0002
Tricresylphosphate	--	0.20
Na	( 5 ppm)	(175 ppm)
K	( 4 ppm)	( 55 ppm)

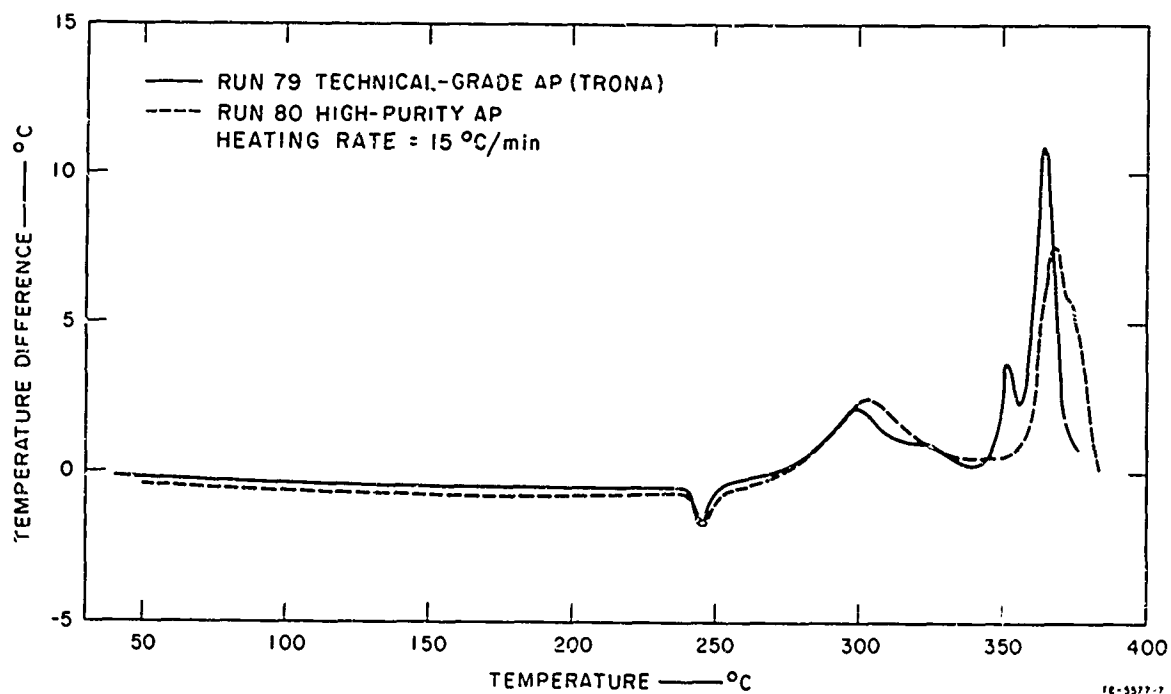


FIG. 10 DIFFERENTIAL THERMAL ANALYSIS OF AP PROPELLANTS

contact with the polyurethane binder caused the exothermic response to be the same in both high-purity and technical-grade AP. One possible reason for this is the solubility of AP in the binder and subsequent catalytic effect of binder impurities. Another may be the presence of exothermic surface reactions in the solid phase between the binder and AP.

Figures 11 and 12 show the DTA thermograms for propellants made from technical-grade AP and high-purity AP, the variable being the lack or presence of FeAA as a binder-curing catalyst. The binder is made from a hydroxy-terminated polybutadiene (PBD) cross linked with TDI. The propellant formulation is given in Table II. An equivalence ratio for diol/triol/NCO of 75/25/107 was used in the binder.

The presence of FeAA in the propellant containing technical-grade AP as a curing catalyst clearly causes the predecomposition exotherm and the final exotherm to occur at a lower temperature, perhaps as much as 30°C lower. When high-purity AP is used in the same formulation, the addition of Fe does not appear to be a significant variable.

The DTA thermograms in Fig. 13 show the interaction of technical-grade and high-purity AP with polypropylene glycol (PPG) 2025, the basic ingredient of many PU formulations. Although the predecomposition exotherms are different, both indicate appreciable reaction exotherms before deflagration occurs. On the basis of these data, there is little likelihood that high-purity AP can be used in a formulation containing PPG 2025 (good commercial quality) to eliminate the predecomposition exotherms; however, it appears to significantly decrease the peak temperature of the exotherm (from 380°C to 320°C).

It is desirable to try to delay the exotherm occurring after the crystal change endotherm in AP to as high a temperature as possible. Since all binders seemed to cause the onset of the exotherm at lower temperatures, it appeared that a compatible coating on the oxidizer might give the desired separation to prevent binder/oxidizer interactions. Accordingly, both technical-grade and high-purity AP were coated with



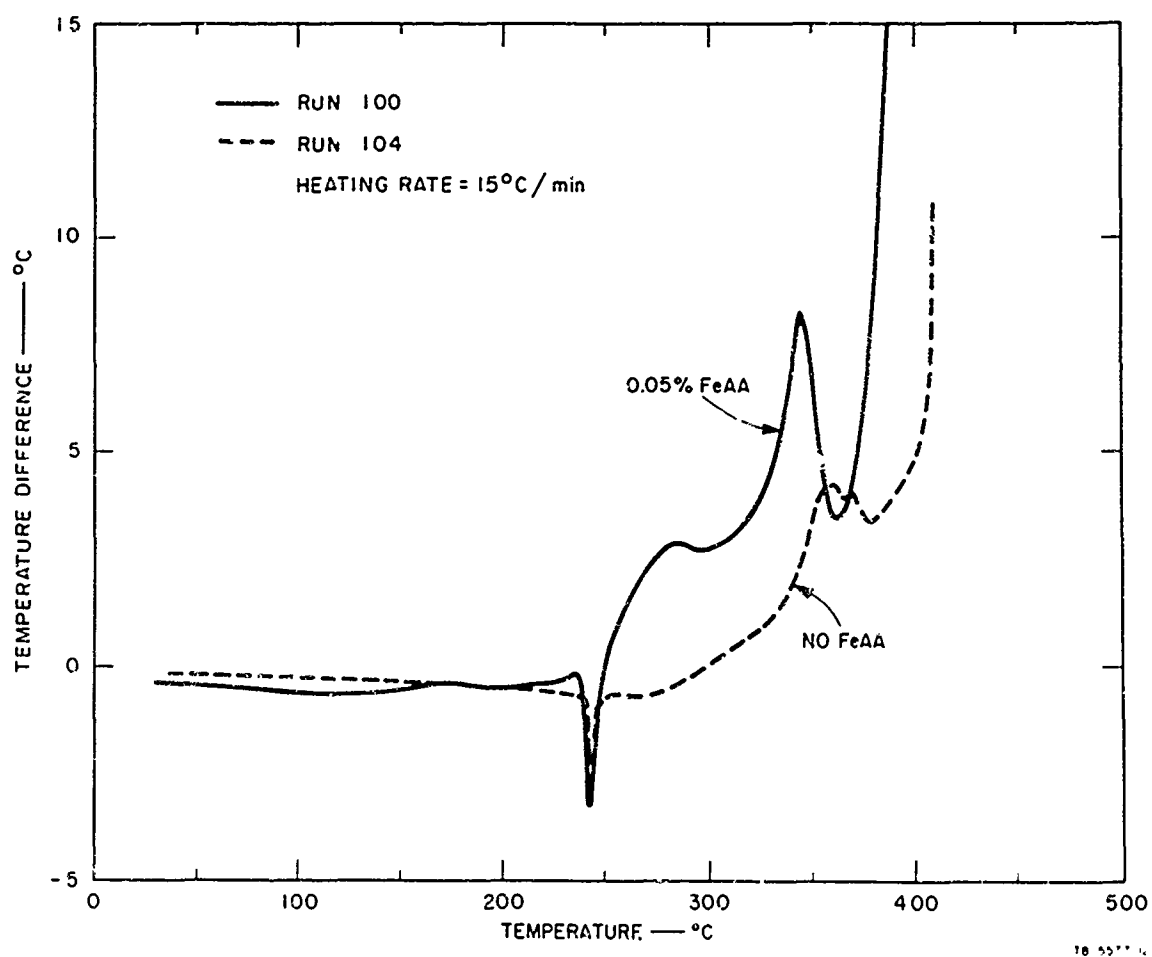


FIG. 11 DTA THERMOGRAMS FOR PBD PROPELLANT WITH TECHNICAL-GRADE AP

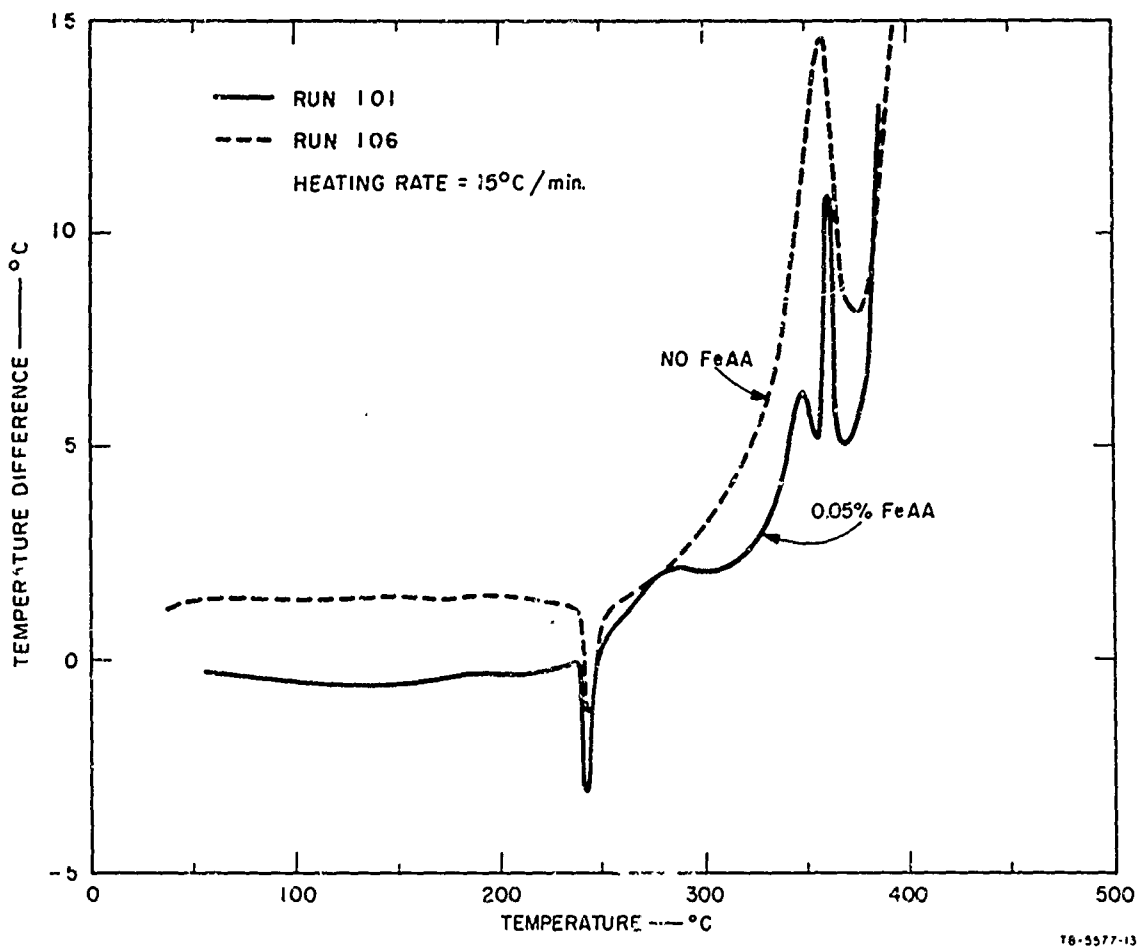


FIG. 12 DTA THERMOGRAMS FOR PBD PROPELLANT WITH HIGH-PURITY AP

Table II  
PBD PROPELLANT FORMULATION

Ingredient	Weight %
Ammonium Perchlorate, 70/30 UG/11 $\mu$	80.00
Sinclair PBD, R45	16.81
LHT 240 (Union Carbide Polyol)	1.23
Tolylene Diisocyanate	1.91
Ferric Acetyl Acetonate (FeAA)	0.05

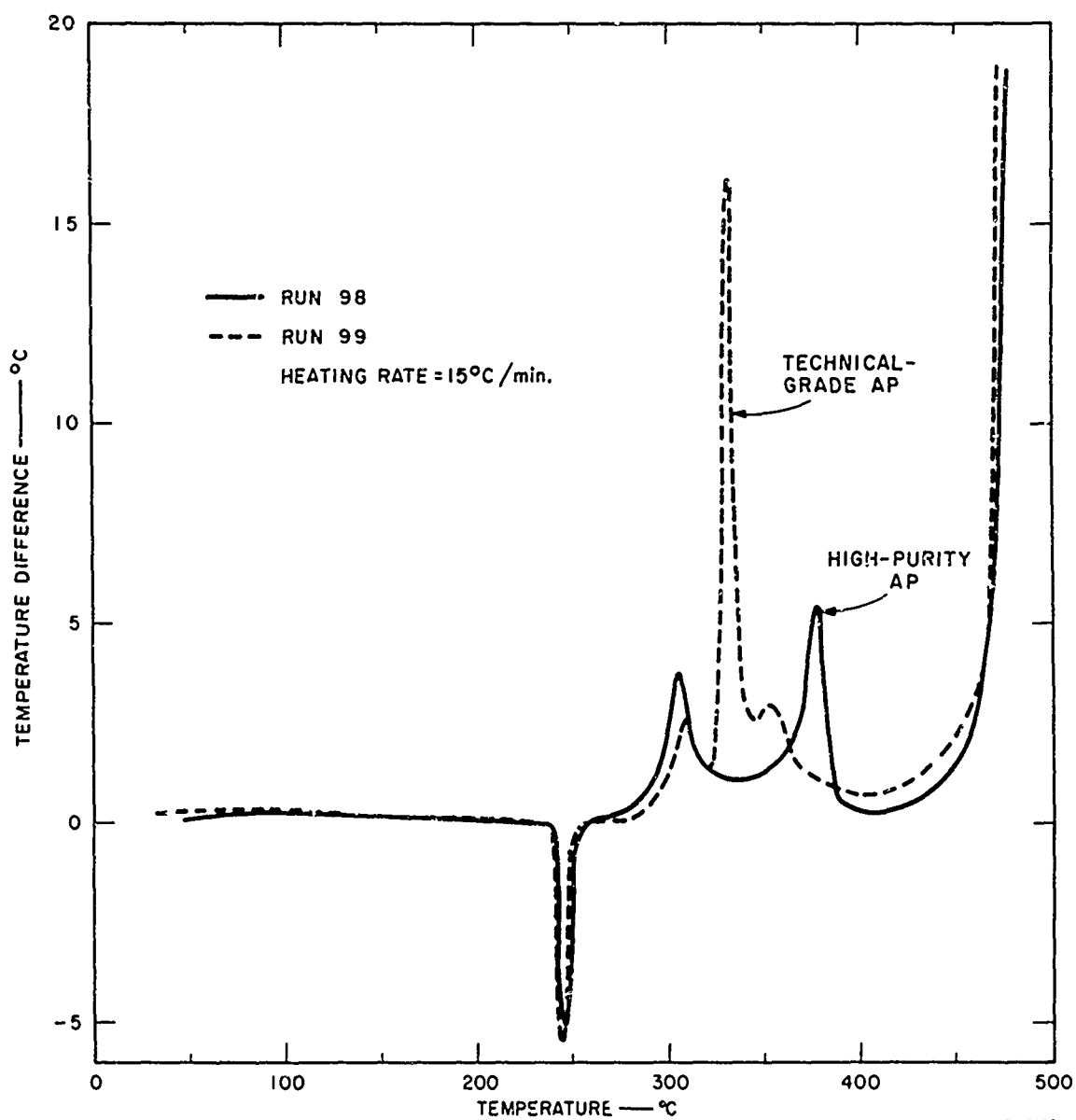


FIG. 13 DTA THERMOGRAMS FOR 80/20 AP/PPG MIXTURES SHOWING EFFECT OF AP PURITY

3% by weight of Viton A\* and 3% of vinylsiloxane.\*\* The resulting thermograms are shown in Figs. 14 and 15. Both delayed the pre-decomposition exotherm of technical-grade AP by only 10°C. Neither caused the early exotherm noted with other binders in contact with high-purity AP, although vinylsiloxane did lower the exotherm to 350°C and Viton A to 395°C from a high of 410°C for the untreated control sample. In propellants, neither treatment was effective on technical-grade AP.

The thermograms for a hydroxy-terminated PBD propellant containing 70% technical-grade AP are shown in Fig. 16. Since the vinylsiloxane coating was easier to apply and made a more fluid propellant, it was formulated into a PBD propellant containing 70% high-purity AP. The thermograms in Fig. 17 show that the onset of the exotherm appears to be displaced almost 50°C higher than for the sample containing uncoated AP.

In Fig. 18, burning rate curves are shown for the propellants listed in Table III. Note that propellants containing 2.5% vinylsiloxane were tested with the additive as a coating on the AP and as a free agent. Since the coated AP propellant exhibits the higher burning rate, it is possible that the energy release and temperature profiles have been modified by the suppression of interfacial heterogeneous reactions. These changes may be reflected in the higher burning rate, since the vinylsiloxane did not function as a catalyst when dispersed in the conventional manner.

With the background data established for ammonium perchlorate at atmospheric pressure, the influence of pressure on DTA thermograms was next studied for a specially prepared propellant. This propellant contained 70% by weight of the highly purified ammonium perchlorate and 30% by weight of a specially purified hydroxy-terminated PBD-based

---

\*Developed by Naval Weapons Center, IDP 1080, Propulsion Development Department, China Lake, California

\*\*U.S. Patent No. 3,190,776, June 22, 1965.

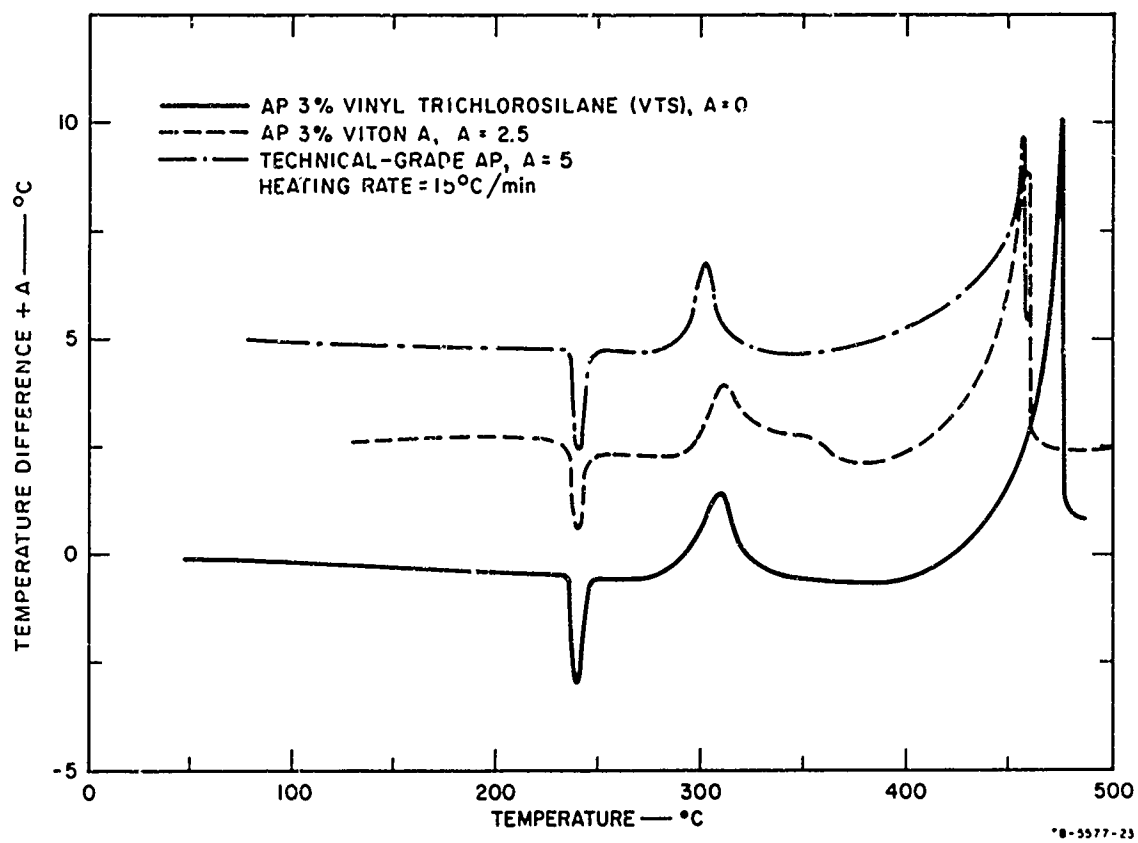


FIG. 14 DTA THERMOGRAMS FOR COATED TECHNICAL-GRADE AP

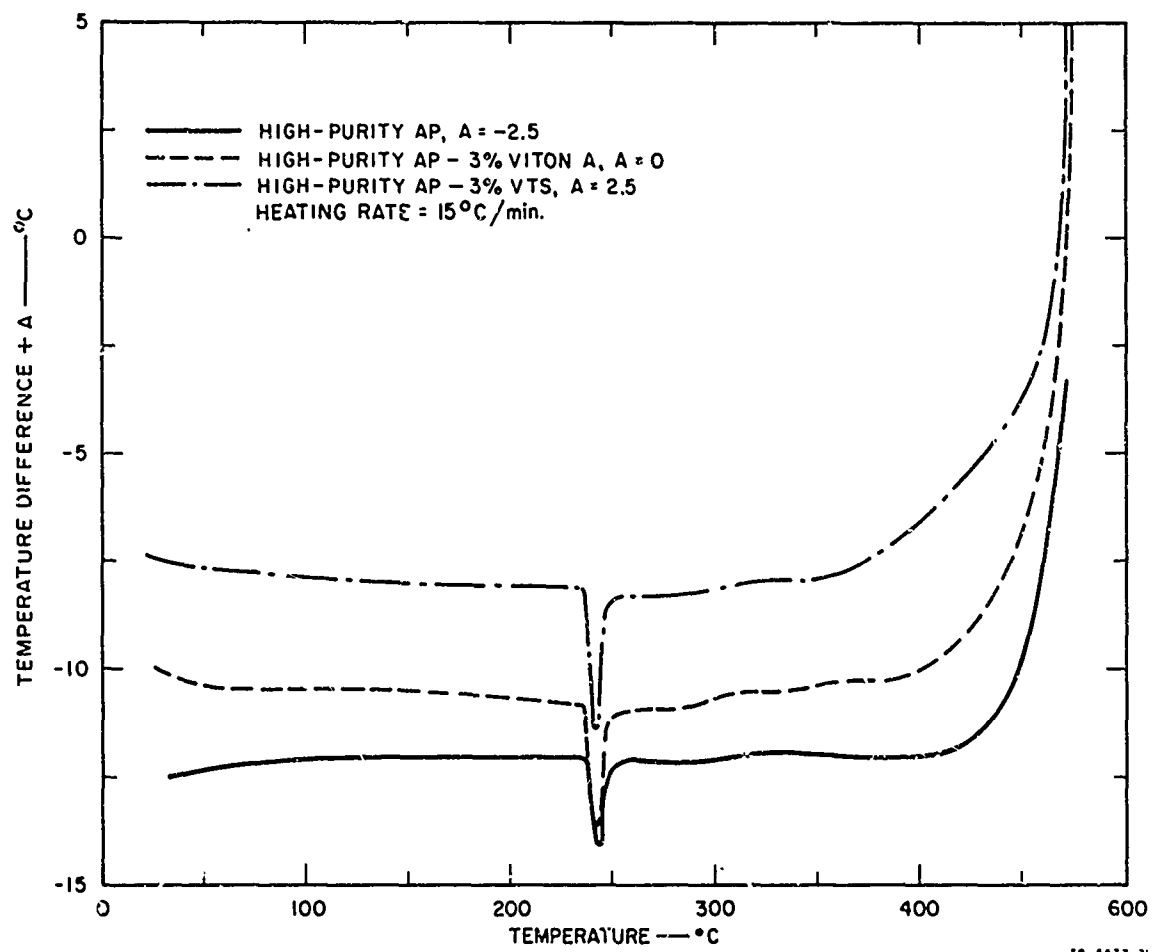


FIG. 15 DTA THERMOGRAMS FOR COATED HI-PURITY AP

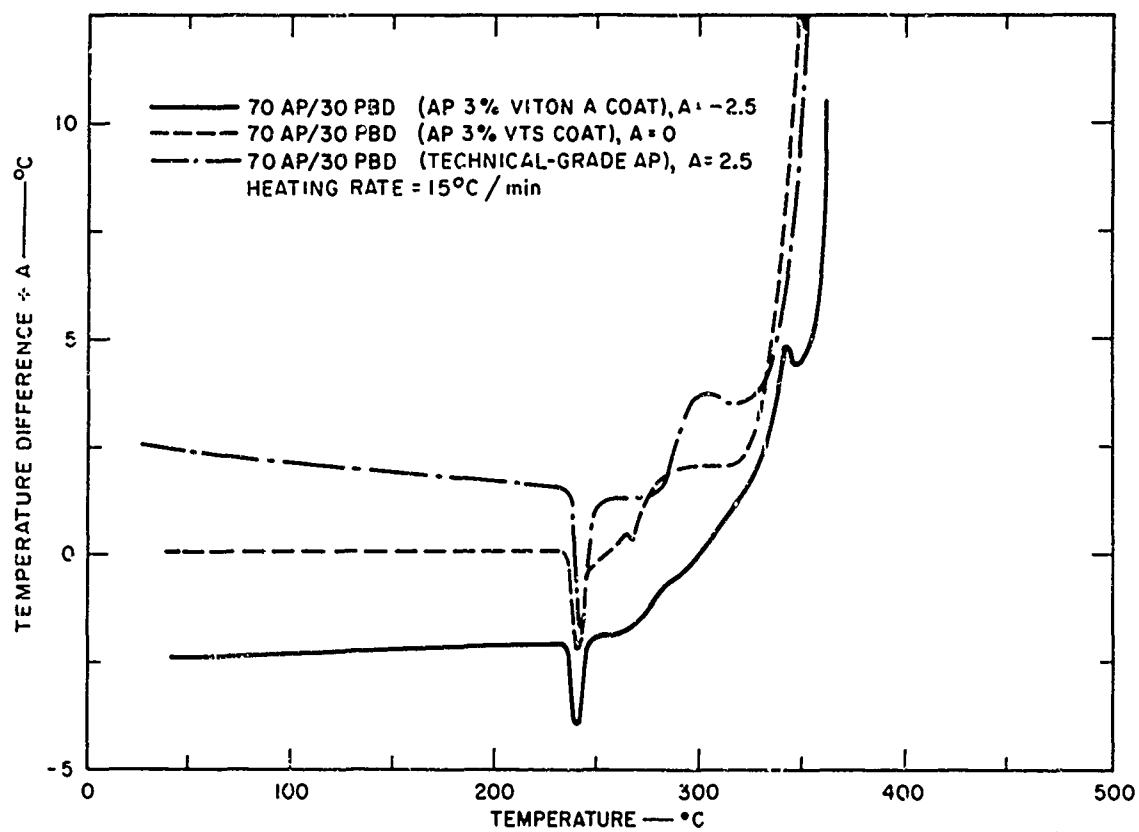
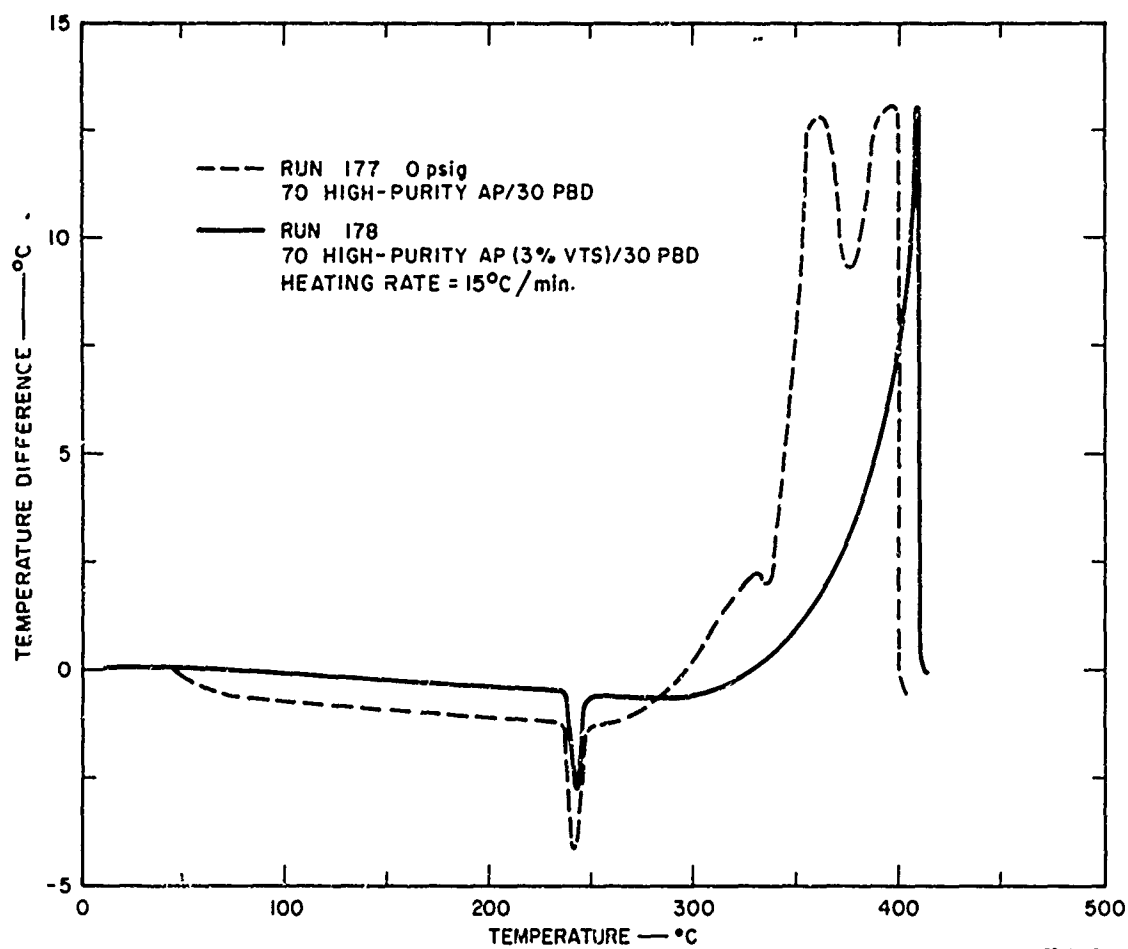


FIG. 16 DTA THERMOGRAMS FOR PROPELLANTS CONTAINING COATED TECHNICAL-GRADE AP



12-5577-22

FIG. 17 DTA THERMOGRAMS FOR PROPELLANTS CONTAINING COATED HIGH-PURITY AP



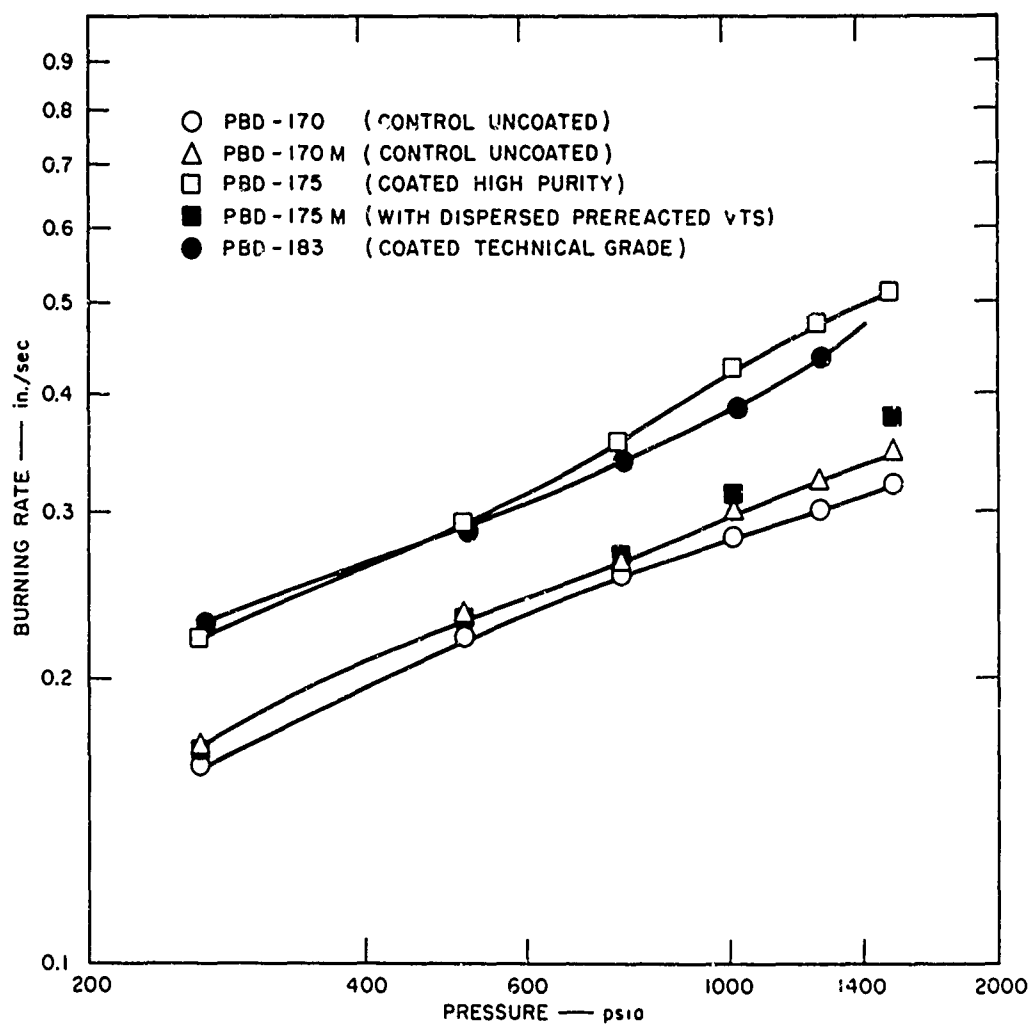


FIG. 18 BURNING RATE FOR PROPELLANTS CONTAINING COATED AND NONCOATED OXIDIZERS

Table III  
PROPELLANT COMPOSITIONS FOR COATED OXIDIZER STUDY

Formulation	Oxidizer <sup>(a)</sup>	Binder	Ballistic Modifier
PBD 170	80 HPAP <sup>(b)</sup>	20	2.5 vinylsiloxane <sup>(c)</sup> (not coated)
PBD 170M	80 AP	20	
PBD 175	80 HPAP	17.5	
PBD 175M	80 HPAP	17.5	
PBD 183	80 AP	17.5	

(a) 70% as received, 30% 11 $\mu$  ground.

(b) HPAP = high-purity ammonium perchlorate.

(c) Solution coated on all AP.

binder prepared from a PBD polymer (PBD R-45, Sinclair Petrochemicals) and toluene diisocyanate. (The choice of highly purified ingredients is critical for the clean separation of the observed exotherms.)

This special propellant was studied in the DTA cell at pressures up to 70 atm (1000 psia), and the data obtained are shown in Fig. 19. At pressures up to 25 atm (350 psia), two or more exotherm peaks occur; the first, from 350°C to 360°C, is unaffected by pressure change, but as the pressure is increased above 25 atm, the exotherms appear at successively lower temperatures until at 34 atm (500 psia), only one deflagration exotherm is recorded.

To gain additional information that would help explain observed phenomena, the DTA sample capillary was swept with a carrier gas (nitrogen) which was sampled continuously through the quadrupole residual gas analyzer. This instrument uses a quadrupole and rf electric field for mass analysis, and provides a rapid response of about 10 msec when scanning the mass range from 0 to 50. All tests were done at atmospheric pressure in order to obtain maximum separation of the exotherms. Any gaseous decomposition products were continuously monitored as the sample temperature increased. The gas transit time through the hot sampling

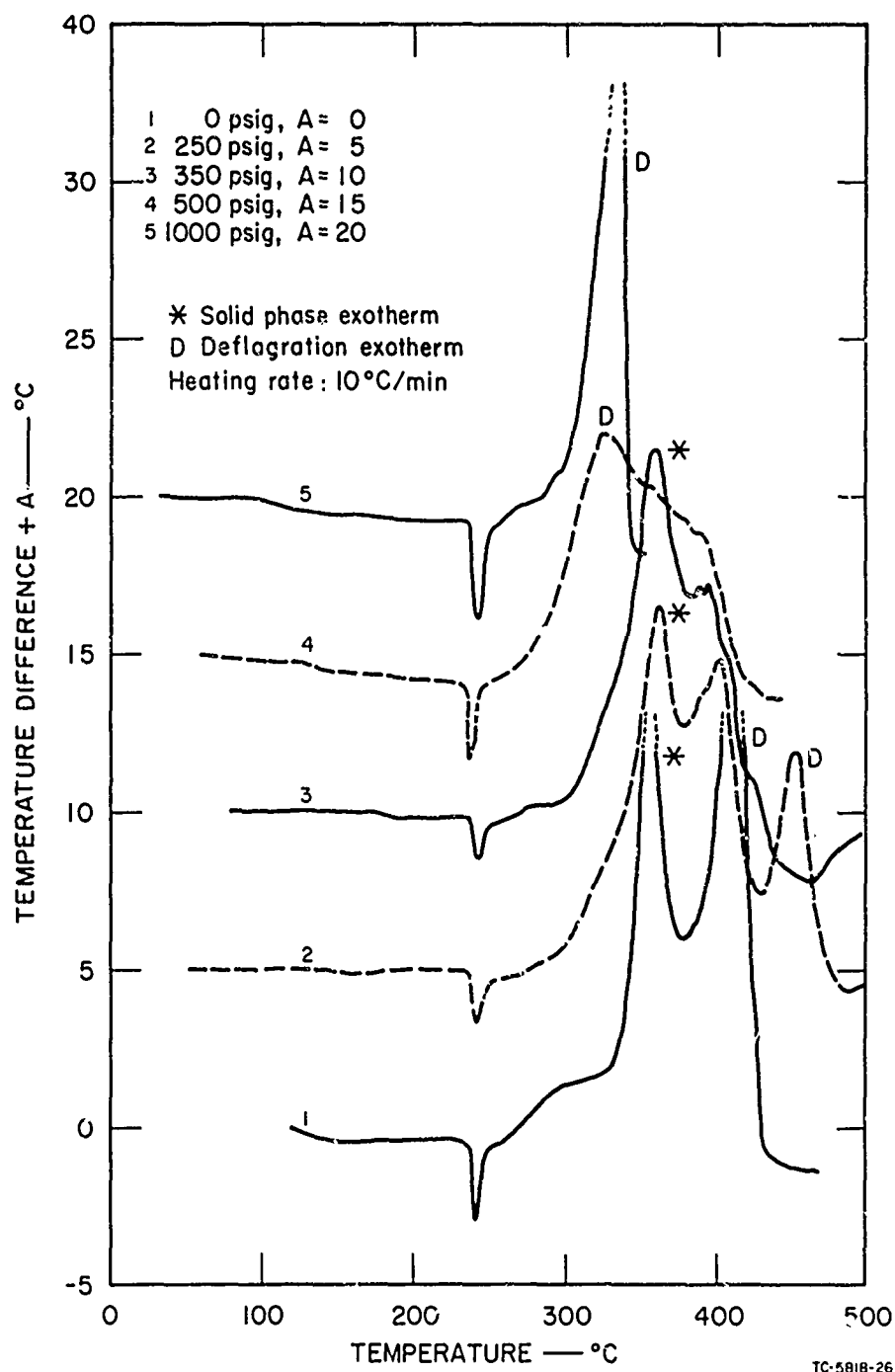


FIG. 19 THERMOGRAMS FOR PURIFIED PROPELLANTS AT AMBIENT AND ELEVATED PRESSURES

capillary was approximately 1 sec, whereas the duration of a typical exotherm was on the order of 4 min; thus for all practical purposes, sample analysis was instantaneous. Gas sampling data for the production-grade AP (which did not contain an anticaking agent) are given in Table IV. Little gas evolution occurred until the deflagration exotherm commenced above 400°C. A very slight amount of oxygen (less than 10<sup>-6</sup> moles/100-g sample) came off during the pre-decomposition exotherm. It can be concluded therefore that this is primarily a solid-phase exotherm resulting from decomposition or reaction of trace contaminants; sodium chlorate is a likely candidate:



Other unidentified organic contaminants introduced during preparation of ammonium perchlorate may also contribute to this pre-deflagration exotherm.

Table IV

MASS SPECTROGRAPHIC  
GAS ANALYSIS OF PRODUCTION GRADE

Species Detected		Mass to Charge Ratio m/e
at 310°C	at 460°C	
Trace O <sub>2</sub>	H <sub>2</sub> O <sup>+</sup>	18
	N <sub>2</sub> <sup>+</sup>	28
	NO <sup>+</sup>	30
	O <sub>2</sub> <sup>+</sup>	32
	HCl <sup>+</sup>	36
	N <sub>2</sub> O <sup>+</sup>	44

Relating the data on the first exotherm to the observed trends in behavior shown for the propellant in Fig. 18, it is surmised that, over the interval of 15 to 350 psia, pressure sensitivity causes the trailing exotherms to move to lower temperatures until at 500 psia, the gas-phase reactions predominate.

By using the known endotherm of 2.3 kcal/mole for the AP crystal change<sup>19</sup> (identified as the DTA endotherm at 240°C), it is feasible to estimate the percentage of total heat release contributed by the solid-phase exotherm. Since neither the endotherm nor exotherm is associated with the generation of any gases (which would result in mass changes and heat transport), it is considered permissible to relate the areas beneath the endotherm and exotherm of the DTA thermogram to the amounts of heat released or absorbed.<sup>20</sup> Thus, the thermogram at atmospheric pressure indicates that the condensed-phase reaction heat release for the propellant studied is 0.172 kcal/g. This is approximately 18% of the total heat release during explosion, 0.94 kcal/g, as measured in a calorimeter.

The experimental results for the special KP propellant are shown in Fig. 20, and the related gas analysis data are given in Table V. The data for the first exotherm at between 360°C and 368°C established that hardly any gas evolved, other than trace amounts of water and carbon dioxide. Thus, the first exotherm is apparently a condensed-phase reaction little affected by pressure. Significant gas evolution is associated with the other exotherms.

It is of significance that DTA thermograms for both pure KP and KP-based propellants showed only a deflagration exotherm. Even a liberal estimate of the heat release associated with solid-phase reactions in the propellant would not be above 5% of the total heat of explosion.

These observations are supported by previous work<sup>21,22</sup> with embedded surface thermocouples which showed that surface exotherms would be detected in AP propellants prior to ignition at incident fluxes above a critical flux. The compositions of the propellants used in this study are given in Table VI.

The surface layer thermocouple data for the KP-based propellant are shown in Fig. 21; those for the AP-based propellant are shown in Fig. 22. Figure 21 shows that after the initiation of the energy pulse at time  $i$  the temperature rises progressively until the pulse terminates at time  $t$ . At this time the surface layer loses heat principally by

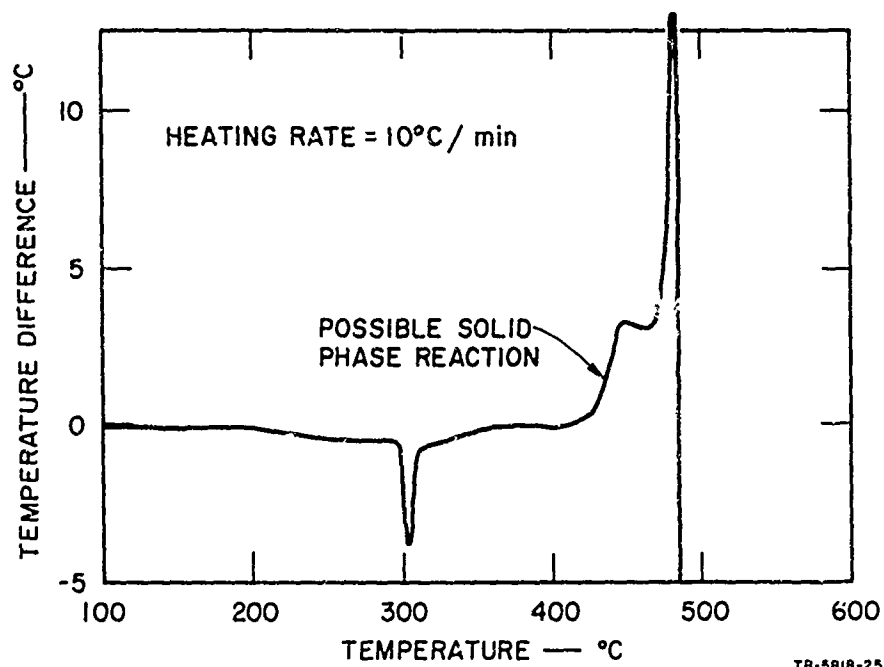


FIG. 20 THERMOGRAM FOR KP-BASED PROPELLANT

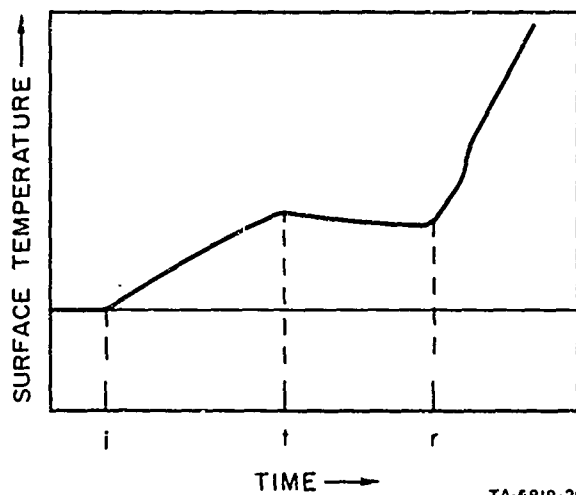
Table V  
MASS SPECTROGRAPHIC GAS ANALYSIS OF  
70/30 HIGH-PURITY AP/PBD PROPELLANT

Species Detected		Mass to Charge Ratio m/e
at 360°C	at 410°C	
Trace H <sub>2</sub> O <sup>+</sup>	H <sub>2</sub> <sup>+</sup>	2
	C <sup>+</sup>	12
	NH <sup>+</sup> , CH <sub>3</sub> <sup>+</sup>	15
	H <sub>2</sub> O <sup>+</sup>	18
	C <sub>2</sub>	24
	CN <sup>+</sup>	26
	HCN <sup>+</sup>	27
	NO <sup>+</sup> , CH <sub>2</sub> O <sup>+</sup>	30
	O <sub>2</sub> <sup>+</sup>	32
	HCL <sup>+</sup> , C <sub>3</sub> <sup>+</sup>	36
Trace CO <sub>2</sub> <sup>+</sup>	CO <sub>2</sub> <sup>+</sup>	44

Table VI

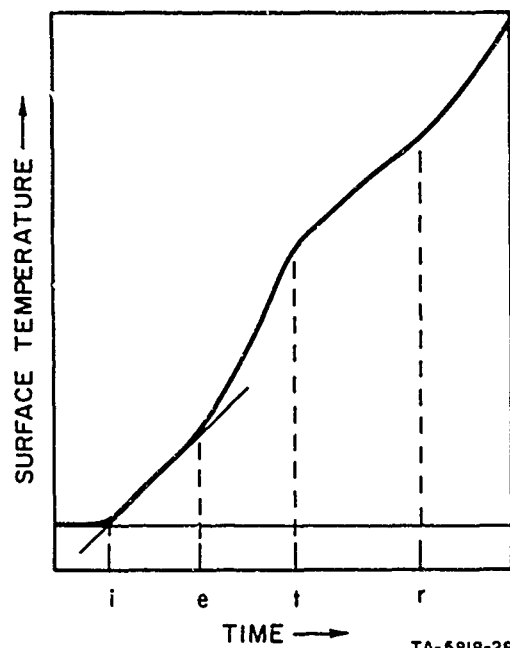
PROPELLANT COMPOSITIONS FOR THERMOCOUPLE STUDIES

Ingredient	PBAN 264	PU 128
AP (150 $\mu$ )	59.5	-
AP (11 $\mu$ )	25.5	-
KP (150 $\mu$ )	-	56.0
KP (11 $\mu$ )	-	22.0
PBAN Binder	15.0	-
PU Binder	-	22.0



TA-5818-20

FIG. 21 EMBEDDED SURFACE THERMOCOUPLE RESPONSE DURING IGNITION OF PU 128



TA-5818-28

FIG. 22 EMBEDDED SURFACE THERMOCOUPLE  
RESPONSE DURING IGNITION OF PBAN 264

conduction into the body of the sample, but ultimately a runaway deflagration occurs at time  $r$ . The temperature-time trace shows that heating of the sample occurs only by the external stimulus of the incident radiant energy.

A completely different response occurs in the case of the AP propellant as is shown in Fig. 22. Following initiation of the energy pulse (time  $i$ ) the temperature rises steadily, and at time  $e$  an inflexion occurs which can only be interpreted as the onset of condensed-phase exothermic reactions. On termination of the energy pulse (time  $t$ ) the temperature continues to rise because of the exothermic reaction, and a runaway deflagration (ignition) occurs at time  $r$ .

The difference in behavior of the KP- and AP- based propellants during an ignition event clearly reinforces the previous DTA indication that significant condensed-phase reactions only occur in the AP-based propellants.



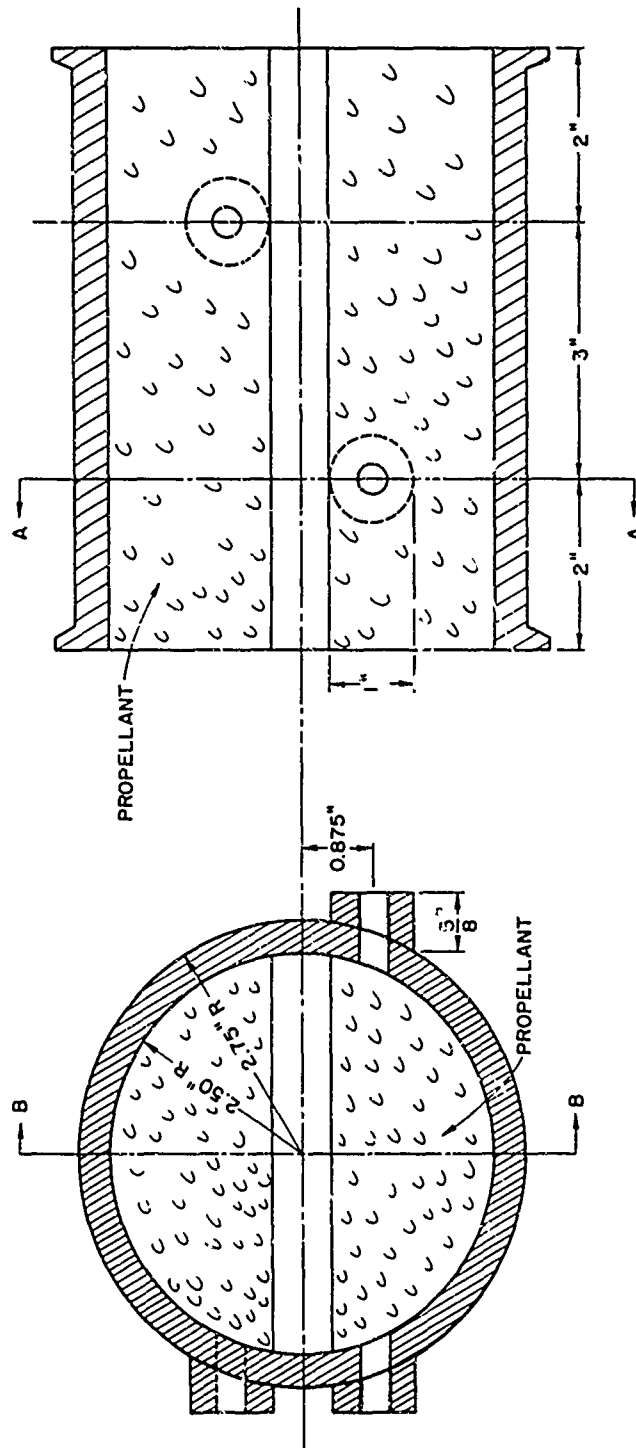
### Fiber-Optic Studies of the Solid Propellant Combustion Zone

The use of fiber optics in conjunction with high-speed photography provides a tool for the study of the microstructure in the combustion zone just above the burning propellant surface. The test motor used in this study is shown in Fig. 23. The upper half of the motor contains a single viewing port which is used when self-illumination from the flame zone is being photographed. The lower half of the motor contains two opposed viewing ports which are used when backlighting is required; e.g., for schlieren or shadow photography. Pyrex fiber optics which are 1/8 in. in diameter are screwed into the viewing ports; a high-speed camera is used to view the burning surface as it recedes past the fiber optic.

The transient extinction analysis predicts that surface-coupled reactions (i.e., heat release at or near the surface) have a profound effect upon the transient behavior. The existence of important heat release phenomena in the vicinity of the surface is clearly shown experimentally by the series of photographs included in the following pages.

The initial photographs without backlighting have revealed that the combustion zone is frequently disturbed by the explosive deflagration of single AP crystals. This phenomenon is observed clearly when camera framing rates on the order of 1000 fps are used. At a combustion pressure of 200 psig during the burning of an 80/20 AP/PU propellant, the deflagration of single crystals appears in less than 1/2% of the AP present. This estimation of frequency was made on the basis of a particle count of the deflagration and the estimated depth of field of the optical setup. Two photographs of these deflagrating crystals are reproduced in Fig. 24.

Figure 25 is a shadowgraph of a propellant containing 80% ammonium perchlorate and 20% PU. The chamber pressure for this test was 185 psia, and the backlighting was provided by a mercury arc lamp. The sequence of pictures shown is taken from a movie film shot at 8500 fps; the first four frames represent events 0.235 msec apart in time and the last frame



TC-3818-30

SECTION B

SECTION A

FIG. 23 TEST MOTOR USED TO OBTAIN FIBER-OPTIC PHOTOGRAPHS



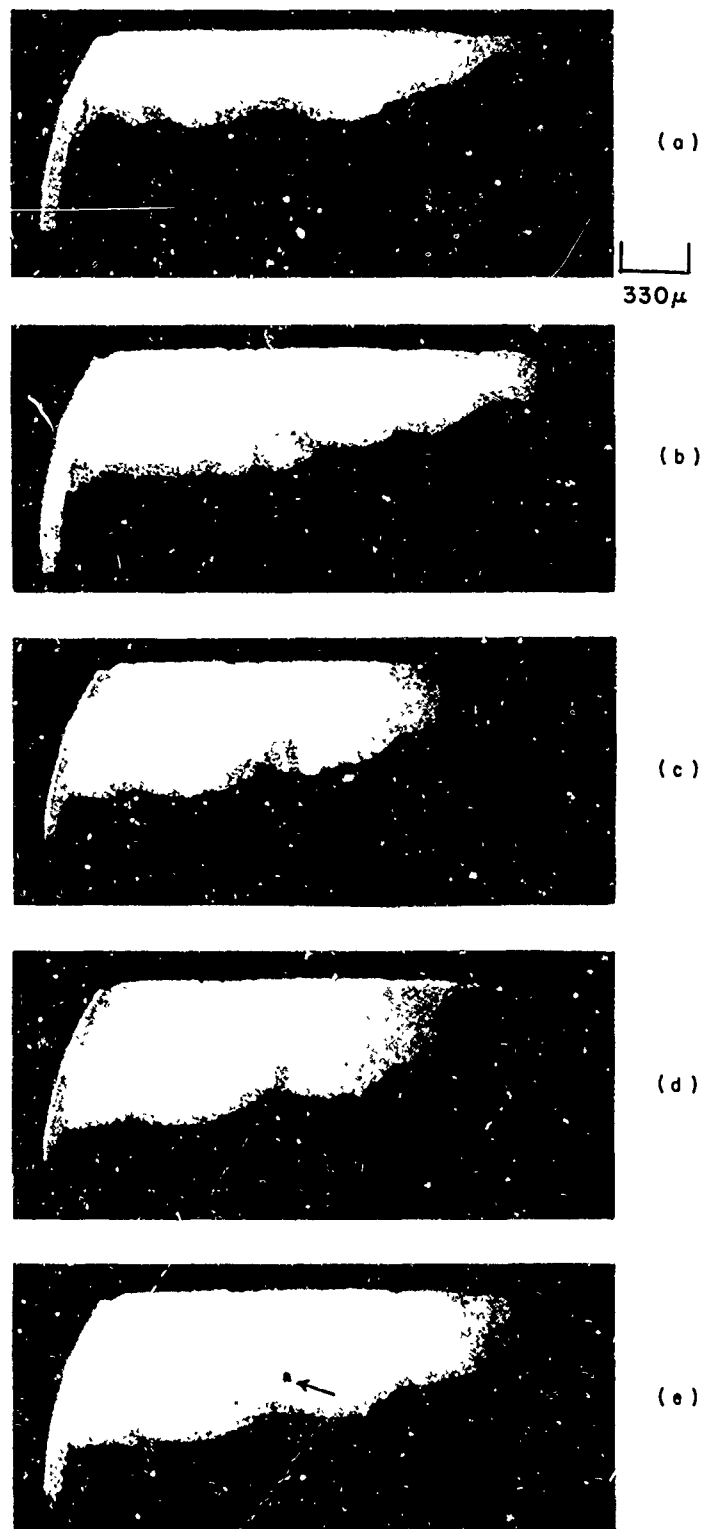
(a)



(b)

TA-5818-35

FIG. 24 DEFLAGRATION OF SINGLE AP CRYSTALS (200 psig)



TA-5818-47

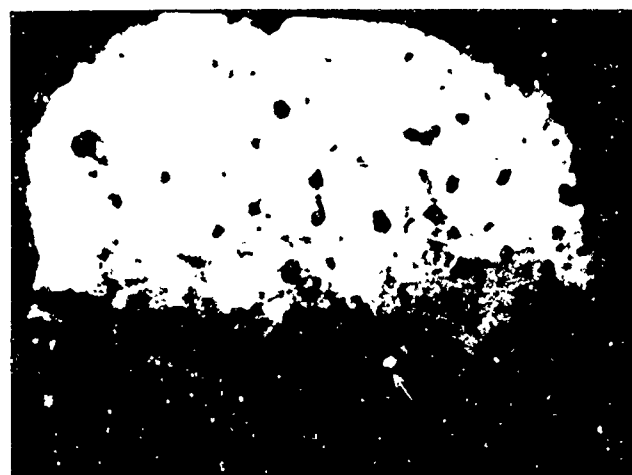
FIG. 25 FIBER-OPTIC SHADOWGRAPH SHOWING THE DEFLAGRATION OF AP AT THE SURFACE OF A BURNING SOLID PROPELLANT

follows the fourth by 0.118 msec. Frame (a) shows the emergence of an AP crystal above the burning surface. In frame (b), ignition is clearly seen to occur on two faces of the crystal; combustion then continues until ultimately, in frame (e), a final burning bit is seen to leave the surface. This particular crystal is somewhat atypical, as its diameter is about 400  $\mu$ , but smaller crystals which are more difficult to observe should behave in a similar manner.

Figures 26 and 27 show the ignition and subsequent partial combustion of aluminum particles at the burning surface. This particular propellant contained 5% aluminum by mass. The framing rate was 8500/sec, giving 0.118 msec between frames; these pictures were obtained without back-lighting. Frame (a) of both figures shows a glowing aluminum particle, about 50  $\mu$  in diameter, in place on the propellant surface. Ignition occurs in frame (b), and in frame (c), the burning particle is seen to leave the surface.

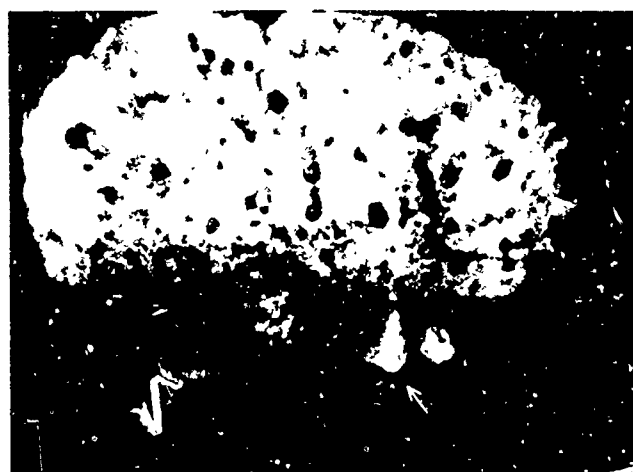
The sequences in these last two figures are representative of many that are observed during a typical test. The fact that aluminum ignition occurs at the surface is very interesting, because the temperature of approximately 1000°K in this region is far below the 2300°K ignition point of aluminum in oxygen. Thus, ignition must be induced by intermediate products of the perchlorate decomposition process.

For the pictures in this series, the burning aluminum provided its own illumination. The particle diameter was estimated from both its image size at the propellant surface upon ignition and from particles that condensed upon the fiber optic at or before their ignition. At 515 psia chamber pressure, most particles were observed to ignite at the surface of the propellant. The projected images of the particle traces were measured as indicated in Fig. 28. After ignition, a jet was formed above the surface, composed of the aluminum combustion products. After combustion has proceeded for a long enough time to reduce the mass of the particle to the point where its weight is equal to the aerodynamic drag force exerted on it, the burning particle is observed to fly off the surface. In several instances, large droplets of aluminum

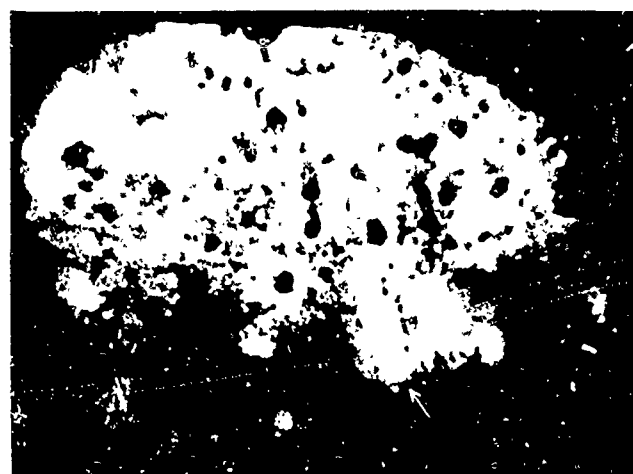


(a)

330 $\mu$



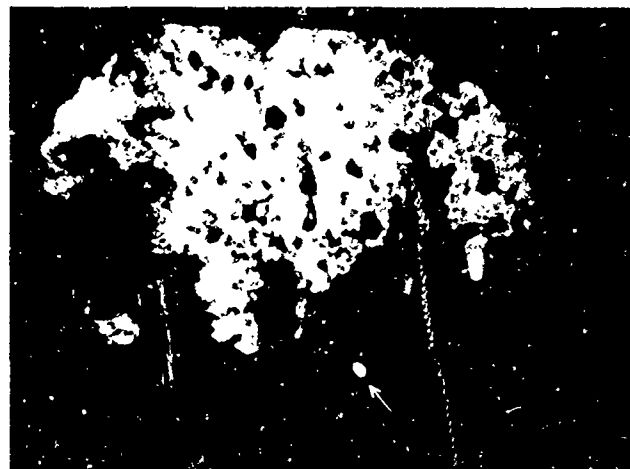
(b)



(c)

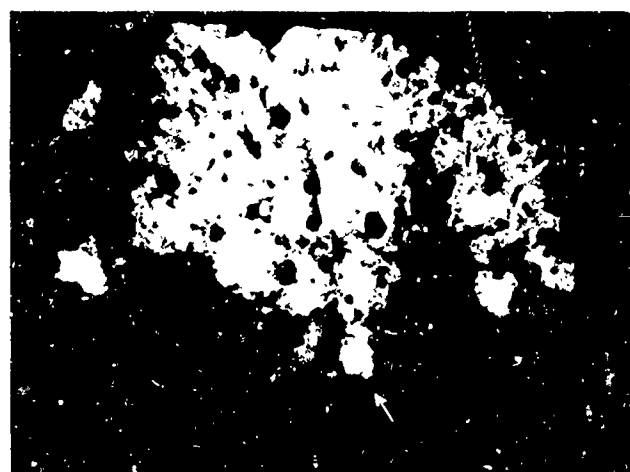
TA-5818-46

FIG. 26 FIBER-OPTIC VIEW OF THE IGNITION OF ALUMINUM PARTICLES  
AT THE SURFACE OF A BURNING SOLID PROPELLANT

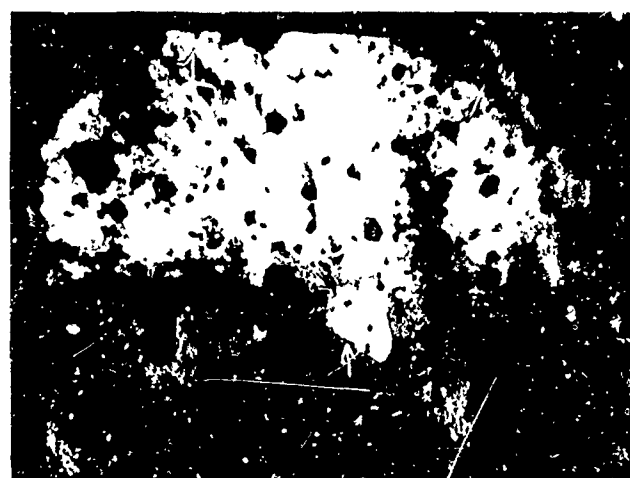


(a)

330 $\mu$



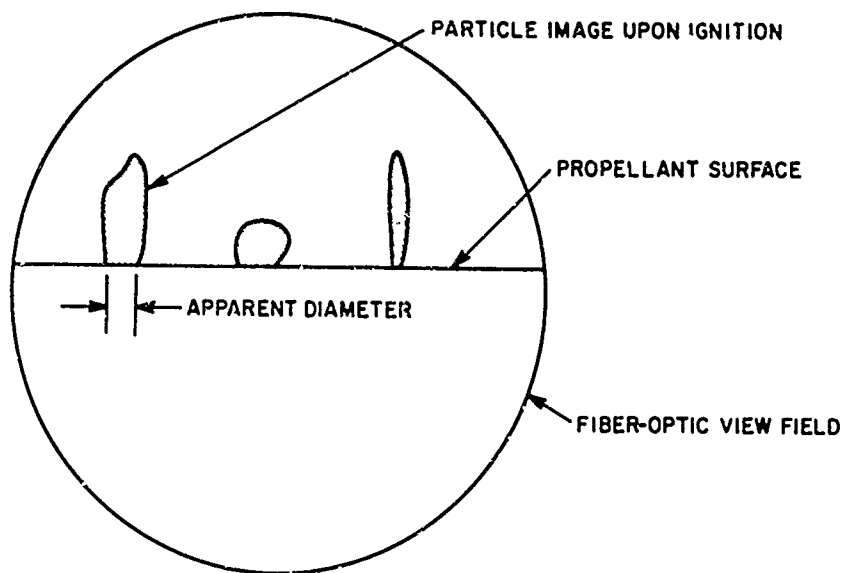
(b)



(c)

TP-5818 45

FIG. 27 FIBER-OPTIC VIEW OF THE IGNITION OF ALUMINUM PARTICLES  
AT THE SURFACE OF A BURNING SOLID PROPELLANT



TA-5577-59

FIG. 28 MEASUREMENT OF ALUMINUM PARTICLE DIAMETER AT IGNITION

in the size range of 40 to 60  $\mu$  were observed to glow red hot just before igniting.

The picture sequences provided us with a means of estimating the ratio of observed particle diameters before and after ignition. The measured luminous diameters were corrected by this ratio. The resulting particle size distributions are plotted in Fig. 29 as histograms. The data from both methods of analysis indicate that over 75% of the observed surface ignitions occur when the aluminum particle diameter lies in the range from 20 to 50  $\mu$ .

The size of the particles of aluminum added during processing was 6  $\mu$ ; the presence of the larger particles observed may be attributable to the aluminum agglomeration phenomenon reported by Crump<sup>23</sup> and other investigators. At the burning propellant surface, the temperature lies in the range of 850°K to 900°K where the small particulate aluminum has just reached its melting point (933°K). Under the influence of the buoyant gas jets from burning AP crystals, molten aluminum particles



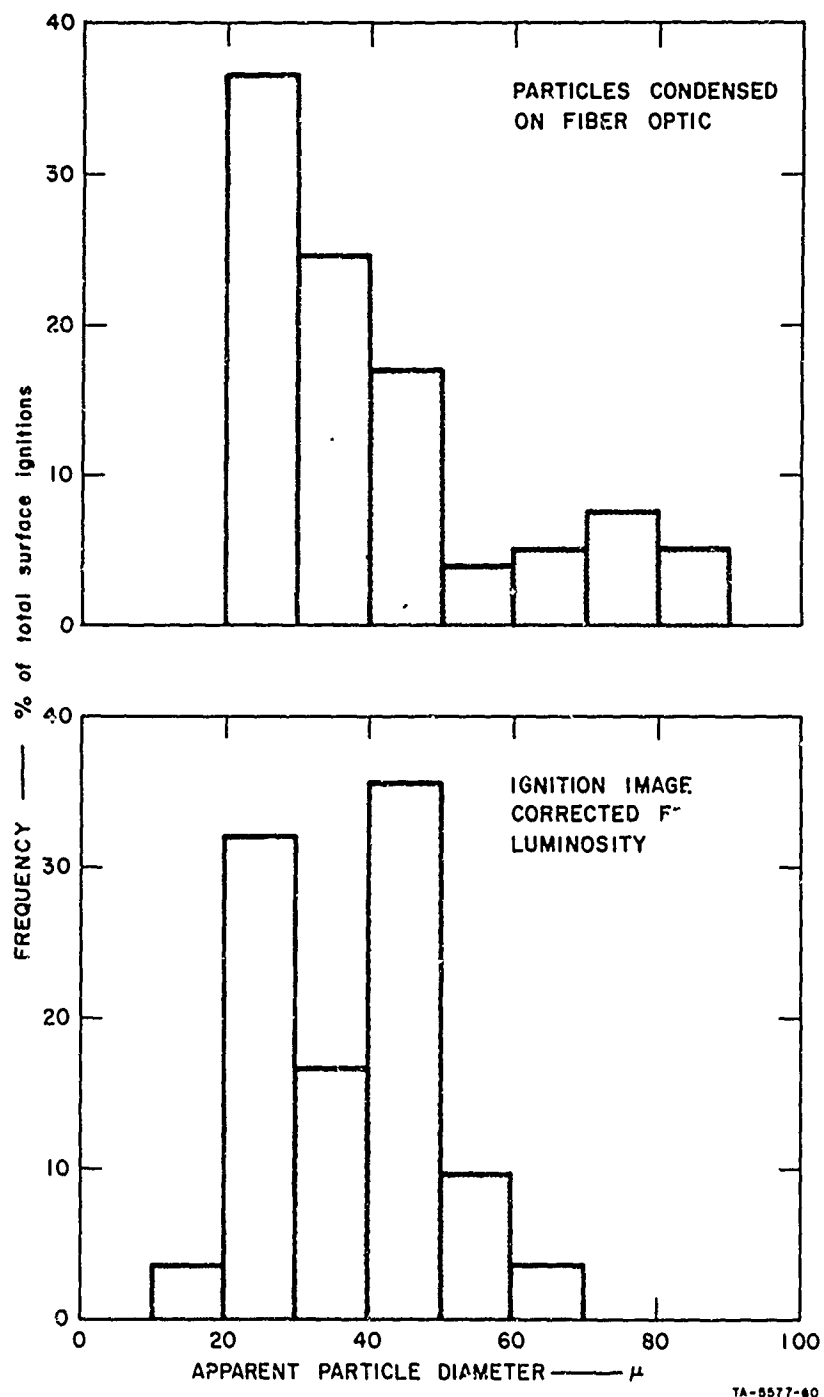


FIG. 29 APPARENT DIAMETER OF ALUMINUM PARTICLES AT IGNITION

move about in a random manner, with collisions causing agglomeration, until the preferred diameter of 20 to 50  $\mu$  is reached. In this size range, the aluminum agglomerate extends upward into a much higher temperature region of the combustion zone.

Experimental measurements<sup>24</sup> by flame pyrometry have indicated that in the surface region, the temperature rises from a surface value of about 850°K to the equilibrium flame temperature of 2200°K within about 100  $\mu$  of the surface. With this temperature profile, one would suspect that the preferred agglomerate particle diameter for ignition would be even larger than that measured experimentally, since ignition temperatures for aluminum in oxygen atmospheres have been reported to be above 2000°K. However, the actual gas composition at the propellant surface undoubtedly plays a major role in the ignition process.

Besides oxygen and the conventional combustion products from the burning hydrocarbon binder (CO, CO<sub>2</sub>, H<sub>2</sub>O), the combustion gases also contain AP decomposition products. These include Cl<sub>2</sub>, HCl, HClO<sub>4</sub>, NH<sub>3</sub>, and numerous other oxidizing species. It is reasonable to suspect that the ignition temperature of aluminum would be considerably lowered in such a gaseous atmosphere. More recent measurements of the flame thickness by Tourin,<sup>25</sup> Waesche,<sup>26</sup> and Povinelli<sup>27</sup> using more sophisticated techniques indicate that the flame thickness is nearer to 1000  $\mu$ . This makes it even more likely that ignition occurs through chemical attack by species other than oxygen, since the particles are in a region where the temperature is considerably less than 2000°K.

#### Traveling Wave Phenomena

Experimental studies to delineate the influence of propellant composition on instability have been based on the pulse triggering of longitudinal-mode finite-amplitude traveling waves.<sup>28</sup> In particular, the studies have sought to define the pressure-burning regimes in which unstable operation can occur.

Data have been reported previously for a wide variety of propellant formulations<sup>1,2</sup> that are summarized in Table VII. Firings of the various

Table VII  
EXPERIMENTAL PROPELLANT FORMULATIONS<sup>(a)</sup>

Formulation No.	NH <sub>4</sub> ClO <sub>4</sub>		KClO <sub>4</sub>		Other Additive (b)	Aluminum (c)	Binder (d)
	Ground	Unground	Ground	Unground			
102	24.0	44.2				15 Re 1131	PBAN, 16.8
103	24.0	56.0					PBAN, 20.0
104	22.5	56.0			1.5 LiF		PBAN, 20.0
105	22.5	44.2			1.5 LiF	15 Re 1131	PBAN, 16.8
106	23.0	44.2			1.0 Fe <sub>2</sub> O <sub>3</sub>	15 Re 1131	PBAN, 16.8
110	23.0	44.2			2.0 Fe <sub>2</sub> O <sub>3</sub>	15 Re 1131	PBAN, 15.8
111	22.0	56.0			2.0 Fe <sub>2</sub> O <sub>3</sub>		PBAN, 20.0
159	12.0	28.0	12	28			PBAN, 20
161	17.05 at 20 μ	34.1				15 Re 1131	PBAN, 16.8
162	17.05 at 600 μ						
166	24.0	44.2				15 VM H322	PBAN, 16.8
170	23.5	60.0	20.0				PBAN, 20
172	70.0	44.2			0.5 Fe <sub>2</sub> O <sub>3</sub>	15 VM H322	PBAN, 16.8
		60.0	10.0				PBAN, 20
184	17.05 at 20 μ						
		34.1				15 VM H322	PBAN, 16.8
185	17.05 at 600 μ						
	20	20 at 600 μ		40			PBAN, 20
186	20.0 at 20 μ	40					PBAN, 20
189M	20.0 at 600 μ						
108	60			20			PBAN, 20
109	22.5	52.5	24.0	56.0			PU, 25
113					64.0 AN		PBAN, 20
244	23	56			1.0 Milori Blue		PU, 25
284	23.5	56.5			1.0 LiF		PBAN, 20
125			30		0.5 SrCO <sub>3</sub>		PBAN, 20
127	40				49.0 AN <sup>b</sup>		PU, 20
104-PS					40.0 AN <sup>b</sup>		PU, 20
					-3.4 LiPb		PS, 25.6

(a) Average particle diameter of 10 μ unless specified otherwise. Amounts in weight percent.

(b) AN = ammonium nitrate, LiP = lithium perchlorate

(c) Re = Reynolds, VM = Valley Metallurgical

(d) PS = polysulfide

propellants were carried out in 5-in.-diam motor hardware with motor lengths of 15, 23, 40, and 82 in. Pulses introduced into the 15-in. and 23-in. motor were found to decay; in the longer motors, however, a definite traveling wave instability could be established for AP propellants above a critical mean pressure for each propellant. In the 82-in. motor the onset of instability was almost always followed by transition to a double mode consisting of two traveling waves, one occupying the front half of the motor and one the rear half, that reflect from one another at the center.

The threshold instability data for the AP propellants in the 40-in. motor are given in Table VIII and plotted in Fig. 30. A definite threshold line is established separating stable and unstable operation; the same line was valid for the data obtained in the 82-in. motor, as shown in Fig. 31. The final results for all propellants considered are shown in Fig. 32. Note that the AN/AP and AN/KP propellants which were formulated to have the same ballistic behavior had completely different stability behavior. This experimental conclusion demonstrates that the instability phenomenon is closely tied to the presence of surface-coupled heat release. The unstable AP propellant must have had significantly greater surface-coupled heat release than the stable KP propellant; this is consistent with the DTA measurements reported earlier.

In addition to the cylindrical motor firings just discussed, data were also obtained in a slab configuration which allowed the location of pressure transducers along the side wall as well as at the head end. Typical experimental behavior is shown in Fig. 33 for PBAN 319 propellant in an 82-in. slab motor operating at a mean pressure of 1260 psia. The important point to be noted is that the head-end pressure pulse is approximately twice as large as the pulses measured at the one-quarter and three-quarter length stations. The aft-end pulse is somewhat smaller than the head-end pulse, presumably because this pressure is measured 4 in. upstream of the nozzle. A possible additional contributing factor may be energy loss upon reflection from the open nozzle.

Table VIII

## AXIAL INSTABILITY TEST DATA FOR AP-CONTAINING PROPELLANTS

Threshold Data						
	Pressure, $P_T$ (psia)	Burning Rate, $r$ in./sec <sup>r</sup>	$A_t$ , (in. <sup>2</sup> )	$D_p$ , (in.)	J	$K_N$
<u>Unstable</u> <u>Propellants:</u>						
PBAN 102	950	0.325	1.23	3.30	7.0	330
PBAN 103	700	0.30(a)	1.28	3.30	6.6	320
PBAN 104	360	0.17(a)	1.83	4.80	7.1	270
PBAN 105	900	0.315	1.37	3.80	8.8	340
PBAN 106	1600	0.56	1.47	3.78	8.7	350
PBAN 161	750	0.275	1.19	2.50	5.0	300
PBAN 162	760	0.29	1.84	2.51	4.9	290
PBAN 166	500	0.215(a)	1.33	3.70	6.9	265
PBAN 170	1350	0.50	1.59	4.01	8.1	310
PBAN 172	530	0.24	1.59	3.37	5.7	270
PBAN 184	700	0.260	1.24	3.14	6.5	300
PBAN 186	720	0.28(a)	1.22	3.47	8.1	340
PU 108	400	0.18	1.49	3.47	6.4	285
PBAN 244	400	0.19	....	....	...	...
PBAN 284	325	0.16	....	....	...	...
PU 127	Highly Unstable: 500-1000 psi					
<u>Stable Propellants:</u>						
PBAN 109	Stable (400-2500 psi)					
PBAN 110	Stable (400-2500 psi)					
PBAN 111	Stable (400-2500 psi)					
PBAN 159	Stable (400-2500 psi)					
PBAN 185	Stable (400-2500 psi)					
PBAN 189(a)	Stable Axially (400-2500 psi)					
PS 104	Stable Over Range (400-2500 psi)					
PU 113	Stable (700-1000 psi)					
PU 125	Stable					

(a) Transitioned to transverse mode

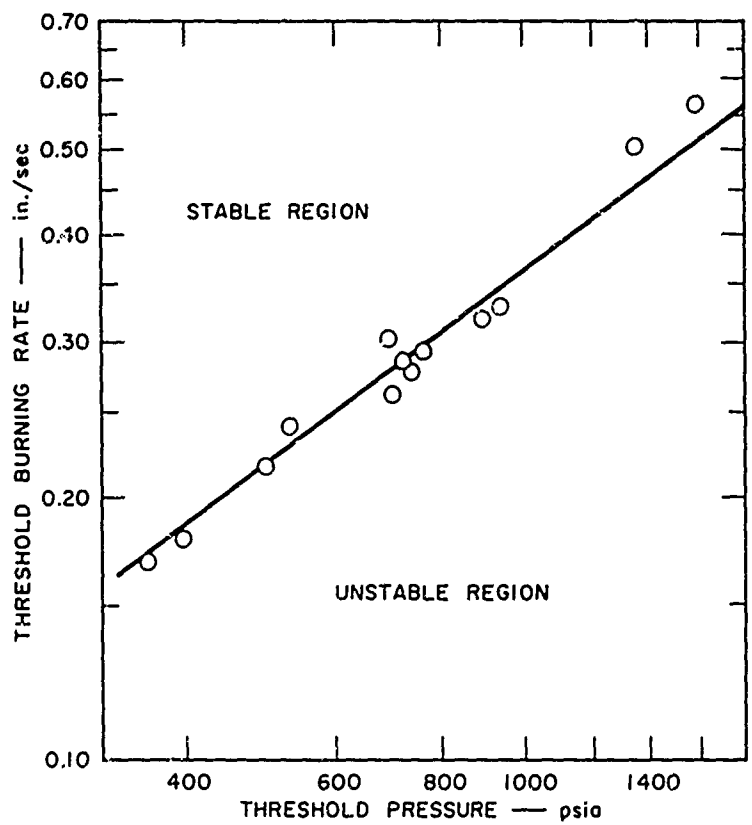


FIG. 30 CORRELATION OF THRESHOLD PRESSURE WITH PROPELLANT BURNING RATE IN A 5 x 40-INCH ROCKET MOTOR

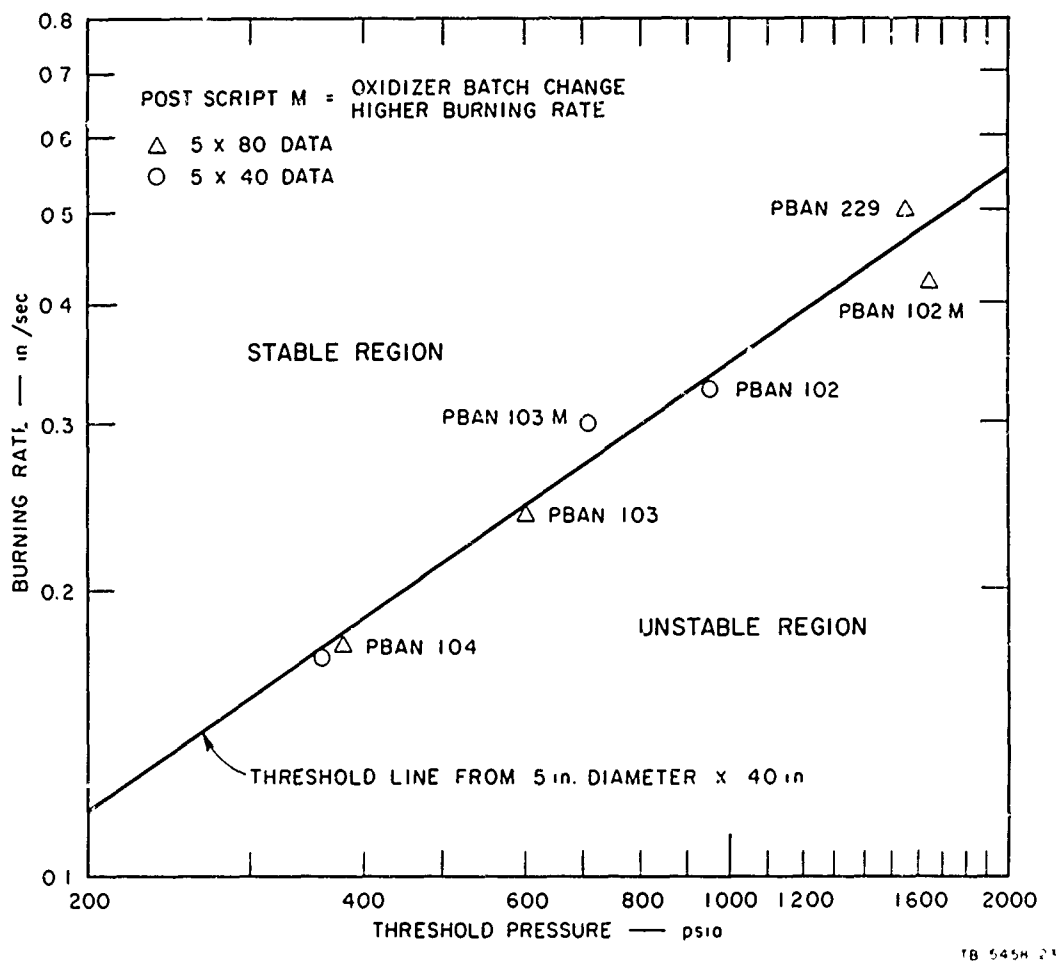


FIG. 31 COMPARISON OF STABILITY BEHAVIOR OF 5 x 40-INCH AND 5 x 80-INCH ROCKET MOTORS

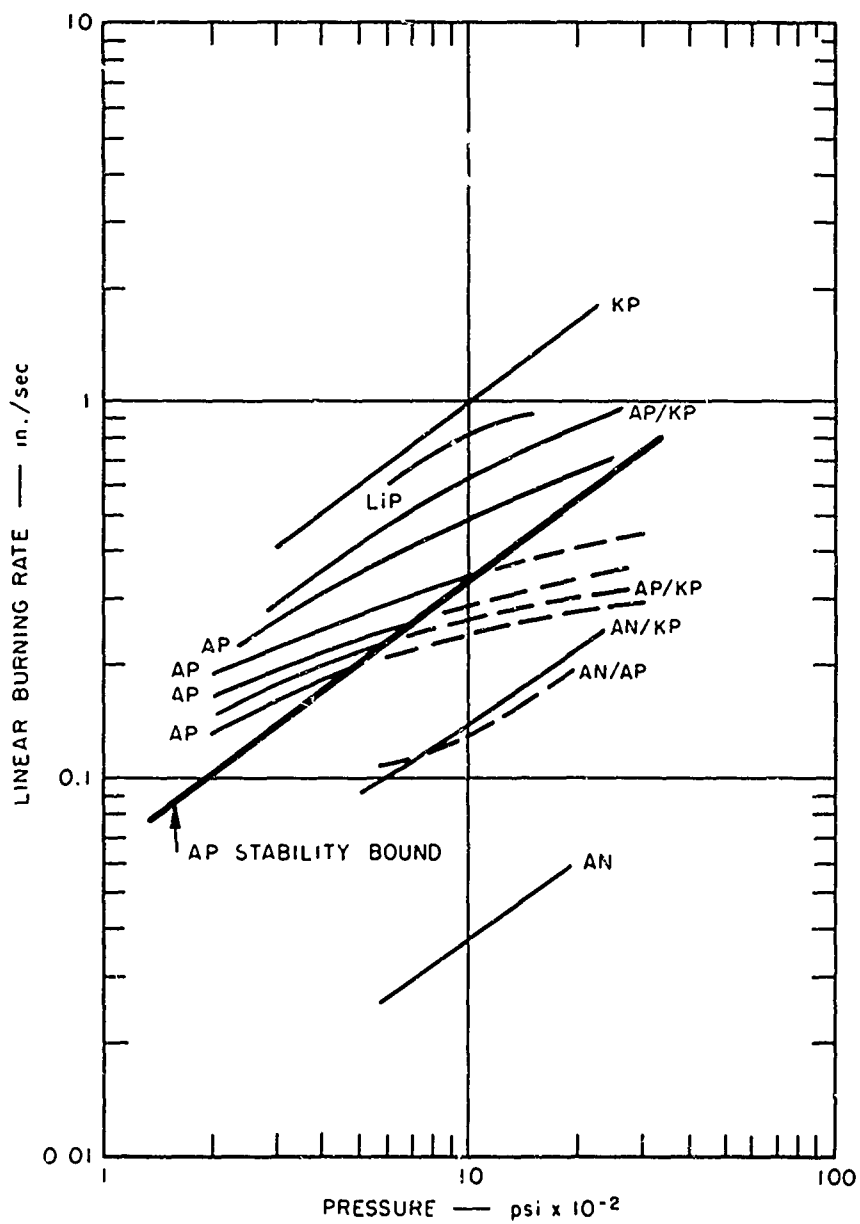
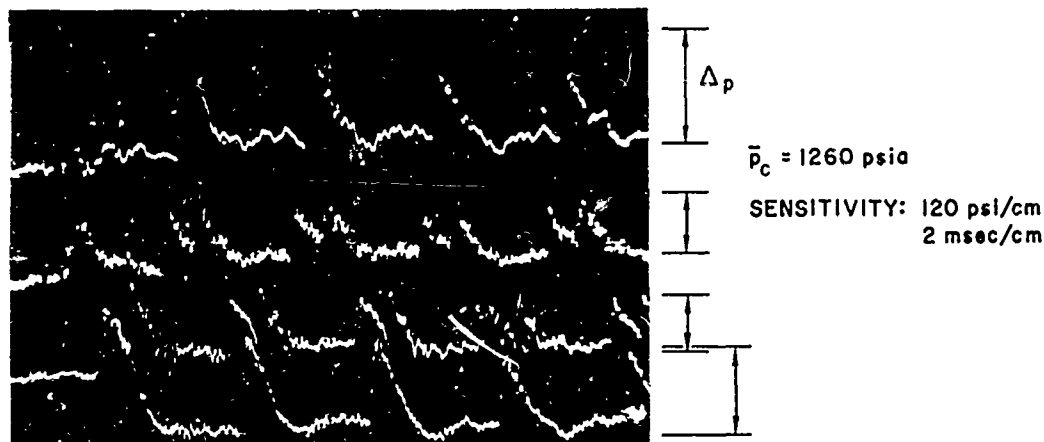


FIG. 32 INFLUENCE OF BURNING RATE AND COMPOSITION ON TRAVELING WAVE INSTABILITY IN A 5 x 40-INCH ROCKET MOTOR (Instability Denoted by Dashed Curves)





TA-5818-15

FIG. 33 TRAVELING WAVE INSTABILITY IN A SLAB BURNER

From a phenomenological point of view, the behavior illustrated by the pressure traces of Fig. 33 can be explained by the presence of a constant strength shock-expansion process which is traveling back and forth in the motor. The passage of the shock wave past any point induces a particle velocity behind it in the direction of travel of the shock, as well as pressure and temperature jumps. In order to satisfy the continuity equation, an expansion process which reduces the induced velocity to zero must form behind the shock wave, as discussed in the "Theoretical Studies" section of this report. Since the expansion process is isentropic, the local velocity of the expansion field will be the local speed of sound, which decreases with increasing distance behind the shock wave. Thus the extent of the expansion process will lengthen as wave travel proceeds down the chamber, but this effect will be slight because the shock wave is weak.

When the shock wave reflects from the end of the chamber, the measured perturbation amplitude doubles because the shock wave will maintain the same pressure change across itself, whereas the pressure in front of the reflected shock is the pressure which was behind the incident shock. A correspondingly strong expansion process will follow the reflected shock back down the passage toward the oncoming expansion

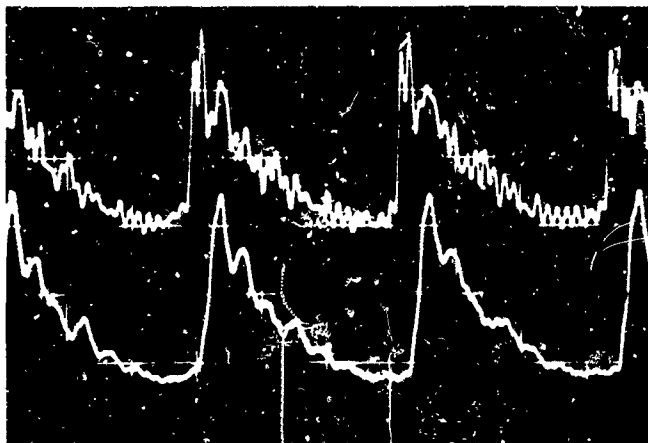
process which was following the incident shock. This incoming expansion process reduces the strength of both the reflected shock and its trailing expansion process down to the strengths of the original process and the chain of events is repeated in the opposite direction. This complicated turn-around process occurs in a very short physical distance, making the details very difficult to obtain experimentally.

This physical reasoning is borne out by further examination of Fig. 33. Not only does pressure doubling occur at the ends, but the wave velocity along the chamber is nearly constant, since a comparison of the data at the quarter-length point with that at the head-end shows that about one-quarter of the total wave travel time is used over the first quarter of the motor. A constant wave velocity implies a constant wave strength; within the accuracy of the traces, the strengths at the one-quarter and three-quarter points are the same.

The final strength (and therefore velocity) of the wave will be determined by the balance between the energy input process and the dissipation process at the walls and by the coupling between the passage of the wave and the primary combustion process. A possible mechanism for this coupling has been discussed in "Theoretical Studies" (see also Appendix C).

Using the fact that pressure doubling occurs upon shock reflection at the end of the motor, head-end pressure measurements can be used to compute the propellant response to the passage of steep-fronted waves. Head-end pressure measurements obtained in tubular motors with five different propellants are shown in Fig. 34. The propellant compositions are listed in Table IX. Two traces are shown for each propellant, the lower one of which has been filtered to remove the organ pipe oscillation in the small cylindrical chamber ahead of the transducer.

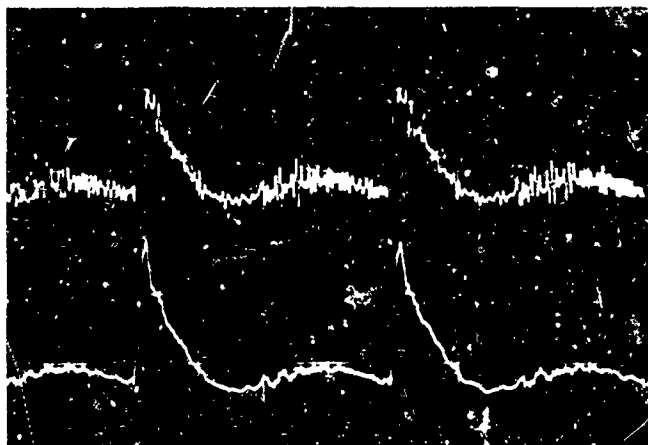
The wave amplitude (see Table IX), computed as half of the head-end pressure pulse for reasons discussed above, is relatively constant for all the propellants considered, being about  $\Delta p/\bar{p} = 0.17$ . The variations which do occur undoubtedly depend more upon the ratio of the mean pressure to the threshold pressure for instability than upon compositional factors in these similar AP-based propellants.



PBAN 103

$\bar{p}_c = 915$  psia

SENSITIVITY: 120 psi/cm  
0.5 msec/cm



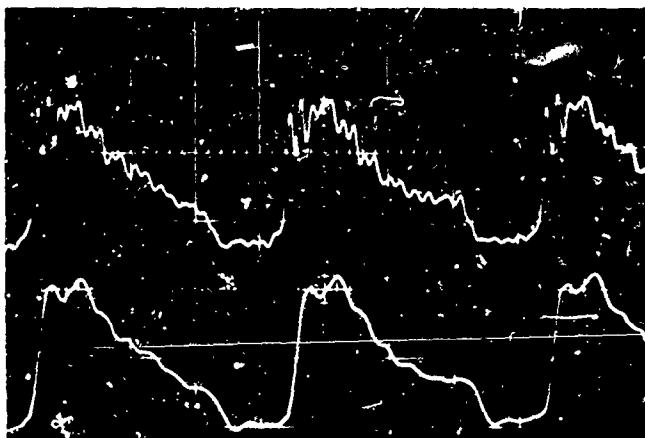
PBAN 104

$\bar{p}_c = 565$  psia

SENSITIVITY: 80 psi/cm  
1 msec/cm

TA-5618-16

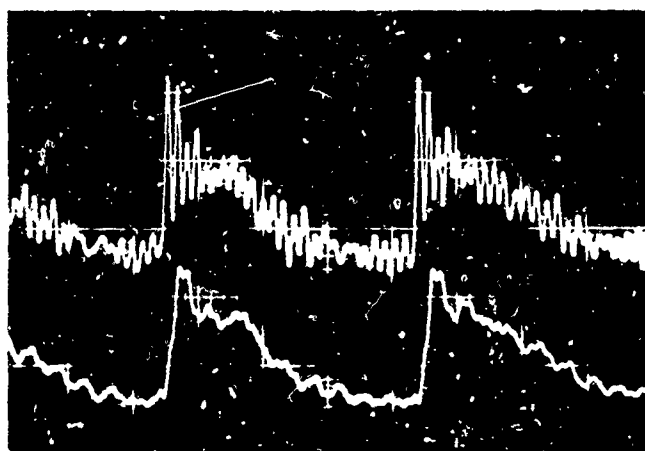
FIG. 34 HEAD-END PRESSURE TRANSIENTS DURING TRAVELING WAVE  
INSTABILITY IN A TUBULAR BURNER



PBAN 244

$\bar{p}_c = 410$  psia

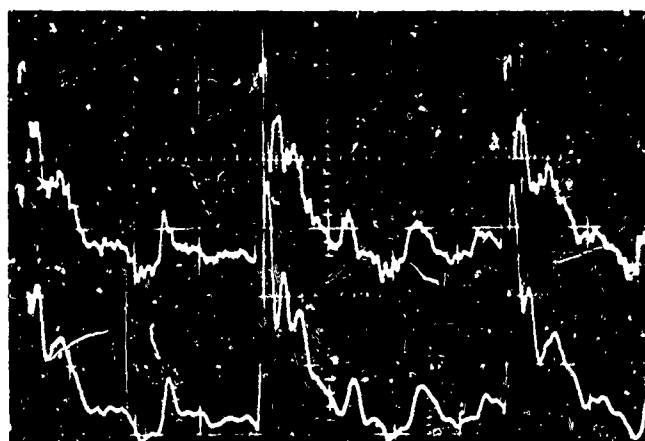
SENSITIVITY: 60 psi/cm  
0.5 msec/cm



PBAN 284

$\bar{p}_c = 635$  psia

SENSITIVITY: 80 psi/cm  
0.5 msec/cm



PBAN 319

$\bar{p}_c = 1215$  psia

SENSITIVITY: 120 psi/cm  
1 msec/cm

TA-5816-17

FIG. 34 Concluded

TABLE IX  
TUBULAR MOTOR INSTABILITY DATA

Propellant	Composition	Motor Length (in.)	Wave Amplitude ( $\Delta p/\bar{p}$ )	Wave Frequency (cps)
PBAN 103	24% ground <sup>a</sup> 56% unground } $\text{NH}_4\text{ClO}_4$ 20% PBAN	40	0.185	600
PBAN 104	22.5% ground <sup>a</sup> 56% unground } $\text{NH}_4\text{ClO}_4$ 20% PBAN 1.5% LiF	82	0.169	244
PBAN 244	27% ground <sup>a</sup> 52% unground } $\text{NH}_4\text{ClO}_4$ 20% PBAN 1% LiF	40	0.163	500
PBAN 284	20% - 20 $\mu$ 20% - 600 $\mu$ } $\text{NH}_4\text{ClO}_4$ 39.5% unground 20% PBAN 0.5% $\text{SrCO}_3$	40	0.138	513
PBAN 319	22% - 20 $\mu$ 22% - 600 $\mu$ } $\text{NH}_4\text{ClO}_4$ 34% unground 17% PBAN 5% Al	82	0.184	250

<sup>a</sup> Average particle diameter of 10  $\mu$ .

In the 82-in. motor it was found experimentally that the shock wave traveled from end to end of the motor, with the frequencies shown in Table IX, only during the first 100 msec after the initiating pulse. In every case the motor failed to sustain such a mode beyond this initial period. Instead, a transition to a double mode (i.e., the first harmonic) always occurred. In this case there were two traveling shock waves in the motor, each traveling through a 41-in. section and reflecting from the other wave at the center. Thus, the 82-in. motor always undergoes a transition to an axial instability mode that exhibits the same frequency range as that shown for a 40-in. motor in Table IX.

#### IV. THEORETICAL INTERPRETATION OF EXPERIMENTAL RESULTS

The experiments reported in the preceding section have clearly indicated the importance of surface-coupled heat release phenomena, confirming the basic premises underlying the transient combustion theory developed elsewhere in the report. However, the ultimate measure of the theory is the effectiveness with which it explains experimental observations. The ensuing discussion will provide an interpretation of axial-mode combustion instability data in terms of frequency and response amplitude criteria derived from the theoretical treatment presented earlier.

##### The Frequency Criterion

As a shock wave travels back and forth in the combustion chamber, it creates an oscillatory pressure disturbance at every point on the propellant surface. The frequency of this disturbance at any given axial position corresponds to the number of times per second that the wave passes this position. In general, there are two distinct frequencies associated with any given axial position. One of these corresponds to the time required for a shock wave traveling toward the right to be reflected from the right end of the chamber and returned to the reference point. The other frequency corresponds to the time for a wave traveling toward the left end to be reflected and return to the same point. At the ends of the chamber only one of these frequencies pertains (i.e., the other is infinite); at the center they are equal, of course. From a brief consideration of this phenomenon one can readily see that the pulse frequency at the center of the chamber is exactly twice that at the ends. At intermediate stations the propellant is subjected to a train of pulse pairs. For example, at the one-quarter and three-quarter positions the separation between pairs corresponds to a recurrence frequency of two-thirds of that at the center, while the spacing between two pulses in a pair corresponds to a frequency of twice that at the center. The band of frequencies encountered is thus dependent on the

motor length, and the stability behavior is dependent on the net driving and damping of the wave train.

Pulse frequencies encountered in experiments performed during this program are shown in Table X. For the 23-, 40-, and 82-in. motors, frequencies were measured at the head-end pressure transducer. As mentioned earlier, these frequencies are produced by a traveling shock wave moving at  $M \approx 1.2$  back and forth in the chamber. Ordinarily, pulses introduced in the 15-in. motor were found to decay; i.e., with most propellants this motor could not be driven to unstable combustion. The frequencies shown in Table X for this motor are the calculated characteristic frequencies based on a traveling shock wave with  $M \approx 1.2$ .

Table X  
FREQUENCY OF PRESSURE PULSE (cps)

Length of Chamber (in.)	End	Axial Position		Center
		1/4 L	3/4 L	
15	1240	1660	4960	2480
23	803	1070	3212	1606
40	465	620	1860	930
82	238	318	952	476

In order to compare these values with theoretical response curves, it is necessary to assign approximate values to the thermochemical parameters that characterize the propellants. For most composite propellants it is reasonable to assume that the activation energy for surface decomposition is  $E_w \approx 30$  kcal. The surface temperature  $T_w$  is approximately  $800^\circ\text{K}$ , and the gas-phase flame temperature is  $T_f \approx 2500^\circ\text{K}$ . The activation energy for the gas-phase flame usually is  $E_f \approx 30$  kcal and the overall effective order of reaction  $n$  is about 1. The parameters for a very wide range of propellants, including those that have been investigated experimentally in this program, almost certainly fall close



to these values. If, additionally, approximately 10% of the heat release occurs near the surface, a typical composite propellant is characterized in Fig. 2 by the parameters  $A \sim 12$  and  $\alpha \sim 0.75$ . It follows that  $1/\sqrt{\tilde{m}/\tilde{p}} \sim 7$  for such propellants, and the resonant frequency of the combustion mechanism corresponds to  $K\omega/\bar{r}^2 \sim 10$ , or  $f \sim 10 \bar{r}^2/2\pi K$ . The maximum deviation from this frequency for which there is a significant burning rate amplification is estimated to be about:

$$\Delta f \approx \pm 3\bar{r}^2/2\pi K$$

A typical thermal diffusivity for solid propellants is  $K \approx 2.3 \times 10^{-4}$  in.<sup>2</sup>/sec. Accordingly, the approximate frequency range in which the combustion mechanism tends to amplify a pressure oscillation is as indicated in Table XI. The frequency given in the table is the approximate resonance frequency, or point of maximum amplitude, and the tolerance figures indicate the approximate range in which a degree of amplification is present.

Table XI

APPROXIMATE RESONANT-FREQUENCY RANGE FOR A  
TYPICAL COMPOSITE PROPELLANT ACCORDING TO THEORETICAL COMBUSTION MODEL

<u><math>\bar{r}</math> (in./sec)</u>	<u><math>f</math> (cps)</u>
0.1	$\sim 66 \pm 20$
0.2	$\sim 275 \pm 80$
0.3	$\sim 625 \pm 190$
0.4	$\sim 1100 \pm 330$
0.5	$\sim 1725 \pm 520$

It is reasonable to assume that axial-mode combustion instability may arise in a solid rocket chamber whenever an appreciable portion of the grain length is subjected to pressure oscillations near the resonance frequency of the combustion mechanism. On this basis a comparison of Tables X and XI affords some interesting conclusions.

In a 15-in. chamber, only a propellant with a very high burning rate should be susceptible to axial-mode instability. With a 0.5-in./sec burning rate, only the portion of the propellant near the ends of the chamber can experience pressure oscillations in the resonance range. With lower burning rates, no part of the combustion surface is in resonance with the waves. Thus, with propellants in the normal burning rate range the theory predicts that combustion instability should be difficult to initiate (or rarely experienced) in a 15-in. chamber. This agrees with the experimental observations.

Instability is much more likely in the 23-in. and 40-in. chambers. In the former, propellants with burning rates of 0.35 to 0.45 in./sec should be particularly susceptible to instability. The corresponding range in the 40-in. chamber is about 0.2 to 0.4 in./sec. The stability characteristics of a number of propellants have been thoroughly documented experimentally in a 40-in. chamber during this program. It is apparent that the burning rates of the propellants that encountered instability fell in the range of from 0.1 to 0.3 in./sec. Though this range is somewhat lower than that predicted theoretically, the agreement is well within the tolerances imposed by uncertainties in evaluating the thermochemical constants of the propellant. The theoretically predicted resonance-frequency bounds offer a plausible explanation for the fact that the high burning rate AP/KP propellant was stable, whereas the other one was not. They may also explain why the KP, Lip, and AN propellants were stable, as all these have resonance frequencies well outside the wave frequencies typical of a 40-in. motor. However, there is also another factor that may be significant here--the value of surface-coupled heat release which determines the amplitude of the burning rate response. This factor certainly appears to be important relative to the opposite behavior of the AN/KP and AN/AP propellants, which should have similar resonance frequencies.

It has been mentioned in the discussion of the experiments that the 82-in. motor always undergoes a transition to the first harmonic, which is an axial instability mode that exhibits the same frequency range as that shown for a 40-in. motor in Table IX. This is precisely

what one would expect for typical AP propellants ( $\bar{r} \sim 0.25$  to  $0.3$  in./sec) from the theoretical analysis of Table XI. The fundamental mode of the 82-in. motor corresponds to a frequency range (Table X) that is somewhat below the resonance frequency-response range of the propellant. However, the double-wave mode, which corresponds to the frequencies of a 40-in. motor, is right in the resonance range, as has already been shown. Thus the transition to this mode in the longer motor is consistent with the theoretical predictions.

For the propellants considered in the present study, with burning rates between  $0.25$  and  $0.3$  in./sec, the measured resonant frequency is approximately  $600$  cps (see Fig. 34) in a 40-in. motor, in agreement with the results presented in Table XI. According to Table X, this implies that the driving mechanism which sustains the waves is strongest near the ends of the motor. Indeed, this is not surprising because one could expect substantial losses in the reflection process at the chamber ends; if immediate reinforcement were not available, the shock process might be destroyed.

The foregoing discussion leads to an important conclusion: Axial-mode combustion instability was observed only under conditions in which the pressure pulse carried by the shock wave passed over the propellant at or near the theoretically predicted frequency of maximum propellant response, i.e., the resonant frequency. In all cases where the wave frequency was substantially different from the theoretical resonance frequency, no instability occurred. Thus, the data confirm the frequency criterion prescribed by the theory.

#### The Response Amplitude Criterion

The frequency criterion is a necessary but insufficient condition for the occurrence of axial-mode instability. Even if the wave frequency corresponds to the resonance frequency, no instability will arise unless the response amplitude of the propellant at this frequency is large enough to support the shock wave or to prevent attenuation of the shock by the following rarefaction wave. The theoretical treatment of the

propellant response wave interaction mechanism presented earlier in this report shows that the minimum response function  $R = 1/\sqrt{\tilde{m}/\tilde{p}}$  for combustion instability to occur is greater than 3.6 and probably is less than 10. For practical purposes it is convenient to identify the stability limit with a value of the normalized response function between these limits, e.g.,  $R \sim 7$ . Thus, when the maximum response amplitude of a propellant corresponds to  $R < 7$ , that propellant will have a low probability of exhibiting axial-mode combustion instability regardless of the frequency of the traveling wave. If  $R > 7$ , axial instability will be likely to arise whenever the frequency criterion is met.

It should be noted that the specific value chosen for the limiting  $R$  (in this case, 7) is not crucial; the resulting interpretation of experimental observations is equally valid for any arbitrarily chosen stability limit (or limiting response function) in the range  $3.6 < R < 10$ . The important point is that the theory introduces a second combustion instability criterion, in addition to the frequency criterion already discussed. Thus, for axial-mode combustion instability to occur<sup>1</sup> the frequency of passage of the wave over the propellant surface must be near the frequency of maximum combustion response to pressure disturbances, or resonant frequency, and (2) the amplitude of the response at that frequency must be sufficient to support the traveling shock wave. The theory predicts both the resonant frequency and the response amplitude at that frequency in terms of thermochemical parameters of the propellant. Consequently, if these parameters can be estimated or measured, the theory provides a method of avoiding axial-mode combustion instability by predicting the conditions under which it will occur.

It has already been shown that instability was observed experimentally only when the frequency coincided with the theoretically predicted resonant frequency. In particular, it was shown that the frequency condition for instability was met in the 40-in. motor, and for the first harmonic, in the 82-in. motor. The remaining task is to determine when a specific propellant will exhibit instability, assuming the frequency criterion, is met; i.e., it is necessary to introduce the second criterion,

that of response amplitude. This requires an interpretation of the data reported in Figs. 30 and 31; i.e., it is necessary to construct a theoretical stability map corresponding to that of Fig. 32 and to compare the results with experimental observations.

#### Theoretical Combustion Instability Limit

The first step in predicting the transient combustion behavior of real propellants is to characterize these propellants in terms of the thermochemical parameters that appear in the theory. If the correct parameters are used, the theoretical combustion model should provide a reasonable representation of both the steady-state burning rate curve for that propellant and the curve of the flame temperature vs. pressure. These requirements constitute an important restriction on the numerical values assigned to thermochemical parameters; they also provide a measure of the ability of the combustion model to describe steady-state combustion behavior. If the model cannot offer a reasonable description of known steady-state behavior, it is unlikely to correctly predict transient behavior.

Of about 20 AP propellants studied in this investigation (see Table VII), steady-state burning rate data over a relatively wide pressure range were obtained for five representative compositions. The data for these five propellants, along with the corresponding theoretical burning rate curves, are shown in Fig. 35. The theoretical curves represent the best fit of the data that is consistent with the flame temperature vs. pressure behavior of these propellants, which is known from separate thermochemical calculations. For PBAN 1C4, 244, and 284 a better fit could be obtained at elevated pressures by allowing the decomposition activation energy  $E$  to have two or more values over the whole pressure range, as may well be the case with these propellants. However, for present purposes the theoretical curves obtained with one value of  $E$  were deemed adequate.

The method of determining these theoretical burning rate curves is presented in Appendix D. The various thermochemical parameters were assigned according to the best available information pertinent to these

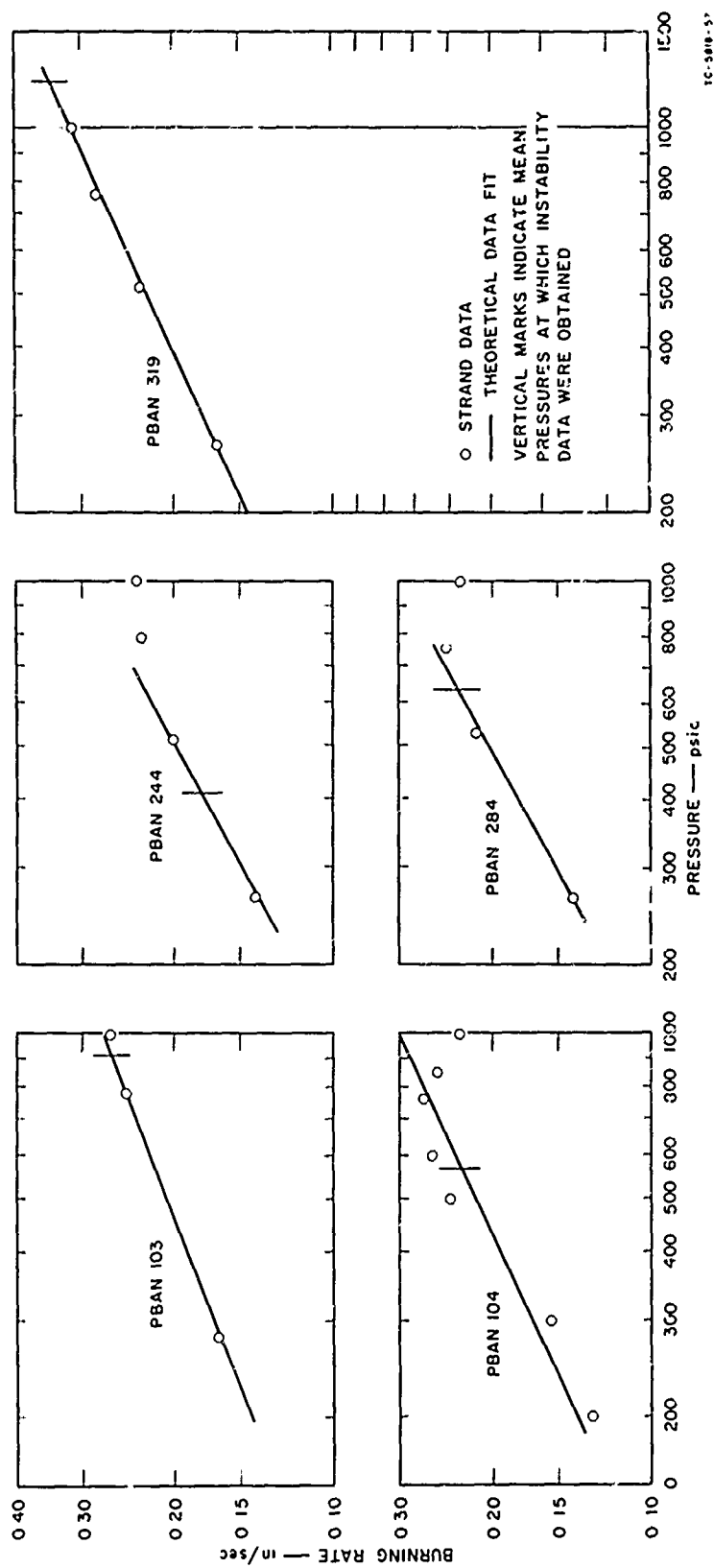


FIG. 35 BURNING RATE BEHAVIOR OF THE FIVE AP PROPELLANTS SELECTED FOR DETAILED ANALYSIS

and similar propellants. The chief assumption is that at a relatively low pressure (250 psi) the surface-coupled heat release is associated primarily with AP decomposition, including that from reactions very near the surface among decomposition products. Through this assumption the fraction of surface-coupled heat release associated with each propellant is determined.

The combustion model indicates that as one proceeds along the theoretical burning rate curve, from lower to higher pressure, the amplitude of the propellant response at the resonance frequency monotonically increases. It has been shown that when the normalized response function  $R = 1/\sqrt{\tilde{m}/\tilde{p}} > 7$ , combustion instability becomes highly probable. It is an easy matter to determine the point where this happens, corresponding to  $\alpha = 0.75$ , on each of the five theoretical burning rate curves given in Fig. 35. A curve drawn through these points represents the line along which  $R \sim 7$  for all thermochemically similar propellants; this curve is the stability limit for such propellants.

This concept is the basis of Fig. 36. The two dashed curves define the theoretically predicted stability limit for AP propellants. To the right of this limit band the propellants are predicted to be susceptible to axial-mode combustion instability in a 40-in. or 80-in. motor. To the left of the band, the propellants should be stable. The width of the limit band defines the inherent uncertainty in the theoretical method, as explained in Appendix D. This uncertainty is attributable mainly to the imperfect fit of the theoretical curves to the burning rate data (Fig. 35).

For comparison with the theory, all of the threshold pressure data obtained during the experimental investigation of AP propellants are replotted in Fig. 36. (These are the same data that appear in Figs. 30 and 31. The propellant corresponding to each data point is identified in Table VIII.) The threshold pressure indicated by each point is the lowest pressure at which the corresponding propellant exhibited axial-mode combustion instability. It is evident that the theoretically predicted stability limit is in good agreement with the experimental observations.

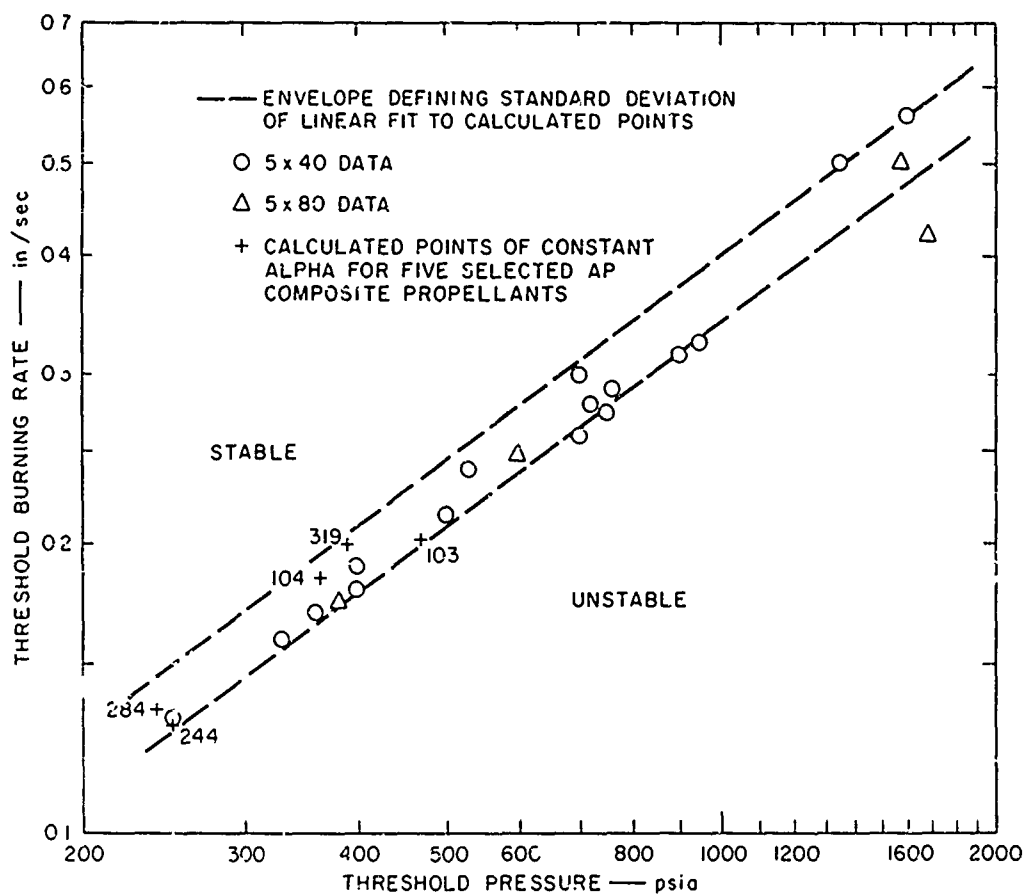


FIG. 36 STABILITY BOUNDARY OF AP PROPELLANTS SUBJECTED TO FINITE-WAVE, AXIAL-MODE PRESSURE DISTURBANCES

As was indicated in Fig. 32, propellants based on KP were experimentally found to be more stable than AP propellants; KP propellants did not exhibit axial-mode instability in the "unstable" zone of the AP stability map presented in Fig. 36. This observation is also explained by the theory, as will be shown.

Experimental measurements using the DTA technique confirmed the theoretical hypothesis that KP propellants have a substantially lower heat release due to solid-phase decomposition than AP propellants. (For example, see Figs. 19 and 20.) From the DTA data it was estimated that surface heat release might account for 15 to 20% of the total heat of



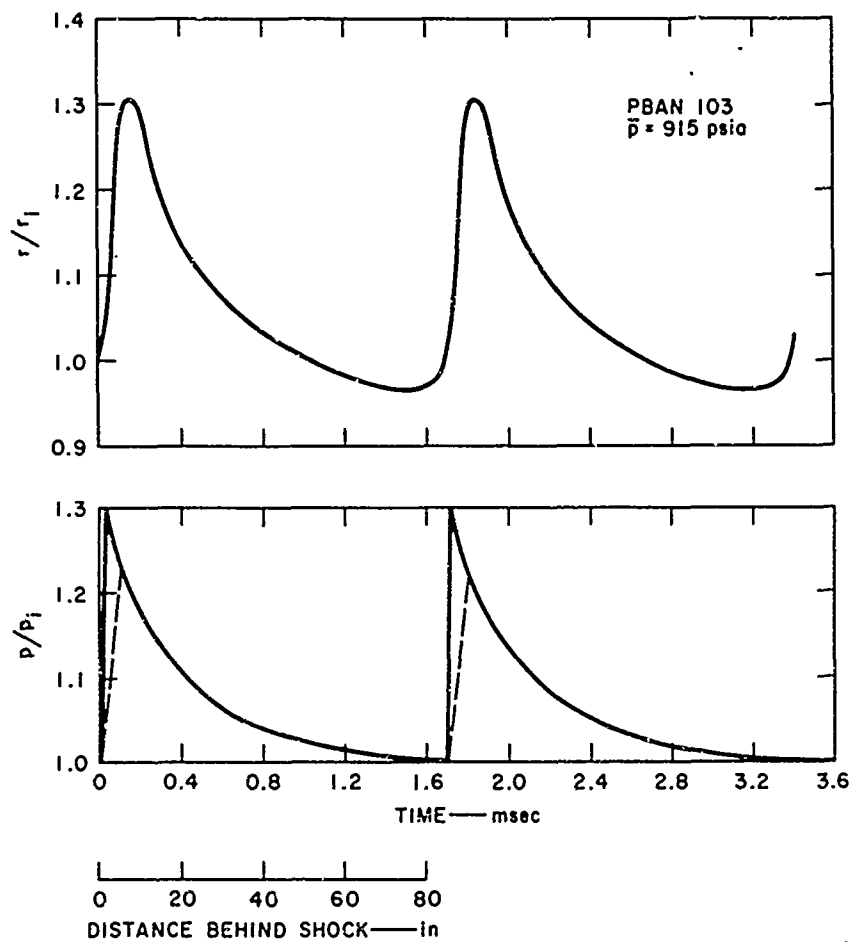
combustion for AP propellants, but only about 5% for KP propellants. The estimate for AP propellants was employed in constructing the theoretical stability limit depicted in Fig. 36. If the lower surface heat release estimate for KP propellants were used to develop a similar stability map for these propellants, the theoretical stability limit would be approximately parallel to that for AP propellants, but displaced to the right toward much higher pressures. Thus, the theoretically "stable" zone for KP propellants is much larger than that for AP propellants and includes most of the "unstable" zone in Fig. 36. Thus, the experimental observation that KP propellants were stable in the latter zone, as indicated in Fig. 32, is fully consistent with the theory.

#### The Propellant Response to a Steep-Fronted Pressure Wave

A calculation carried out in the "Theoretical Studies" section showed that a mass flux perturbation from the wall amounting to 1.6% of the mean mass flux in the motor is required to drive the observed instability wave at a Mach number of 1.2, according to the simplified analysis of Appendix C. The remaining task is to calculate the mass flux perturbation that is induced by the observed pressure wave in order to determine whether the wave can drive itself as hypothesized.

The nonlinear computer analysis outlined in Appendix B has been applied to the PBAN 103 composite AP propellant whose pressure wave is shown in Fig. 34. The wave form shown has been simplified to that depicted in the lower half of Fig. 37. The dashed line shows the response measured by the transducer whose rise time was limited by the cooling jacket required to withstand the rocket motor environment. Thus, the pressure wave shape is estimated for times less than 0.1 msec.

The propellant response obtained from the computer, using values for propellant parameters derived in Appendix D, is shown in the upper part of Fig. 37. This is the equilibrium response obtained at long times after the starting transients have died away. It can be seen that the net effect of the pressure wave is to increase the average burning rate because the average pressure is increased.



TA-5818-62

FIG. 37 THE CALCULATED PROPELLANT RESPONSE TO A SHARP-FRONTED PRESSURE WAVE

The mass flux perturbation up to any distance  $x$  behind the shock can now be calculated from the equation

$$\frac{m'}{m} = \frac{4}{L} \int_0^x (r^* - 1) dx \quad (17)$$

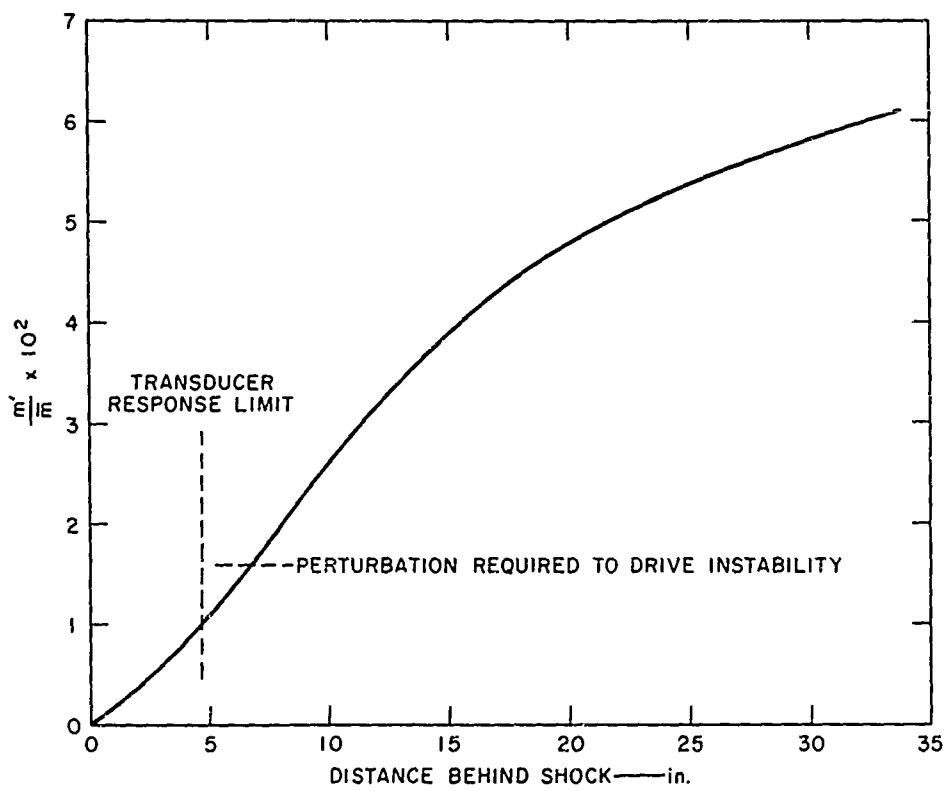
or, in terms of elapsed time as

$$\frac{m'}{m} = \frac{4V}{L} \int_0^t (r^* - 1) dt \quad (18)$$

where  $V$  is the shock velocity ( $4.7 \times 10^4$  in./sec) and  $L$  is the motor length. The factor 4 occurs if the mean mass flux at the quarter length point is used; this point corresponds closely to the frequency chosen for the pressure wave. Also shown in Fig. 37 is a distance scale obtained by converting elapsed time to distance through the shock velocity. Note that a complete pass, backward and forward, through the motor is required before the expansion is complete (see also Fig. 34).

The integral in Eq. 18 can be evaluated most easily by using a planimeter to obtain the area under the response curve of Fig. 37. The resulting prediction of  $m'/\bar{m}$  is shown in Fig. 38 as a function of distance behind the shock. The distance required to obtain the necessary perturbation ratio of  $1.6 \times 10^{-2}$ , which is needed to drive the wave, is nearly the same as the distance that is masked by the propellant response. This explains why the observed wave shape is a simple decay following the initial rise.

The above results indicate that the rather crude first-order calculation of the driving mechanism provides a surprisingly good phenomenological understanding of the event. The true picture is, of course, much more complicated because waves of two frequencies exist near the ends of the motor, but the basic mechanism has been delineated.



T4-5818-63

FIG. 38 INTEGRATED MASS ADDITION PERTURBATION AS A FUNCTION OF POSITION

## V. CONCLUSIONS AND RECOMMENDATIONS

From a relatively simple analysis it has been possible to construct a reasonably quantitative theoretical description of axial-mode, traveling wave combustion instability. The theory appears to be fully consistent with experimental observations obtained using motors that were pulsed with a powder charge. The observed correlation of instability with a restricted range of motor lengths is explained in terms of the theoretical frequency response of the propellant combustion mechanism, because the burning rate response amplitude required to drive the instability wave can only be obtained near the resonant frequency. Even at this frequency a certain minimum percentage of the total heat of combustion must arise from surface-coupled heat release in order to obtain a large enough response to support the wave.

This last observation explains why KP propellants were observed experimentally to be stable under conditions in which AP propellants were unstable. Differential thermal analysis measurements show that KP propellants typically have at most one-third as much surface-coupled heat release as do AP propellants, so that their response amplitude in the pressure regime tested (up to 2000 psia) was too low to support a traveling wave, even at the resonant frequency. Thus, the theoretical stability boundary for KP propellants in the burning rate/pressure coordinate system would be displaced from the AP boundary toward much higher pressures.

These results can now be applied as guidelines that can be used to minimize the occurrence of finite-amplitude axial-mode combustion instability in future solid propellant rockets. The guidelines can be stated as follows:

1. The motor configuration should be chosen so that the motor length divided by any whole number does not correspond to the fundamental propellant resonant frequency. This will eliminate not only single-mode instabilities, but also dual and higher modes (note that a dual-mode instability occurred in the 82-in. motor experiments).

2. If it is necessary to operate in a length regime that corresponds closely to the resonant frequency, a propellant having a low proportion of surface heat release at the desired burning rate should be selected. This means that the propellant that exhibits the desired burning rate at the lowest possible pressure is the most desirable; i.e., catalyzed propellants are more stable than uncatalyzed ones.
3. The AP stability boundary in the burning rate/pressure plane is defined by results obtained from some 20 propellants containing many different additives. The consistency of the data indicates that this curve can be applied to any AP propellant to obtain the pressure boundary of stability once the strand burning rate curve has been measured.

In summary, well-documented combustion instability characteristics of many propellant systems have been interpreted successfully in terms of theoretical propellant response characteristics, providing a means of stability calculation not available heretofore.

## APPENDIX A

### LINEAR ANALYSIS OF THE COMBUSTION MODEL BASED ON A TRANSFORMATION

Following the usual small-perturbation procedure, it is convenient to assume that each dependent variable, as well as the pressure, is the sum of a steady and a perturbed component:

$$\begin{aligned} p^* &= 1 + \tilde{p} \\ T_f^* &= 1 + \tilde{T}_f \\ T_w^* &= 1 + \tilde{T}_w \\ r^* &= 1 + \tilde{r} \end{aligned} \tag{A1}$$

where, for example,  $\tilde{p}$  is the ratio  $[p(t) - \bar{p}]/\bar{p} \ll 1$ . By introducing these expressions into Eqs. (1), (2), (3), (7), and (10) and retaining only first-order terms in the perturbed quantities, one can obtain a set of linear equations. The solution to these equations gives the first-order response of the combustion mechanism to a perturbation in the chamber pressure.

The results of Denison and Baum's analysis<sup>12</sup> for the case of zero surface heat release can be applied to the more general combustion model formulated during this investigation when the proper transformation of variables is defined. With the assumption of a constant gas-phase heat release ( $Q_r = \text{constant}$ ) the transformation takes the form

$$\left. \begin{aligned} \alpha &= \alpha_o - \frac{\theta_s}{A} \\ B &= \frac{\alpha_o B_o + m_H^* (1 - T_o^*)}{\alpha_o - \theta_s/A} \end{aligned} \right\} \tag{A2}$$

where:

$$A = A_o = \frac{E_w}{RT_w} \left( \frac{\tilde{T}_w - T_o}{\tilde{T}_w} \right)$$

$$\alpha_o = \frac{c_p \bar{T}_f}{c_s (\bar{T}_w - T_o)} \left( \frac{1}{\frac{n+2}{2} + \frac{E_f}{2R\bar{T}_f}} \right)$$

$$\theta_s = \left[ \left( \frac{E_H}{R\bar{T}_w} - m \right) \zeta_H + \frac{E_D}{R\bar{T}_w} \zeta_D \right] (1 - T_o^*)$$

The effective steady-state pressure exponent  $\nu$  (in the usual empirical burning rate formula,  $r = cp^\nu$ ) changes from  $n/2$  to

$$\nu = \frac{\alpha_o \frac{n}{2} + m\zeta_H}{\alpha_o - \theta_s/A} \quad (A3)$$

The subscript o on  $\alpha$ ,  $B$ , and  $A$ , denotes the value, as defined by Denison and Baum,<sup>12</sup> for zero surface-coupled heat release. The parameter  $\theta_s$  is a measure of the total heat release that occurs in surface-coupled reactions.



## APPENDIX B

### THE NUMERICAL ANALYSIS OF THE NONLINEAR THEORETICAL COMBUSTION MODEL

The mathematical description of the model begins with the equation governing heat conduction in the solid phase beyond the surface reaction zone:

$$\frac{\partial T}{\partial t} = r(t) \frac{\partial T}{\partial x} + \kappa \frac{\partial^2 T}{\partial x^2} \quad (B1)$$

The following boundary condition is imposed upon the temperature:

$$T \rightarrow T_0 \text{ as } x \rightarrow \infty \quad (B2)$$

The remaining boundary condition is obtained through an energy-flux balance at the gas-solid interface. The result is

$$\begin{aligned} -k \left( \frac{\partial T}{\partial x} \right)_w = \rho_s r \left[ \epsilon_r Q_r - L - c_p (T_f - T_0) + c_s (T_s - T_0) \right. \\ \left. + H_H \left( \frac{p}{T_w} \right)^m e^{-E_H/RT_w} + H_D e^{-E_D/RT_w} \right] \end{aligned} \quad (B3)$$

The final two equations that complete the description of the basic combustion model are the assumed Arrhenius propellant pyrolysis law

$$r = ae^{-E_w/RT_w} \quad (B4)$$

and the expression that relates the burning rate to the instantaneous gas-phase reaction rate (i.e., the flame speed)

$$r = C_p T_f^{n/2} T_f^{1+n/2} e^{-E_f/2RT_f} \quad (B5)$$

Equations B1, B4, and B5 describe the behavior of the three unknowns  $r$ ,  $T$ , and  $T_f$  when the time dependence of the pressure is specified as the input driving force. To obtain a general solution for these three unknowns, it is convenient to nondimensionalize the equations by defining the variables

$$x^* = \frac{r_i x}{K}, \quad t^* = \frac{r_i^2 t}{K}, \quad T^* = \frac{T}{T_{wi}}, \quad p^* = \frac{p}{p_i}, \quad r^* = \frac{r}{r_i},$$

$$Q_H^* = \left( \frac{p^*}{T_w^*} \right)^m e^{\frac{E_H}{RT_{wi}} \frac{T_w^* - 1}{T_w^*}}, \quad Q_D^* = e^{\frac{E_D}{RT_{wi}} \frac{T_w^* - 1}{T_w^*}},$$

$$\zeta_H = \frac{H_H}{c_s(T_{wi} - T_o)} \left( \frac{p_i}{T_{wi}} \right)^m e^{-\frac{E_H}{RT_{wi}}}, \quad \zeta_D = \frac{H_D}{c_s(T_{wi} - T_o)} e^{-\frac{E_D}{RT_{wi}}}$$

Equations B1 through B5 then become

$$\frac{\partial T^*}{\partial t^*} = r^* \frac{\partial T^*}{\partial x^*} + \frac{\partial^2 T^*}{\partial x^{*2}} \quad (B6)$$

$$T^* \rightarrow T_o^* \text{ as } x^* \rightarrow \infty \quad (B7)$$

$$-\left( \frac{\partial T^*}{\partial x^*} \right)_w = r^* \left[ \frac{\epsilon_r Q_r - L}{c_s T_{wi}} - \frac{c_p}{c_s} \left( \frac{T_{fi}}{T_{wi}} T_f^* - T_o^* \right) + (T_w^* - T_o^*) \right. \\ \left. + (\zeta_H Q_H^* + \zeta_D Q_D^*) (1 - T_o^*) \right] \quad (B8)$$

$$r^* = e^{\frac{E_w}{RT_{wi}} \frac{T_w^* - 1}{T_w^*}} \quad (B9)$$

$$r^* = p^{*n/2} T_f^{*1} + n/2 \frac{E_f}{2RT_{fi}} \frac{T_f^* - 1}{T_f^*} \quad (B10)$$

The quantity  $Q_r$  in Eq. B8 represents the heat release in the gas-phase combustion zone; its transient behavior is generally, unknown. However, it is reasonable to assume that during nonsteady combustion, the gas-phase heat release will be the same as its steady-state value for the same total heat release in surface-coupled terms. Note that such an assumption does not relate the instantaneous value of  $Q_r$  to the instantaneous value of  $p$  or  $T_w$ , but rather to the instantaneous heat release connected with the surface. Using this assumption, the boundary condition of Eq. B8 can be written as

$$-\left(\frac{\partial T^*}{\partial x}\right)_w = r^* \left[ \frac{c_p}{c_s} \frac{T_{fi}}{T_{wi}} (\tilde{T}_f^* - T_f^*) + (T_w^* - T_o^*) \right] \quad (B11)$$

where  $\tilde{T}_f^*$  is a fictitious flame temperature obtained from a simultaneous solution of the equations

$$\tilde{r}^* = e \frac{E_w}{RT_{wi}} \frac{\tilde{T}_w^* - 1}{\tilde{T}_w^*} \quad (B12)$$

$$\tilde{T}_f^* = \tilde{T}_f^*(p^*) \quad (B13)$$

$$\tilde{r}^* = f(\tilde{p}^*) \quad (B14)$$

$$\zeta_H \tilde{Q}_H^* + \zeta_D \tilde{Q}_D^* = \zeta_H Q_H^* + \zeta_D Q_D^* \quad (B15)$$

Note that the heat conduction equation (Eq. B6) has been replaced by Eq. B14 which represents the steady-state empirical burning rate law of the propellant under consideration. In addition, the flame

temperature equation (Eq. B10) has been replaced by the thermochemical equation (Eq. B13).

To obtain a numerical solution to Eq. B6, it is necessary to transform the infinite spatial coordinate  $x^*$  into a finite coordinate  $y^*$ . The transformation

$$y^* = 1 - e^{-x^*} \quad (\text{B16})$$

which changes  $0 < x^* < \infty$  into  $0 < y^* < 1$  is most convenient because steady-state temperature profiles are given by

$$\frac{T^* - T_o^*}{T_w^* - T_o^*} = (1 - y^*) r^* \quad (\text{B17})$$

Note that the initial steady-state profile, corresponding to  $r^* = 1$ , is linear. Using transformation B16, Eq. B6 becomes

$$\frac{\partial T^*}{\partial t^*} = (r^* - 1)(1 - y^*) \frac{\partial T^*}{\partial y^*} + (1 - y^*)^2 \frac{\partial^2 T^*}{\partial y^{*2}} \quad (\text{B18})$$

In addition

$$\left( \frac{\partial T^*}{\partial y^*} \right)_w = \left( \frac{\partial T^*}{\partial x^*} \right)_w \quad (\text{B19})$$

The heat conduction equation (Eq. B18) can be solved numerically in a number of ways. Here the implicit method of Crank and Nicolson<sup>4</sup> has been chosen because of the relative freedom allowed in the choice of the time step size relative to the distance step size. Both spatial and temporal derivatives are replaced by finite differences, and the time derivative evaluated at  $(t^* + \delta t^*)$ . The time derivative becomes

$$\frac{\partial T^*}{\partial t^*} = \frac{T^*(y^*, t^* + \delta t^*) - T^*(y^*, t^*)}{\delta t^*} \quad (\text{B20})$$

while the space derivatives become

$$\begin{aligned} \frac{\partial T^*}{\partial y^*} &= \frac{T^*(y^* + \delta y^*, t^*) + T^*(y^* + \delta y^*, t^* + \delta t^*)}{4\delta y^*} \\ &\quad - \frac{T^*(y^* - \delta y^*, t^*) + T^*(y^* - \delta y^*, t^* + \delta t^*)}{4\delta y^*} \end{aligned} \quad (B21)$$

and

$$\begin{aligned} \frac{\partial^2 T^*}{\partial y^{*2}} &= \frac{T^*(y^* + \delta y^*, t^*) + T^*(y^* + \delta y^*, t^* + \delta t^*)}{2(\delta y^*)^2} \\ &\quad + \frac{T^*(y^* - \delta y^*, t^*) + T^*(y^* - \delta y^*, t^* + \delta t^*)}{2(\delta y^*)^2} \\ &\quad - \frac{2T^*(y^*, t^*) + 2T^*(y^*, t^* + \delta t^*)}{2(\delta y^*)^2} \end{aligned} \quad (B22)$$

Defining  $K = \delta t^*/(\delta y^*)^2$ , Eqs. B20, B21, and B22 can be combined to give the final difference equation:

$$\begin{aligned} T^*(y^*, t^* + \delta t^*) &= \frac{K}{2} \frac{1}{1 + K(1 - y^*)^2} \\ &\quad \left\{ \left[ (1 - y^*)^2 + (r^* - 1)(1 - y^*) \right] \left[ T^*(y^* + \delta y^*, t^*) + T^*(y^* + \delta y^*, t^* + \delta t^*) \right] \right. \\ &\quad \left. + \left[ (1 - y^*)^2 - (r^* - 1)(1 - y^*) \right] \left[ T^*(y^* - \delta y^*, t^*) + T^*(y^* - \delta y^*, t^* + \delta t^*) \right] \right\} \\ &\quad + \frac{1 - K(1 - y^*)^2}{1 + K(1 - y^*)^2} T^*(y^*, t^*) \end{aligned} \quad (B23)$$

Note that the temperature at any point depends upon the temperature at the two adjacent points at the same time; this implicitness assures

rapid convergence for any value of K. Also, since the temperature at  $-\delta y^*$  is not of interest, it is convenient to combine Eqs. B21 and B23 at  $y^* = 0$  to obtain

$$T^*(0, t^* + \delta t^*) = \frac{K}{1 + K} \left\{ T^*(\delta y^*, t^*) + T^*(\delta y^*, t^* + \delta t^*) - 2 \left[ 1 - (r^* - 1) \frac{\delta y^*}{2} \right] \delta y^* \left( \frac{\partial T^*}{\partial y^*} \right)_w \right\} + \frac{1 - K}{1 + K} T^*(0, t^*) \quad (B24)$$

where  $\left( \frac{\partial T^*}{\partial y^*} \right)_w$  is given by Eq. B11 (see Eq. B19).

Equations B9, B10, B11, B23, and B24 have been programmed in Fortran IV for general computation. The method of solution proceeds as follows: With known values of  $p^*$  and  $r^*$  at time  $t^*$ , Eq. B10 is used to obtain the value of  $T_f^*$  at the next time  $(t^* + \delta t^*)$ . With known values of  $p^*$  and  $T_w^*$  at time  $t^*$ ,  $Q_H^*$  and  $Q_D^*$  are calculated and used with Eqs. B12 through B15 to obtain  $\tilde{T}_f^*$ . Then Eqs. B11, B23, and B24 are solved for a new value of  $T_w^*$  which is then used in Eq. B9 to obtain a new value of  $r^*$ . The known value of  $p^*$  and this new value of  $r^*$  are then used to repeat the entire process, until no further change is noted in  $T_f^*$  or  $T_w^*$ . This completes the calculation for one time step.

## APPENDIX C

### REINFORCEMENT OF A SHOCK WAVE BY A MASS SOURCE

The traveling wave instability data obtained during the course of this program shows that once an equilibrium pressure wave is established, the wave pattern traverses the chamber with no change in shape. That is, the shock wave is followed closely by an expansion process which does not overtake it; an equilibrium situation of this kind can only occur if the flow behind the shock is accelerated over a very short distance to a local Mach number of unity so that the following sonic velocity expansion waves can never overtake the shock wave and destroy it.

The pressure change across the shock wave induces an enhanced burning rate according to the response function theory discussed previously. Here the effect of such a mass addition on the flow immediately behind the shock will be considered. For simplicity it will be assumed that the flow is quasi-one-dimensional with the mass added uniformly across the cross section. The flow process is described by the equations which express conservation of mass, momentum, and energy.

The continuity equation for mass conservation is

$$\frac{d(\rho u)}{dx} = \dot{m} \quad (C1)$$

where  $\dot{m}$  is the mass addition per unit length. The momentum equation is

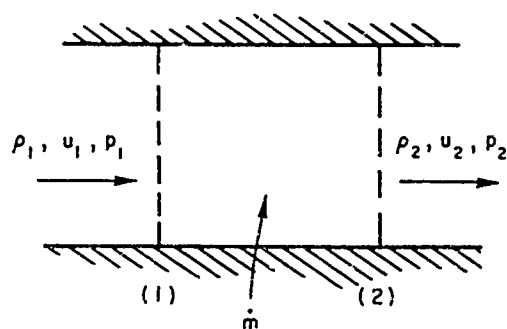
$$\rho u \frac{du}{dx} = - \frac{dp}{dx} \quad (C2)$$

and the energy equation is

$$\rho u \frac{d(h + u^2/2)}{dx} = \rho u \dot{m} H \quad (C3)$$

where  $H$  is the energy per unit mass of the material being added to the flow.

Consider now the region between station (1) and station (2) shown in Fig. C-1. Station (1) is assumed to lie just behind the shock wave



TA-5818-64

C-1 THE MASS ADDITION PROCESS BEHIND THE SHOCK WAVE

and station (2) at an undefined (as yet) downstream point. Equations C1, C2, and C3 can now be integrated between the two stations to obtain their integral forms:

$$\rho_2 u_2 = \rho_1 u_1 + \int_1^2 \dot{m} \, dx \quad (C4)$$

$$p_2 + \rho_2 u_2^2 = p_1 + \rho_1 u_1^2 + \int_1^2 \dot{m} H \, dx \quad (C5)$$

$$h_2 + \frac{u_2^2}{2} = h_1 + \frac{u_1^2}{2} + \frac{1}{\rho_1 u_1} \int_1^2 \dot{m} H \, dx \quad (C6)$$

Let

$$I_1 = \int_1^2 \dot{m} \, dx$$

$$I_2 = \int_1^2 \dot{m} u \, dx$$

$$I_3 = \frac{1}{\rho_1 u_1} \int_1^2 \dot{m} H \, dx$$

Assuming that the enthalpy can be expressed as  $h = c_p T$ , Eq. C6 can be written as



$$1 + \frac{\gamma - 1}{2} M_1^2 + \frac{I_3}{c_p T_1} = \frac{T_2}{T_1} \left( 1 + \frac{\gamma - 1}{2} M_2^2 \right) \quad (C7)$$

From the equation of state ( $p = \rho RT$ )

$$\frac{T_2}{T_1} = \frac{p_2}{p_1} \frac{\rho_1}{\rho_2} = \frac{p_2}{p_1} \frac{\rho_1 u_1}{\rho_2 u_2} \frac{M_2}{M_1} \left( \frac{T_2}{T_1} \right)^{\frac{1}{2}}$$

or

$$\frac{T_2}{T_1} = \left( \frac{p_2}{p_1} \right)^2 \left( \frac{\rho_1 u_1}{\rho_2 u_2} \right)^2 \left( \frac{M_2}{M_1} \right)^2 \quad (C8)$$

Using Eqs. C4, C5, and C8, Eq. C7 can be written in the form

$$1 + \frac{\gamma - 1}{2} M_1^2 + \frac{I_3}{c_p T_1} = \left[ \frac{1 + \gamma M_1^2}{1 + \gamma M_2^2} + \frac{I_2/p_1}{I + \gamma M_2^2} \right]^2 \left[ \frac{1}{1 + I_1/\rho_1 u_1} \right]^2 \left[ \frac{M_2}{M_1} \right]^2 \left( 1 + \frac{\gamma - 1}{2} M_2^2 \right) \quad (C9)$$

If  $I_1$ ,  $I_2$ , and  $I_3$  were specified, Eq. C9 would relate the Mach numbers at station (1) and station (2). Alternatively, if  $M_1$  and  $M_2$  were specified, this equation could be used to specify relations between the three integrals. In this case, the condition of interest is  $M_2 = 1$  in order to avoid the trailing expansion process. Also, since the shock wave is weak, with a typical Mach number being 1.2, the integrals can be simplified to:

$$\frac{I_1}{\rho_1 u_1} = I$$

$$\frac{I_2}{p_1} \approx \frac{I_1 u_1}{p_1} = \gamma M_1^2 I$$

$$\frac{I_3}{c_p T_1} \approx \frac{I_1}{\rho_1 u_1} = I$$

Equation C9 now becomes

$$\frac{M_1^2 \left(1 + \frac{\gamma - 1}{2} M_1^2 + I\right)(1 + I)^2}{[1 + \gamma M_1^2 (1 + I)]^2} = \frac{M_2^2 \left(1 + \frac{\gamma - 1}{2} M_2^2\right)}{(1 + \gamma M_2^2)^2} \quad (C10)$$

When  $M_2$  is unity, the equation reduces to its final form of interest

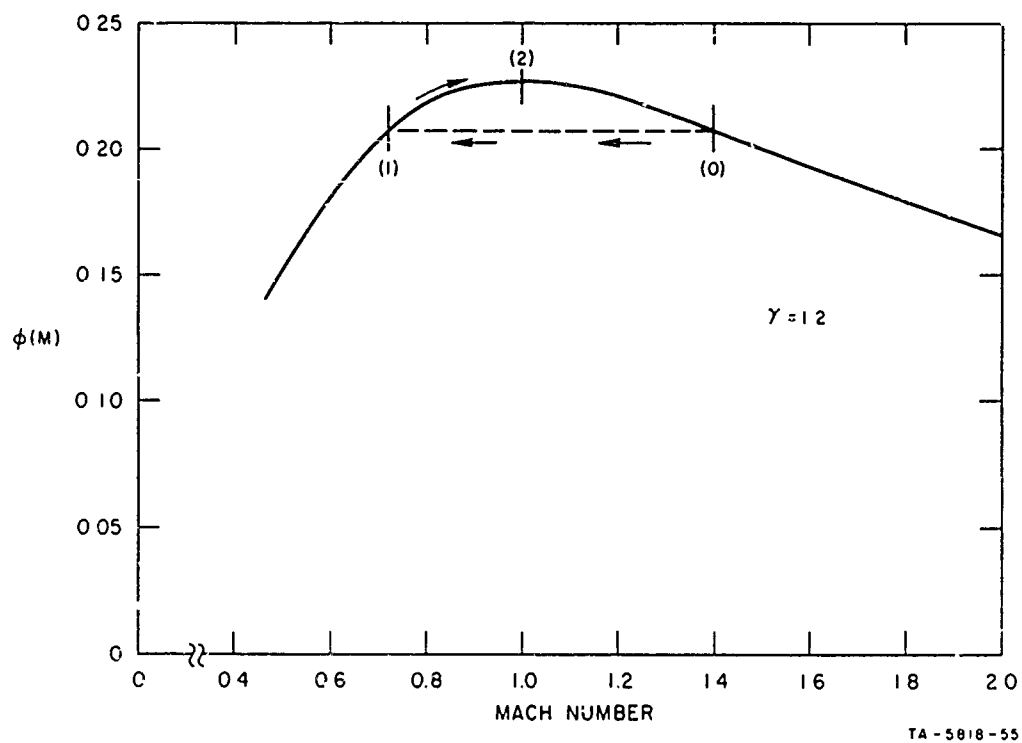
$$\frac{M_1^2 \left(1 + \frac{\gamma - 1}{2} M_1^2 + I\right)(1 + I)^2}{[1 + \gamma M_1^2 (1 + I)]^2} = \frac{1}{2(1 + \gamma)} \quad (C11)$$

Note that Eq. C10 was originally derived for the region stretching from just behind the shock to some downstream point such as the point defined by  $M_2 = 1$ . Closer examination of Eq. C10, however, shows that if the shock process is considered as a discontinuity with  $I = 0$  through the infinitesimal shock region (no mass addition), the quantity

$$\phi(M) = \frac{M^2 \left(1 + \frac{\gamma - 1}{2} M^2\right)}{(1 + \gamma M^2)^2} \quad (C12)$$

is preserved across the shock wave, so that Eq. C11 actually exhibits a double-valued solution for the Mach number. The larger value is the Mach number of the traveling wave and the smaller value is the Mach number just behind the wave. Thus, Eq. C11 can be interpreted as an equation relating the Mach number of wave travel to the quantity  $I$ .

This concept is depicted graphically in Fig. C-2 where  $\phi(M)$  is plotted versus  $M$ . Note that  $\phi(M)$  has a maximum at  $M = 1$ , showing that mass and/or energy addition behind a shock can at most drive the flow to sonic conditions in a one-dimensional process. A typical path for the process being investigated here proceeds as shown: first, a jump in Mach number from  $M_0$  to  $M_1$  occurs across the shock with  $\phi(M)$  constant, followed by an increase in Mach number along the  $\phi(M)$  curve until the sonic point is reached. If  $M_0$  is specified, Eq. C11 can be solved for the required mass addition  $I$  that can then be compared to the available mass addition calculated from the propellant response function.



C-2 BEHAVIOR OF THE MACH NUMBER FUNCTION  $\phi$

## APPENDIX D

### DERIVATION OF THE CALCULATED STABILITY LIMIT

In order to derive the theoretical stability limit in the burning rate-pressure coordinate system, five propellants that had been thoroughly documented (see the "Experimental Studies" section) were chosen as being representative of the many that were tested. Since the losses associated with the chamber should be practically independent of the propellant formulation and dependent on the geometry instead, it is plausible to assume that the limit line represents a line along which the burning rate response function  $\tilde{m}/\sqrt{p}$  is constant for each propellant at the point where its burning rate curve crosses the limit line. If  $A$  is chosen as being constant for the family of AP propellants being considered here, a constant burning rate response implies a constant value of the parameter  $\alpha$  since one would expect the burning rate response to fall in the linear range in the vicinity of the limit line.

When the basic decision has been made to treat the stability limit as a line of constant  $\alpha$ , the calculational procedure required to delineate the line consists of two steps: (1) a theoretical fit to the measured burning rate/pressure curves, and (2) a calculation of the variation of  $\alpha$  along the theoretical curve to determine the point at which  $\alpha$  reaches its desired value.

To fit the measured burning rate curve obtained from strand data, it was assumed that

$$r = C_1 + C_2 p + C_3 \log p \quad (D1)$$

The values of  $C_1$ ,  $C_2$ , and  $C_3$  obtained for the five propellants under consideration are given in Table D-1. Thermochemical calculations for these propellants indicated that the variation of flame temperature could be expressed to first order as

$$T_f^* = r^{*0.04} \quad (D2)$$

Table D-1  
PROPELLANT PARAMETERS REQUIRED FOR THEORETICAL ANALYSIS

Propellant	$C_1$	$C_2$	$C_3$	$n$	$A$	$\alpha_o$	$\alpha$	$r^{(a)}$ (in.sec)	$p^{(a)}$ (psia)
PBAN 103	$-7.58 \times 10^{-2}$	$8.02 \times 10^{-5}$	$3.90 \times 10^{-2}$	0.65	12.1	0.82	0.75	0.202	470
PBA. 104	$-8.94 \times 10^{-2}$	$1.17 \times 10^{-4}$	$3.93 \times 10^{-2}$	0.77	12.1	0.81	0.75	0.184	363
PBAN 244	$-9.06 \times 10^{-2}$	$1.41 \times 10^{-4}$	$3.48 \times 10^{-2}$	0.91	12.1	0.80	0.75	0.131	247
PBAN 204	$-8.89 \times 10^{-2}$	$1.52 \times 10^{-4}$	$3.40 \times 10^{-2}$	0.93	11.9	0.80	0.75	0.133	240
PBAN 319	$-9.45 \times 10^{-2}$	$1.13 \times 10^{-4}$	$4.19 \times 10^{-2}$	0.76	11.9	0.81	0.75	0.200	395

(a) Threshold conditions

The additional steady state equation to be satisfied is the equation relating the burning rate to the gas-phase flame speed:

$$r^* = p^{n/2} \frac{T_f^*}{T_f}^{1 + n/2} \frac{(E_f/2RT_{f1})(T_f^* - 1)/T_f^*}{e} \quad (D3)$$

The use of Eqs. D1 and D2 in Eq. D3 and the choice of a suitable value for the flame activation energy allows the calculation of a value for the effective order  $n$  of the gas phase reaction. Using a value of 12.5 kcal/mole for  $E_f$ , the values of  $n$  shown in Table D-1 have been computed. The flame temperature at a pressure of 50 psia has been taken to be 2150°K in accordance with the results of the thermochemical calculations.

In order to calculate the values of the linear parameters  $A$ ,  $\alpha_o$ , and  $\alpha$  as the burning rate increases with pressure, it is necessary to choose values for  $T_w$ ,  $T_o$ ,  $E_w$ ,  $E_H$ , and  $E_D$ . Here it has been assumed that  $T_w = 800^\circ\text{K}$  at a pressure of 50 psia,  $T_o = 300^\circ\text{K}$ ,  $E_w = 32$  kcal/mole, and  $E_H = E_D = 20$  kcal/mole. The parameter  $A$ , which is given by

$$A = \frac{E_w}{RT_w} \left( 1 - \frac{T_o}{T_w} \right) \quad (D4)$$

is approximately equal to 12 along the limit line, as shown in Table D-1. The parameter  $\alpha_o$  is given by

$$\alpha_o = \frac{c_p T_f}{c_s (T_w - T_o)} \frac{1}{1 + n/2 + E_f/2RT_f} \quad (D5)$$

Assuming that  $c_p/c_s = 1$ , the value of  $\alpha_o$  can be calculated along the burning rate pressure curve. The parameter which governs the magnitude of the response is  $\alpha$  (see Appendix A), which involves choices for the values of the heat release parameters  $\zeta_H$  and  $\zeta_D$ ; i.e.,

$$\alpha = \alpha_o - \frac{[(E_H/RT_w - m)\zeta_H + (E_D/RT_w)\zeta_D](1 - T_o^*)}{A} \quad (D6)$$

The choice of the ratio  $\zeta_H/\zeta_D$  will obviously affect the slope of the constant- $\alpha$  stability limit line in the burning rate/pressure plane

because of the direct pressure sensitivity of  $\zeta_H$  (see Appendix A). In order to generate a slope in agreement with the experimental results, it has been assumed that  $\zeta_H/\zeta_D = 5$  at a pressure of 250 psia.

The choice for the variation in  $\zeta_H$  and  $\zeta_D$  as one moves from one propellant curve to another requires additional consideration. Here it has been assumed that at a fixed pressure the proportion of surface-coupled heat release depends inversely on the burning rate; i.e., at a fixed pressure the surface heat release associated with a fixed AP loading (all of the propellants considered here contained a nominal loading of 80% AP) is constant. This constraint was applied at 250 psia and allowed the calculation of  $\alpha$  along one propellant burning rate curve to be related to similar calculations along other curves.

Finally, suitable choices for the magnitudes of  $\zeta_H$  and  $\zeta_D$  would allow the calculation of  $\alpha$  along each propellant. An alternative procedure, which has been adopted here, is to choose the value of  $\alpha$  which is desired at the limit line and back calculate  $\zeta_H$  and  $\zeta_D$  for each propellant. As pointed out in the "Theoretical Studies" section, a response amplitude  $\tilde{m}/\tilde{v}_p$  of the order of 5 is required to support the wave. Using the results of Fig. 2 with a value of  $A = 12$ ,  $\alpha$  has been chosen as 0.75 on the stability limit line; this gives a response amplitude of 7. The corresponding values of  $\zeta_H$  and  $\zeta_D$  for the point where each of the five propellants of Table D-1 have a value of 0.75 for  $\alpha$  are 0.24 and 0.02, respectively.

The threshold burning rate/pressure conditions for each of the five propellants, calculated according to the procedure outlined above, are listed in Table D-1 and shown in Fig. 36. These five calculated points were then fit with a linear least-squares error curve in the log r-log p coordinate system, and the lines representing the standard deviation of the points were generated. These two curves are also shown on Fig. 36.

## REFERENCES

1. Capener, E. L., et al., "Response of a Burning Propellant Surface to Erosive Transients," Stanford Research Institute Final Report prepared for AFOSR, Contract No. AF 49(638)-1507, March 15, 1966.
2. Capener, E. L., et al., "Response of a Burning Propellant Surface to Erosive Transients," Stanford Research Institute Annual Report prepared for AFOSR, Contract No. AF 49(638)-1665, December 31, 1966.
3. Capener, E. L., Dickinson, L. A., and Kier, R. J., "Driving Processes of Finite-Amplitude Axial-Mode Instability in Solid Propellant Rockets," AIAA J. 5, 938-945 (1967).
4. Hart, R. W., and McClure, F. T., "Theory of Acoustic Instability in Solid Propellant Rocket Combustion," Proc. Tenth Symposium (International) on Combustion, The Combustion Institute, Pittsburgh, Pa., 1965, pp. 1047-1065.
5. Friedly, J. C., and Petersen, E. E., "Influence of Combustion Parameters on Instability in Solid Propellant Motors: Part I. Development of Model and Linear Analysis," AIAA J. 4, 1604-1610 (1966); "Part II. Nonlinear Analysis," AIAA J. 4, 1932-1937 (1966).
6. Culick, F.E.C., "Calculation of the Admittance Function for a Burning Surface," presented at the Third ICRPG Combustion Conference, J.F. Kennedy Space Center, Cocoa Beach, Fla., October 1966.
7. Vantoch, P., "Combustion Instability in Solid Propellant Rockets," For. Sci. Bull. 1 (9) (September 1965).
8. Marxman, G. A., "Theoretical Model of Solid Propellant Response in Combustion Instability and Extinction," presented at Third ICRPG Combustion Conference, J.F. Kennedy Space Center, Cocoa Beach, Fla., October 1966.
9. Marxman, G. A., and Wooldridge, C. E., "The Effect of Surface Reactions on the Solid Propellant Response Function," AIAA J. 6, 471-478 (1968).



10. Brown, R. S., Muzzy, R. J., and Steinle, M. E., "Surface Reaction Effects on the Acoustic Response of Composite Solid Propellants," Paper No. WSCI-67-17, presented at the 1967 Spring Meeting, Western States Section, Combustion Institute, La Jolla, Calif., May 1967.
11. Krier, H., T'ien, J. S., Sirignano, W. A., and Summerfield, M., "Non-Steady Burning Phenomena of Solid Propellants: Theory and Experiments," Second ICRPG/AIAA Solid Propulsion Conference, Anaheim, Calif., June 1967.
12. Denison, M. R., and Baum, E., "A Simplified Model of Unstable Burning in Solid Propellants," ARS J. 31, 1112-1122 (1961).
13. Istratove, A. G., and Librovich, V. B., "Combustion Stability of Propellants," Zhurnal prikladnoy mekhaniki i techcheskoy fiziki 3, 139-144 (1964).
14. Novikov, S. S., and Ryazantsev, Yu. S., "The Theory of Combustion of Condensed Systems," In: Akademiya nauk SSSR. Doklady 157(6), 1448-1450 (1964).
15. Novikov, S. S., and Ryazantsev, Yu. S., "The Theory of the Steady-State Velocity of Propagation of an Exothermal Reaction Front in a Condensed Medium," Zhurnal prikladnoy mekhaniki i fiziki 3, 43-48 (1965).
16. Beckstead, M. W., and Culick, F.E.C., "A Comparison of Theoretical and Experimental Response Functions," Fourth ICRPG Combustion Conference, Menlo Park, Calif., October 1967.
17. Penner, S. S., Chemistry Problems in Jet Propulsion, New York, Pergamon Press, 1957, pp. 136-156.
18. Mirels, H., "Attenuation in a Shock Tube Due to Unsteady Boundary Layer Action," NACA Report 1333, 1957.
19. Saurer, S. F., Propellant Chemistry, New York, Reinhold Publishing Co., 1966, p. 296.
20. Reed, R., Weber, L., and Gottfried, B., "Differential Thermal Analysis and Reaction Kinetics," Ind. Eng. Chem. Fundamentals 4(1), 38 (February 1965).

21. R. B. Beyer and N. Fishman, "Solid Propellant Ignition Studies with High Flux Radiant Energy as a Thermal Source," Progress in Astronautics and Rocketry, Vol. I, Solid Propellant Rocket Research, New York, Academic Press, 1960, pp. 673-692.
22. N. Fishman, "Solid Propellant Ignition Studies," Stanford Research Institute Final Report, Contract No. AF 04(611)-10534, Report No. AFRPL-TR-65-213, November 5, 1965.
23. Crump, J. E., "Aluminum Combustion in Composite Propellants," CPIA Publication No. 105, Vol. I, Second ICRPG Combustion Conference, May 1966, p. 321.
24. Summerfield, M., Sutherland, G. S., Webb, M. J., Taback, H. J., and Hall, K. P., "Burning Mechanism of Ammonium Perchlorate Propellants," Solid Propellant Rocket Research, Progress in Astronautics and Rocketry, Summerfield, M., ed., Vol. I, New York, Academic Press, 1960, p. 141.
25. Tourin, R. H., Penzias, G. J., and Liang, E. T., "Infrared Radiation and Temperature Measurements in Solid Propellant Flames," Warner-Swasey Co. Report No. TR-800-5, Contract NONR 3657(00), October 1962.
26. Waesche, R.H.W., "Spectrographic Studies of Solid Propellant Flames," Rohm & Haas Co. Report No. S1-11, Contract No. DA-01-021AMC11536(2), (Confidential), October 1966.
27. Povinelli, L. A., "Study of Composite S.P. Flame Structure Using A Spectral Radiation Shadowgraph Technique," NASA Report No. TMX-52071, 1964.
28. Dickinson, L. A., "Command Initiation of Finite Wave Axial Combustion Instability in Solid Propellant Rocket Motors," ARS J. 32, 643(1962).

UNCLASSIFIED

Security Classification

## DOCUMENT CONTROL DATA - R &amp; D

*(Security classification of title, body of abstract and indexing annotation must be entered when the overall report is classified)*

1. ORIGINATING ACTIVITY (Corporate author) Stanford Research Institute Poulter Laboratory for High Pressure Research Menlo Park, California 94025		2a. REPORT SECURITY CLASSIFICATION <b>UNCLASSIFIED</b>	
		2b. GROUP N/A	
3. REPORT TITLE  RESPONSE OF A BURNING PROPELLANT SURFACE TO EROSION TRANSIENTS			
4. DESCRIPTIVE NOTES (Type of report and inclusive dates) Final Report			
5. AUTHOR(S) (First name, middle initial, last name)  G. A. Marxman and C. E. Wooldridge			
6. REPORT DATE April 30, 1968		7a. TOTAL NO. OF PAGES 136	7b. NO. OF REFS 28
8a. CONTRACT OR GRANT NO. AF 49(638)-1665		9a. ORIGINATOR'S REPORT NUMBER(S)  SRI Project PGU-5818	
b. PROJECT NO. 9713-01			
c. 61445014		9b. OTHER REPORT NO(S) (Any other numbers that may be assigned this report) AFOSR No. 68-0771	
d. 681308			
10. DISTRIBUTION STATEMENT  Distribution of this document is unlimited.			
11. SUPPLEMENTARY NOTES  Tech, other		12. SPONSORING MILITARY ACTIVITY AF Office of Scientific Research (SREP) 1400 Wilson Boulevard Arlington, Virginia 22209	
13. ABSTRACT <p>This report describes an investigation of high-amplitude axial-mode solid rocket combustion instability which arises in the form of an oscillating shock wave in the combustion chamber. Experimental studies have provided an evaluation of the influence of compositional factors, oxidizer type, and deflagration characteristics on the incidence of axial instability. The stability characteristics of a wide range of ammonium perchlorate and potassium perchlorate propellants were determined in motors ranging from 15 to 82 in. in length, using an explosive pulse to initiate a traveling shock wave. Differential thermal analysis of these propellants, and experiments incorporating fiber-optic devices with high-speed photography, indicated that surface-coupled heat release is a key factor underlying the different stability behavior observed with various propellants. This concept formed the basis for theoretical studies during the program.</p> <p>A theoretical combustion model was proposed and a mathematical analysis was developed that predicts the response of a burning propellant to the pressure pulse imposed by a traveling shock wave as it passes over the propellant surface. Also considered theoretically was the interaction mechanism through which this burning rate response supports the shock wave. The resulting theory predicts the limits of the stable operating regime for individual propellants in terms of thermochemical parameters and the degree of surface-coupled heat release associated with the propellant type. The theory provides a consistent explanation of all stability characteristics observed experimentally during this program and established guidelines for avoiding axial instability.</p>			

DD FORM 1473 (PAGE 1)

1 NOV 65

S/N 0101-807-6801

UNCLASSIFIED

Security Classification

